SCUOLA DI DOTTORATO
UNIVERSITÀ DEGLI STUDI DI MILANO-BICOCCA

Department of Materials Science

PhD program in Materials Science and Nanotechnology Cycle XXXII

Rare-Earth doped Scintillating Silica Fibers for ionizing radiation detection

Cova Francesca

748598

Tutor: Professor Anna Vedda

Coordinator: Professor Marco Bernasconi

ACADEMIC YEAR 2018 - 2019

Riassunto

I materiali con proprietà di scintillazione trovano ampio impiego in applicazioni che riguardano la rivelazione di radiazioni ionizzanti, quali il monitoraggio e la diagnostica per immagini, la dosimetria in campo medico, la sicurezza nazionale ed industriale, e la fisica delle alte energie. Recentemente, la scoperta di nuovi scintillatori veloci ed efficienti ha rappresentato un campo di ricerca in attivo e continuo sviluppo. Fra i numerosi sistemi indagati, le fibre ottiche scintillanti hanno suscitato grande interesse grazie alla loro estrema versatilità che permette la progettazione di rivelatori con un *design* innovativo.
In questa tesi si propone lo studio di fibre scintillanti di silice che mostrano efficienti proprietà luminescenti quando drogate con ioni di terre rare, come Cerio e Praseodimio.
L'argomento è trattato sia da un punto di vista fondamentale che applicativo, al fine di migliorare ed ottimizzare la resa del materiale perchè possa essere impiegato in rivelatori di nuova generazione.
A questo scopo, si è deciso di studiare gli effetti dell'esposizione ad elevate dosi di radiazioni ionizzanti sulla trasparenza del materiale.
L'ottimizzazione della concentrazione del drogante luminescente nella matrice di silice, nonchè dei processi di sintesi *sol-gel* e di filatura della fibra ha permesso di ottenere un'efficiente propagazione della luce all'interno della fibra stessa. É stata altresì dimostrata la fattibilità di una rivelazione simultanea di luce Cherenkov e di scintillazione, esponendo a fasci di elettroni altamente energetici un piccolo prototipo di calorimetro realizzato con fibre scintillanti drogate con Cerio. Le fibre di silice possono quindi essere considerate promettenti candidate in quell'ambito della calorimetria che prevede l'utilizzo della doppia lettura del segnale Cherenkov e di scintillazione per compensare le fluttuazioni energetiche caratteristiche dell'interazione con adroni pesanti.
Inoltre, una completa conoscenza dei fattori che limitano l'efficienza di scintillazione è di primaria importanza per una futura ingegnerizzazione del materiale: l'esistenza di difetti di punto, che competono con i centri luminescenti nella cattura dei portatori di carica generati a seguito dell'interazione con la radiazione ionizzante, risulta essere la principale causa della presenza di una componente temporale lenta nella cinetica di ricombinazione. É stato quindi condotto uno studio approfondito del ruolo dei difetti nelle fibre di silice, al fine di comprenderne la natura e gli effetti sulle proprietà di scintillazione.
I risultati ottenuti in questa tesi hanno confermato il potenziale di questa tecnologia per applicazioni in rivelatori per fisica delle alte energie e gettato le basi per un ulteriore futuro sviluppo del materiale.

Questo lavoro è stato svolto presso i laboratori del Dipartimento di Scienze dei Materiali dell'Università di Milano-Bicocca, in collaborazione con il Centro Europeo per la Ricerca Nucleare (CERN, Ginevra, Svizzera) e con il *Lawrence Berkeley National Laboratory* (Berkeley, USA). Parte dei dati è stata ottenuta in collaborazione con *Saint Gobain Research* (Aubervilliers, Parigi, Francia) e con l'Istituto di Fisica dell'Accademia delle Scienze della Repubblica Ceca (Praga, Repubblica Ceca).

Abstract

Scintillating materials find a wide variety of applications in ionizing radiation detection systems, monitoring and imaging, real time dosimetry in the medical field, homeland and industrial security, and high energy physics. In the recent years, the development of new, fast, and performing scintillators has been an active field of research. Scintillating fiber technology freshly raised a lot of interest because its extreme flexibility can provide a powerful tool for innovative detector designs.
This thesis focuses on the study of scintillating fibers made of silica glass which show efficient luminescent properties when activated with rare-earth ions, like Cerium and Praseodymium.
Both fundamental and practical aspects are discussed, in view of the improvement and optimization of the material performances for application perspectives in the future generation of high energy physics detectors.
With this objective, the effects of high dose levels of ionizing radiation on the transparency of the material are studied. The fine-tuning of the activator content incorporated in the silica matrix and of the sol-gel synthesis and fiber drawing processes allow to obtain a good light guiding and a well-controlled optical quality. The feasibility of a simultaneous readout of Cherenkov and scintillation light is demonstrated in high energy calorimetry conditions, probing Ce-doped silica fibers embedded in a small detector prototype exposed to beams of electrons. Silica fibers can be considered as promising candidates in the framework of the dual readout calorimetry approach, which aims at compensating the energy fluctuations, inherent to the detection of hadronic particles.
A deep understanding of the factors limiting the scintillation performances is of primary importance for future material engineering: they are found to be mainly related to the presence of point defects, which compete with the luminescent centers in capturing the free carriers created upon irradiation and introduce a delay in the recombination kinetics. A fundamental study of the role of defects in silica fibers, detrimental for the scintillation efficiency, is proposed and discussed.
The potential of silica fibers for applications in high energy physics detectors is outlined and further optimization of the material technology is foreseen.

This work was performed at the Department of Materials Science at the University of Milano - Bicocca, in collaboration with the European Organization for Nuclear Research (CERN, Switzerland) and with the Lawrence Berkeley National Laboratory (US). Some measurements were carried out in collaboration with Saint Gobain Research (France) and the Institute of Physics of the Czech Academy of Sciences (Czech Republic).

Acknowledgements

First and foremost, I would like to express my sincere gratitude and special appreciation to my supervisor, *Professor Anna Vedda*, for her continuous support and inspiring motivation. Her constant guidance allowed me to grow as a scientist and her very kind assistance guided all the time of my research and writing. She helped me with her thoughtful encouragement and careful supervision, throughout every step of the advancement of this work, spending time in proof-reading the various drafts of my thesis and giving me the moral support and the freedom I needed to move on. Her advice have been priceless.
I'm grateful for the exciting opportunities I had the possibility to experience during my PhD, having the chance to work in an international and challenging environment.

I won't forget to express my gratitude to the rest of my research team. Special thanks to *Mauro Fasoli* for his precious and insightful suggestions and comprehensive advice, and for the great job he continuously does for our research group.
I would like to thank *Norberto Chiodini* for having provided the glass samples and fibers I studied during my PhD research, and for the improvements in the sol-gel synthesis technique.
Thanks also to *Roberto Lorenzi* for the help with the Raman and FTIR measurements and results interpretation.
Then special thanks to my co-workers *Irene Villa* and *Roberta Crapanzano* with whom I shared happiness and pain of the routine lab life.

My sincere thanks also goes to *Dr. Etiennette Auffray*, who provided me the opportunity to join her team as an intern and welcomed me in her *Lab27* at CERN: there I had the possibility to experience and work in an exciting atmosphere that challenged me deeply.
Special thanks of course to *Kristof Pauwels* and *Marco Lucchini*, my fellow lab mates at Lab27, for their wonderful collaboration and stimulating discussions, and also for the sleepless nights we were working together to extract as many data as possible during the fibers test beam campaign.
I would like to thank also *Andrea Polesel*, *Rosalinde Pots* and *Nazar Bartosik*, for taking part in this test beam and for all the time they put into it.

Many thanks to *Dr. Edith Bourret*, for having given me the opportunity to spend a two-month period in her group at the *Lawrence Berkeley National Laboratory (USA)*, experiencing a different culture and habits.
Many thanks to *Federico Moretti* for his guidance and help with the measurements during this period, and for his availability to go on collaborating on interesting research topics.

I had like to thank *Dr. Martin Nikl*, *Dr. Jiri Mares*, *Viteslav Jary* and *Romana Kucerkova* of the Institute of Physics of the Czech Academy of Sciences in Prague, for having given me access to their laboratories and research facilities, and for their support with the awkward scintillation measurements.
Also I thank all my Czech friends, especially *Maksym Buryi* and *Robert Kral*, for the beer nights and for having made me feel at home.

Then I would like to thank *Dr. Vladimir Ouspenski* and *Dr. Alessandro Benedetto* from *Saint Gobain Recherche* in Paris, for having welcomed me in their work environment, for their assistance with the nanoindentation measurements, a completely new topic for me, and for having shared their great expertise.
I would also acknowledge *Dr. Veronique Jubera* and *Theo Guerineau* from the University of Bordeaux for the nice collaboration in the framework of the EIT SPARK project.

I would like to thank *Dr. Marco Caresana* and *Gabriele Zorloni* from the *Department of Energy* of *Politecnico di Milano*, and *Jan Hostaša* and *Valentina Biasini* from *CNR Institute of Science and Technology for Ceramics (Italy)* for the new-born and very stimulating collaborations I hope can grow up in the future.

I'll take the chance to thank my office mates at the Department of Materials Science at the University of Milano - Bicocca and all the people and friends in the labs all around the world I was lucky enough to meet. They all really mean a lot to me.
Of course I want to thank all my friends, for their constant presence and for having helped me forget physics besides work (or at least tried).

Many deeply felt thanks to my parents, not only for having listened to my complaints and having shared my moments of happiness, but also for providing me the motivation to always go further in my work and for being my main supporters. Thank you because you have always been and will always be by my side.
It is impossible not to mention my husband *Luca*, for his love and his support during these years, and for having helped me appreciate the littlest moments of relax stolen by the daily routine. You have always been strong for both, being there for me also and especially during the long months abroad: I'm so proud of you. You trusted in me much more than I trusted in myself and I cannot imagine my life without you.

Contents

Introduction **1**

1 Theoretical Background **7**
1.1 Interaction of Ionizing Radiation with matter . . . 7
1.1.1 Photon interaction . . . 7
1.1.2 Electron and positron interaction . . . 9
1.1.3 Heavy particle interaction . . . 12
1.2 The Physical Process of Scintillation . . . 14
1.2.1 Scintillation Mechanism in Inorganic Scintillators . . . 14
1.2.2 General Characteristics of Inorganic Scintillators . . . 18
1.2.3 Signal losses in scintillators . . . 22
1.3 Cherenkov Effect . . . 25

2 Amorphous Silicon Dioxide by Sol-Gel Technique **28**
2.1 Introduction . . . 28
2.2 Sol-Gel Synthesis Technique . . . 30
2.2.1 Rapid Thermal Treatment . . . 32
2.3 Fiber Drawing . . . 33
2.4 Optical Properties and Point Defects in Silica . . . 35
2.4.1 Spectroscopy of rare-earth ions doped silica . . . 37

3 Description of silica samples and influence of the fiber drawing **43**
3.1 Description of the samples . . . 44
3.2 Optical properties . . . 47
3.2.1 Photo-luminescence excitation . . . 47
3.2.2 Raman Spectroscopy . . . 48
3.2.3 Fourier Transform Infrared Spectroscopy . . . 50
3.3 Mechanical properties . . . 51

4 Radiation damage and formation of radiation-induced defects **57**
4.1 Degradation of the optical transmission of Pr-doped silica . . . 58
4.1.1 Decay time of Pr^{3+} luminescence in silica . . . 58
4.1.2 Defect-related induced absorption and radiation damage . . . 59

4.2 Radiation hardness of Ce-doped silica . . . 64
4.2.1 Optical absorption spectroscopy on fibers and bulk silica . . . 64
4.2.2 Attenuation length of light propagation . . . 68
4.3 Conclusions . . . 71

5 Trap distributions and slow scintillation tails in silica fibers 72
5.1 Role of defects in scintillation . . . 73
5.1.1 Thermal detrapping through delocalized bands . . . 74
5.1.2 Temperature independent recombination: athermal tunneling . . . 75
5.1.3 Distribution of trap levels . . . 76
5.2 Radio-luminescence efficiency below and above RT . . . 77
5.2.1 Radio-luminescence sensitization in Ce-doped silica . . . 79
5.3 Scintillation decay as a function of temperature . . . 82
5.4 Phosphorescence . . . 85
5.5 Thermally stimulated luminescence . . . 87
5.6 Conclusions . . . 92

6 Dual Cherenkov and Scintillation Response to high energy electrons 93
6.1 Calorimetry at CERN . . . 94
6.2 Experimental setup . . . 95
6.2.1 Beam line . . . 97
6.2.2 Experimental procedure . . . 97
6.3 Test beam results . . . 99
6.3.1 Pulse-shape analysis . . . 99
6.3.2 Discrimination of Cherenkov and scintillation light . . . 101
6.3.3 Energy reconstruction and linearity . . . 106
6.3.4 Attenuation length . . . 107
6.4 Conclusions . . . 109

Conclusions and Outlook 110

A Scintillation decay as a function of excitation energy 113

B RL sensitization and TSL in Pr-doped silica 115

References 118

Introduction

Scintillators are optical materials able to convert high energy photons or particles into ultraviolet or visible light, thus allowing the detection of ionizing fields by optical systems. Scintillation originates from radiative transitions of intrinsic centers or dopants used as activators, the most common of which are rare-earth (RE) ions [1]. Numerous crystalline and amorphous systems are being investigated whose variety can be significantly increased by composition and geometry engineering strategies recently in advancement.

The development of new scintillating materials has been an important subject of research for years. Almost one century after the birth of the first scintillator in the 40s, the research is still very active as detector technologies are progressing, functionalities and performances of ionizing radiation systems are changing, and material synthesis methods and related knowledge are greatly improving and extending.

Nowadays, scintillating materials are widely used in various fields, such as high energy physics (HEP) calorimetry, radiation monitoring in medicine, homeland security, and industrial controls. Big advances in the scintillation science have recently been reached, for what concerns both a fundamental understanding of the underlying physical mechanisms and technological applications: the materials performance is being brought close to the intrinsic limits, while the requirements are more and more demanding [2]. The evolution of scintillators development and optimization has been tuned by the needs of a specific field of application and then extended to explore new possibilities in material compositions, doping, and shape, and to deepen the fundamental comprehension of the interaction processes occurring between ionizing radiation and matter.

In the past decades, research on scintillating materials was driven by the needs for positron emission tomography (PET) and HEP calorimetry: it played a key role in one of the major discovery of the century, the observation of a Higgs boson which confirmed the predictions of the Standard Model. This new particle was detected at the Large Hadron Collider (LHC) at CERN (Geneva, Switzerland) by the two biggest experiments, CMS (Compact Muon Solenoid) and ATLAS (A Toroidal LHC ApparatuS) on the 4^{th} July, 2012. Such challenging discovery was made possible thanks to a huge collaboration among a wide community of physicists.

HEP experiments are based on accelerating particles that are collided at a very high energy (at the TeV-scale), where each collision creates extreme physical conditions. Designing and operating accelerators that provide the required energy range to various particles is not the only challenge: the careful observation of what happened during the collision is critical. The detectors placed around the location of the collision have to provide the maximum amount of information describing all the sub-products created. High precision of the information supplied by the detectors is necessary for the full reconstruction of the collision details.

Particle energies are measured in detectors called *calorimeters*, where they are stopped, producing a shower of secondary particles. Calorimeters can be classified as electromagnetic or hadronic, according to the type of particles they were designed to study. Electromagnetic calorimeters measure the energy of electromagnetic showers made of electrons, positrons, and photons. On the other hand, hadronic calorimeters do not only focus on hadronic showers, since part of the secondary particles generated by hadrons (mainly pions and nucleons), which interact through a succession of various inelastic interactions, yields electromagnetic cascades. Hadronic calorimeters have therefore to deal with both type of particles and the challenge is to balance the response to these two signals.

Regardless of the type of calorimeter considered, the actions of stopping the particles and measuring their energy can either be performed in separate volumes (sampling calorimeters) or in the same volume (homogeneous calorimeters). In *sampling* calorimeters, the photon energy is partially absorbed in high-density passive absorber plates and only a small fraction of the deposited energy is measured in the sensitive medium interleaved with the absorption medium and transformed into detectable signal. In a *homogeneous* detector, on the other hand, the whole detector volume is active, and the electron or photon showers are fully contained in the sensitive medium. The energy is then revealed by scintillation and Cherenkov light, both collected in highly transparent media or by ionization in conductive liquids [3].

The electromagnetic calorimeter module of CMS was actually made of 75848 lead tungstate ($PbWO_4$) crystals, selected for their high density, good scintillation response, and fast timing performances, of the order of the bunch crossing time (25 ns at LHC): these properties allowed the design of a compact homogeneous calorimeter with fine granularity.

Future HEP calorimeters will be operated under an unprecedented integrated luminosity of 3000 fb^{-1}, which is expected to be provided by the accelerator in 10-12 years. During the High Luminosity LHC (HL-LHC) phase, foreseen to start in 2026, the accelerator will produce between five and ten times more collisions than the LHC, allowing more precise measurements of rare phenomena that are predicted in the Standard Model to be taken, and maybe even detecting new particles that have never been observed before: in these extreme conditions at the frontier of energy, new physics is likely to emerge.
During the HL-LHC phase, collisions rate and radiation levels will increase, becoming much higher than the nominal values for which the CMS detector was designed.
Therefore, new requirements arise for materials employed in the future experiments, especially concerning the challenge of a severe radiation environment: crystals should survive a level of

charged hadron fluence of $6{\cdot}10^{14}$ cm^{-2}, fast neutron fluence of $3{\cdot}10^{15}$ cm^{-2}, and absorbed dose of the order of hundreds of kGy, depending on the region of the detector considered relative to the beam pipe, which will be achieved during the entire HL-LHC operation [4, 5]. To mitigate this challenge, efforts have been made to reduce the light path length in the crystals by new calorimeter designs, and investigations of the radiation hardness of inorganic scintillators to such a dose level have been carried out.
Moreover, in future HEP experiments, the event rate will be pushed to about 10 ns: such a fast rate requires ultrafast scintillators to mitigate the detrimental effect of pileup.

It is worth taking into account that HEP experiments comprising the particle energy measurement require calorimeters having large volumes: therefore, a cost-effective production of large amounts of detector material is a key requirement for the detector specification.

Material shape plays a key role in light collection, which is an important aspect in the detection system.
Several approaches have been proposed to overcome the facing challenges, among which particular attention focused on fiber technology that can provide a powerful tool for innovative calorimeter designs. Fiber geometry is particularly suitable for homogeneous and extremely granular calorimeters: the former being a fundamental requirement for good energy resolution, the latter representing a potential tool to improve particle identification capabilities and pileup mitigation. The extreme flexibility provided by fiber shape allows for multiple implementations of this technology in calorimeter designs as illustrated in Figure 1.

In all the proposed designs, the light signal can be readout by grouping together a bunch of fibers using optical fibers or light guides which collect the photons exiting the fibers and bring them to the photodetector. Such option would allow to reduce the number of channels at the cost of a coarser granularity. Alternatively, each fiber can be readout independently to maximize the spatial granularity and imaging capability of the detector in reconstructing the topology of hadronic showers and jets [8]; this achievement would be made possible by advances in the Silicon Photomultiplier (SiPM) technology.

A new concept of calorimetry was proposed for future collider experiments [6, 9], based on replacing conventional blocks of scintillating material with bunches of scintillating fibers, enabling a higher granularity and more flexibility in the detector design. In addition to the common parameters, like fast decay time, high scintillation yield and good radiation hardness, the fiber shape requires to exhibit a good propagation of the scintillation light; in this frame, much progress has been made in the understanding and optimization of synthesis methods to improve the radial segregation of the dopant, and the attenuation length together with the radiation hardness of crystalline garnet fibers [10, 11].

$Lu_3Al_5O_{12}$ (LuAG) and $Y_3Al_5O_{12}$ (YAG) single crystal fibers grown by the micro-pulling down technique [12] have been intensively studied and showed optimal scintillation properties when doped with RE ions as luminescent activators: moreover, the aliovalent codoping by optically inactive ions, such as Ca and Mg, was found to dramatically increase the light yield and to effectively suppress the slow scintillation decay components, leading to a very fast decay

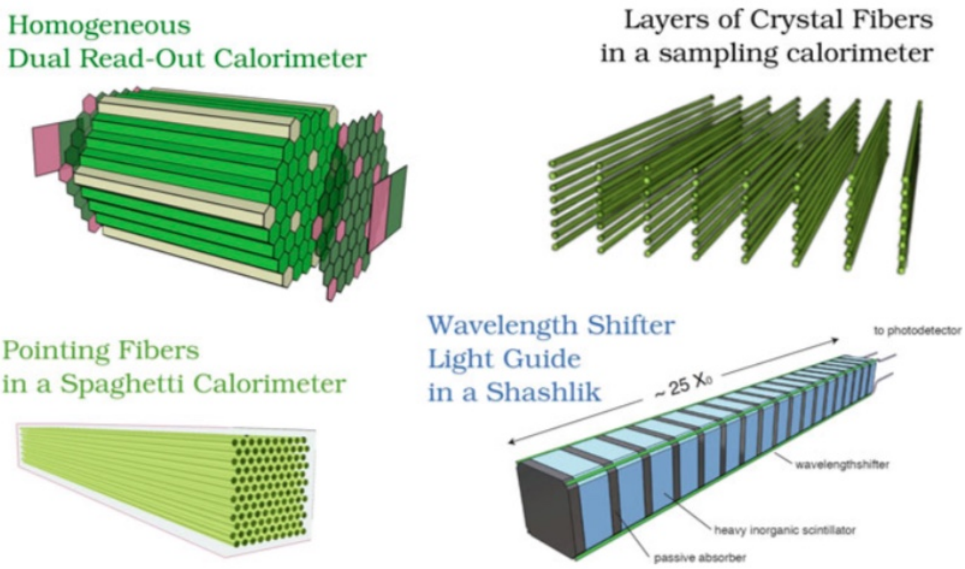

FIGURE 1: Top left: simplified drawing of a homogeneous calorimeter providing a high granularity and dual readout capabilities due to the combination of Cherenkov (white) and scintillating (green) fibers as presented in [6]. **Top right**: schematic view of crystal fibers planes which can be inserted into an absorber structure as the one of current CMS hadronic calorimeter. **Bottom left**: example of a *SpaCal* sampling calorimeter module consisting of a dense absorber filled with crystal fibers with longitudinal axis oriented along the beam direction. **Bottom right**: crystal fibers used as a radiation hard wavelength shifter to readout the light of a *Shashlik* calorimeter [7].

time of the scintillation emission [13]. Crystalline garnet fibers have been characterized under high levels of γ and proton irradiation fields and were demonstrated to have a good radiation hardness [12, 14].

On the other hand, organic scintillating fibers have become widely used in HEP detectors, because of their fast rise and decay time, the latter of the order of few ns, and their high optical transmission. However, radiation hardness remains one of the major issues for plastic scintillators to be operated in high radiation environments: the damage was observed to result in a significant decrease of the light yield of organic fibers [15, 16, 17].

A new approach got a foothold in the recent years, based on the detection of both scintillation and Cherenkov emission, in the so-called *dual readout* method: it consists in recording the two components of the signal separately in order to estimate the fraction of the energy carried by electromagnetic particles. This would substantially improve the energy resolution of hadronic calorimeters by compensating for fluctuations in the electromagnetic fraction of the shower of secondary particles generated upon interactions between the primary particle and the detector medium. Several methods were suggested for the dual readout concept: among them, either the use of two independent active media or the *a posteriori* decomposition of scintillation and Cherenkov components of the light emitted by a single material [9, 18].

This work takes place in the framework of the search for new and fast scintillators satisfying the requirements for future HEP experiments: it proposes RE (Ce, Pr)-doped silica-based

scintillating fibers, produced by sol-gel method, as a potential alternative to single crystalline fibers for dual readout calorimetry.

Silica glass can be drawn in long fibers, either doped or undoped, in a cost-effective way. In the last years, it has been demonstrated that scintillators based on glass matrices are a valid alternative to several crystals, because of their good chemical stability, better mechanical properties, easy preparation, and shaping possibilities. In principle, glass matrices can host luminescent activators in large amounts: the sol-gel technique allows a very good control of the luminescent centers incorporation and dispersion inside the glass matrix and of the purity of the raw material [19]. This latter factor is an essential point in the improvement of the radiation hardness of this class of amorphous materials. Scintillation efficiency, linearity upon dose, and signal reproducibility were optimized in the past decades [20, 21].

Sol-gel silica fibers were at first developed for remote real-time dosimetry in radiology and radiotherapy [22, 23]. Recently they were proposed to be investigated for their interesting scintillation properties, and to be explored as candidates for the active scintillating component in electromagnetic calorimeters.

Scope of this thesis

In this work a complete investigation of scintillating RE-doped sol-gel silica fibers is presented in detail.

A general overview of the basic principles of the scintillation mechanism and all the processes involved, occurring in a material upon interaction with ionizing radiation, is presented in Chapter 1.

A detailed description of the sol-gel synthesis technique and of the properties of pure and doped amorphous silicon dioxide obtained by sol-gel method is given in Chapter 2. The main steps of the fiber drawing procedure and the treatments involved are discussed. An exhaustive review of the most important previous works on the optical properties and point defects of sol-gel silica is also reported, to pave the fundamental starting point from which this work has headed off.

The preparation and morphology of the specific samples, both in bulk and fiber form, measured and investigated in this thesis is discussed in Chapter 3: moreover, the modification of the optical, vibrational, and mechanical properties of sol-gel silica induced by fiber drawing is presented. The process could indeed affect the defectiveness of the glass network, with a change in the local environment surrounding the luminescent centers, due to the high temperatures applied: its role in the response and performances of sol-gel silica is thus disclosed.

The radiation damage effects on the optical absorption and scintillation performances of Pr- and Ce-doped silica fibers are investigated and discussed in Chapter 4, especially concerning the degradation of the attenuation length and the optical transmission upon increasing irradiation dose, to verify the requirements for the possible use in future HEP experiments. The formation of point defects acting as color centers affecting the light propagation is evidenced,

and strategies to improve the radiation resistance are proposed, like the reduction of the dopant concentration and the use of high temperature thermal treatments.

To deeply understand the nature of defects participating in the scintillation process and degrading the application performances, thermally stimulated luminescence (TSL) technique was used to reveal the presence of a broad continuous distribution of defect levels, which was then correlated with the origin of the phosphorescence signal detected as a function of temperature after exposure to X-rays. Localized trap levels, observed by thermo-luminescence analysis, were also found to be responsible for slow tails in the scintillation time decay: moreover, the study of the scintillation decay profiles revealed an interesting dependence of the slow contribution of the decay on the temperature. The results are reported in Chapter 5, together with those related to the dependence of the radio-luminescence (RL) efficiency on the exposure time during irradiation, which give hints on the role of point defects as competitors with luminescent centers in the capture of free carriers created by the interaction with ionizing radiation.

The scintillation properties under high energy electron beams are then measured by embedding Ce-doped silica fibers as the active scintillating component in a small Spaghetti Calorimeter (*SpaCal*) prototype, and addressing the reconstruction of the shower profile and energy.
The feasibility of the dual readout concept is discussed and demonstrated in Chapter 6, and the results of the test beam campaign are presented. The simultaneous detection of both scintillation and Cherenkov components of the emitted light makes silica fibers an interesting candidate for dual readout calorimeters.

The last chapter finally summarizes the results of this thesis and provides an outlook to further activities and research developments.

This work was conducted at the Department of Materials Science at the University of Milano - Bicocca, in collaboration with the EP-CMX-DA group of the European Organization for Nuclear Research (CERN, Switzerland) and with the Lawrence Berkeley National Laboratory (LBNL, US). Some measurements were performed in collaboration with Saint Gobain Research (France) and the Institute of Physics of the Czech Academy of Sciences (Czech Republic).
It was carried out in the frame of the Crystal Clear collaboration and was supported by the Horizon 2020 RISE Intelum project (Grant No. 644260), the Horizon 2020 Research Infrastructures (AIDA-2020) (Grant No. 654168), the ASCIMAT project (Grant No. 690599), and the EIT SPARK project (Grant No. 16290).

Chapter 1

Theoretical Background

In this chapter, a brief review of the main theoretical aspects required for the understanding of this thesis will be provided. The basic concepts of the physics of ionizing radiation interaction with matter will be addressed, the process of generation of scintillation light, and the Cherenkov effect will be introduced.

1.1 Interaction of Ionizing Radiation with matter

When interacting with a material, an incident particle deposits its energy by various mechanisms, depending mainly on the kind of particle. A scintillator can convert this energy into low energy photons which can then be detected. Before describing the scintillation process in inorganic scintillating materials, the different types of interactions involved are briefly reviewed.

1.1.1 Photon interaction

High energy photons interact mainly with the electrons of a material, losing their energy by the three fundamental mechanisms of electromagnetic interactions: photoelectric effect, Compton scattering and pair production. The interaction cross-section (σ) through each of these processes is energy dependent.

In the *photoelectric effect*, the energy of the incoming photon is completely absorbed by an atom and subsequently an electron (called *photoelectron*), usually in one of the inner shells, is ejected: the atom is therefore left with an ionized inner shell ($atom^+$).

$$\gamma + atom \rightarrow e^- + atom^+ \tag{1.1}$$

The probability for this process to occur increases with the atomic number Z and decreases with the photon energy E_γ. The cross-section for the photoelectric effect can be estimated for

photons of energy much higher than the binding energy as

$$\sigma_{ph} \propto \frac{Z^5}{E_\gamma^{7/2}} \tag{1.2}$$

This effect is thus dominant at low energies ($E \lesssim 100$ keV), where the total absorption of the photon is favored, and in dense materials.

In the *Compton scattering*, the incoming photon is inelastically scattered on an electron of the detector atoms and only part of its energy is transferred; although, it is enough to free the electron from its shell. After the interaction, the photon has a different angle and a lowered energy, so that further interactions of this photon with the medium are possible.

$$\gamma + atom \rightarrow \gamma^{'} + e^{-} + atom^{*} \tag{1.3}$$

The cross-section of this process increases with the atomic number Z and decreases with the energy E_γ, in a way that it is prevalent at medium energies:

$$\sigma_{cpt} \propto Z \, \frac{\ln(E_\gamma)}{E_\gamma} \tag{1.4}$$

It is noteworthy that both types of excitation leave holes in the core shells of the atoms (Eqs. 1.1, 1.3): the consequent de-excitation of these atoms leads to the generation of additional soft photons/electrons, through X-ray fluorescence and Auger effect, when electrons from the other shells are filling these gaps.

The *production of an electron-positron pair* becomes possible if the energy of the incident photon exceeds 1.022 MeV, the mass-energy of an electron-positron pair at rest. The cross-section of this process in the nuclear field increases with the nuclear charge and the photon energy, so that it is predominant at high energies ($E \gtrsim 1$ GeV):

$$\sigma_{pp} \propto Z^2 \ln(2E_\gamma) \tag{1.5}$$

The detailed behavior of the three types of interactions as a function of the photon energy is displayed for silicon dioxide (SiO_2) as an example in Figure 1.1. The mass attenuation coefficient is reported instead of the respective cross-sections and is defined as

$$\frac{\mu}{\rho} \propto \frac{\sigma_{tot}}{A} \cong \frac{(\sigma_{ph} + \sigma_{cpt} + \sigma_{pp})}{A} \tag{1.6}$$

where A is the mass number.

It can be noticed that the maximal penetration is reached around 10 MeV: at lower energy, the photons only penetrate a few micrometers of matter before being absorbed and converted into photoelectrons. In the GeV energy region, the attenuation coefficient tends to a constant value.

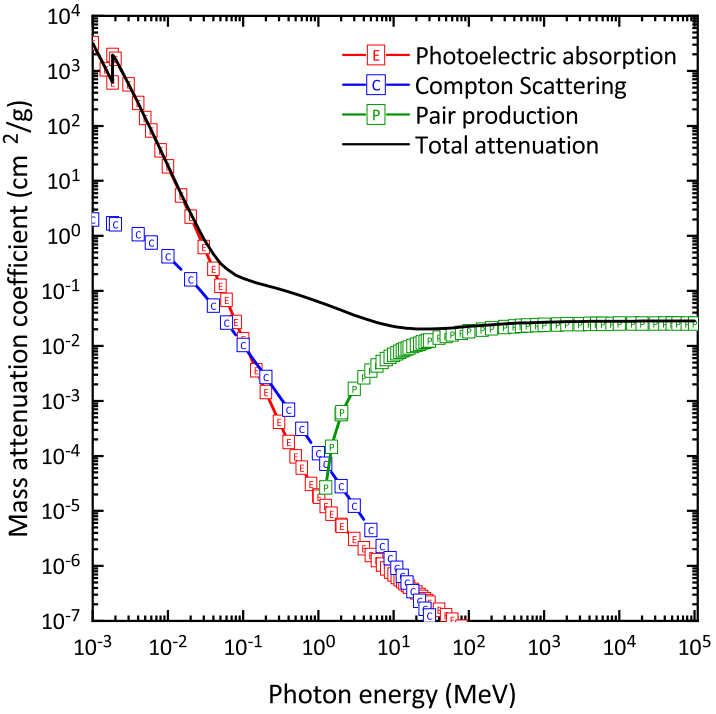

Figure 1.1: Mass attenuation coefficient in SiO_2 as a function of photon energy, as computed from [24].

1.1.2 Electron and positron interaction

Light charged particles, like electrons and positrons, can be deflected from their trajectory by the electric field of the atoms of the medium. This deceleration of the charged particle in the Coulomb field of the nucleus results in the emission of electromagnetic radiation.
This effect is called *bremsstrahlung*, and the related radiation losses can be expressed as [25]:

$$-\left(\frac{dE}{dx}\right)_{brems} = \frac{N_A E Z(Z+1)e^4}{137 m_0^2 c^4}\left(2\ln\frac{2E}{m_0c^2} - \frac{4}{3}\right) \tag{1.7}$$

where Z is the atomic number of the medium and N_A the Avogadro constant. The radiation losses increase linearly with the particle energy and the energy deposition follows an exponential law: therefore, only fast electrons ($E \geq 1$ MeV) can have a significant yield of *bremsstrahlung*, and radiative losses are most important for absorber materials with large atomic number.

A charged particle passing through matter dissipates its kinetic energy also by excitation and ionization of the atoms, allowing a tracking of the particle itself. In the second process, the incident particles transfer enough energy to the atomic electrons to free them from the atom: the less energetic electrons and photons produced are used in detectors for signal generation. The mean ionization and excitation loss is given by the Bethe-Block formula, which can be written for electrons as [25]:

$$-\left(\frac{dE}{dx}\right)_{ion} = \frac{2\pi e^4 N_A Z}{m_0 \nu^2}\left(\ln\frac{m_0\nu^2 E}{2I^2\gamma} - \ln 2\,(2\sqrt{\gamma}-\gamma) + \gamma + \frac{1}{8}(1-\sqrt{\gamma})^2\right) \tag{1.8}$$

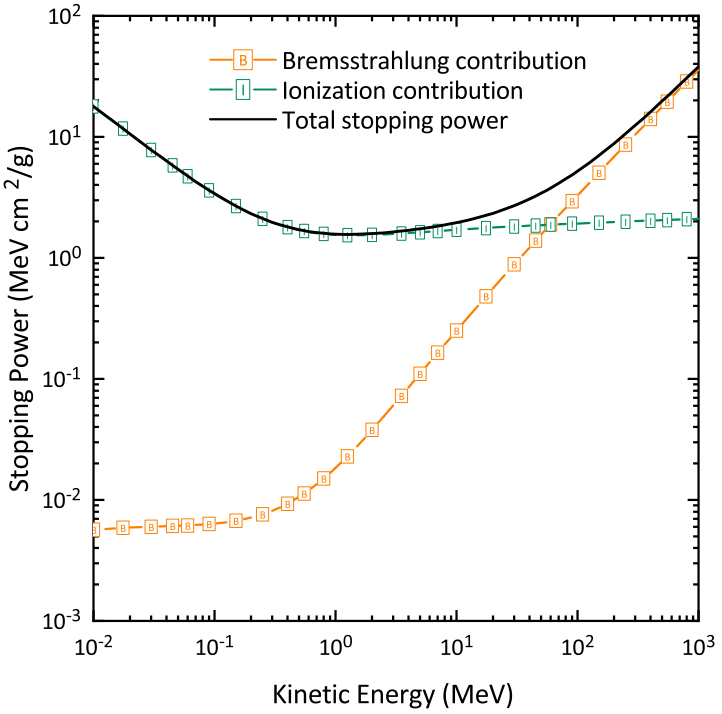

Figure 1.2: Linear stopping power of SiO_2 as a function of kinetic energy of incoming electrons, as computed from [26].

where $\gamma = 1 - v/c^2$, m_0 the electron mass, and I the mean excitation energy. Non-relativistic particles stay longer in the neighborhood of the atomic electrons and therefore transfer more energy to them. Increasing the electron energy reduces this energy transfer until a *plateau* is reached: in this region the losses become constant, regardless of the particle type.
At high energies, the expansion of the electric field yields to a slow rise of the ionization losses, called *relativistic rise*.

The relative weight of the *bremsstrahlung* and ionization contributions depends on the particle energy. The sum of ionization and radiative losses gives the total linear stopping power, defined as:

$$\frac{dE}{dx} = \left(\frac{dE}{dx}\right)_{brems} + \left(\frac{dE}{dx}\right)_{ion} \tag{1.9}$$

In Figure 1.2 the two contributions are reported for SiO_2: it can be observed that the ionization process is predominant at low energies ($E \lesssim 10$ MeV), whereas losses through *bremsstrahlung* are more important at high energies.

Electromagnetic showers

An *electromagnetic shower* is the process through which energetic ($\gtrsim$ GeV) electromagnetic particles interacting with matter generate a large production of secondary particles (photons, electrons and positrons), often referred to as *multiplicative shower* or *cascade shower*.
The secondary particles, produced by the primary energetic one, interact through the same processes, leading to the production of a particle cascade inside the material.

The shower development stops when secondary particles are slowed down to energies at which energy losses from ionization processes are higher than from *bremsstrahlung*. To describe the behavior of an electromagnetic shower, it is useful to define the *critical energy* E_c, as the energy at which the loss rates from ionization and from *bremsstrahlung* become equal: it is a crucial parameter to characterize a material. A reasonable parameterization of E_c for liquids and solids, obtained from experimental results [27], is given by

$$E_c = \frac{610}{Z + 1.24} MeV \tag{1.10}$$

The parameters used to define the longitudinal and transversal size of a shower are respectively the *radiation length* and the *Molière radius*. The radiation length X_0 is defined as the mean distance that an electron travels to lose $(1 - 1/e)$ of its energy by *bremsstrahlung*, and can be parameterized as

$$X_0 = \frac{716.4\ A}{Z(z+1)\ \ln(287/\sqrt{Z})}\ g/cm^2 \tag{1.11}$$

This formula can be approximated to $X_0 = 180\ A/Z^2\ g/cm$. The mean distance covered by a photon before converting to an electron-positron pair with probability $(1-1/e)$ is equal to $\frac{9}{7}X_0$: this means that if the incident primary particle is a photon, the shower will start to develop slightly later with respect to electrons. However, in both cases, the mean longitudinal profile of the energy deposited by an electromagnetic shower can be described by a Γ-distribution function [27, 28] according to

$$\frac{dE}{dt} = Eb\ \frac{(bt)^{\alpha-1}\ e^{-bt}}{\Gamma(\alpha)} \tag{1.12}$$

where $t = x/X_0$, $b \approx 0.5$, $\alpha = bt_{max} + 1$ and t_{max} is the point where the distribution has its maximum, corresponding to the position where the number of secondaries starts to decrease. The depth of the shower maximum moves logarithmically with the incident particle energy, according to

$$t_{max} \propto \ln\left(\frac{E}{E_c}\right) \tag{1.13}$$

Due to the multiple scattering of the electrons by the electric field of the nuclei, the shower develops also in the transverse direction: in general, the 90 % of an electromagnetic shower energy is contained within the Molière radius, defined as

$$R_M \propto E_s\ \frac{X_0}{E_c} \tag{1.14}$$

where $E_s = \sqrt{4\pi/\alpha}\ m_e c^2 = 21.2$ MeV.

The shower development is a pure statistical process that can only be efficiently modeled with Monte-Carlo simulations, and it is sketched in Figure 1.3: here a simplified model to describe the average behavior of the shower has been considered.

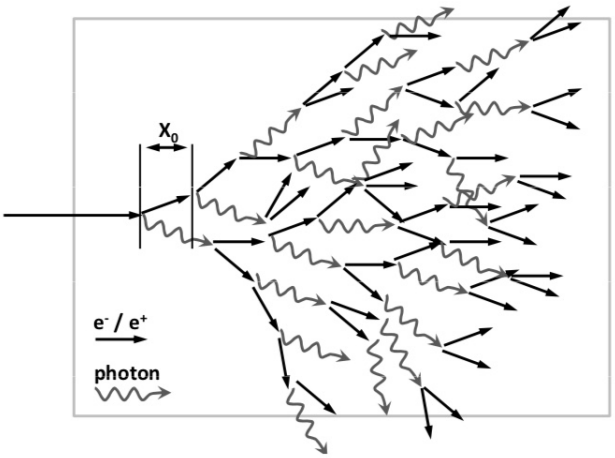

Figure 1.3: Sketch of the development of an electromagnetic shower.

1.1.3 Heavy particle interaction

Heavy charged particles, like protons and α particles, lose their energy by ionizing and exciting the atoms of the medium: however, the ionization losses depend slightly on the property of the medium, because of the weak penetration of these particles.

Neutrons interact with matter mainly through a strong interplay with the nuclei, by scattering and absorption processes resulting in photons and charged particles production, which can be detected due to their electromagnetic interactions with the medium. At first, neutrons slow down via elastic scattering and once thermalized are subjected to neutron capture by the nuclei: de-excitation of the nuclei via emission of photons can yield to a delayed detectable signal. This cascade of secondary photons and electrons subsequently gives rise to scintillation signal.

Hadronic showers

Due to its different nature, hadrons interaction with matter presents a significantly different behavior with respect to electrons and photons interaction: an incident high energy hadron interacts with the nucleons of the nuclei of the absorber through inelastic collisions [29]. This results in the production of a wide range of secondary particles, that in turn undergo a variety of interactions: the most abundant are the lightest particles, $\pi^{\pm}$ and π^0. The last type of pions, which account for about 30 % of the secondaries, decay into photons and create electromagnetic showers. Therefore, part of the hadronic shower detection is based on the same mechanisms described in the previous section. Charged hadrons (p, $\pi^{\pm}$, μ) also dissipate energy via elastic scattering and ionization.

The secondary particles that do not interact electromagnetically undergo strong interactions that involve, among others, nucleus excitation, nuclear fission and production of hadrons: these processes do not all yield detectable signals. A large fraction (around 30 %) of the hadron energy does not dissipate in particle production but is lost in the binding energy of the nuclear

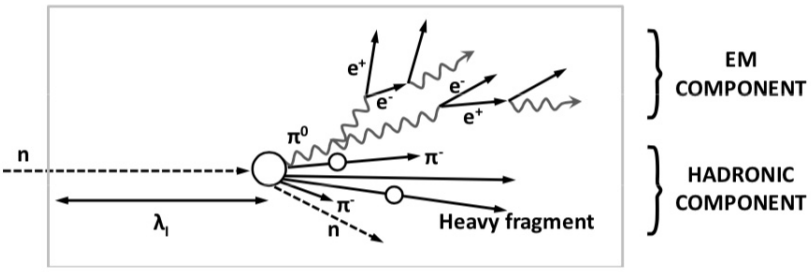

Figure 1.4: Schematic model of the hadronic shower development produced by a high energetic neutron.

break-up and recoil fragments. Ionizing particles (40-60 % of the shower), such as spallation protons, α particles and nucler fragments, yield ionization tracks in the detector.

Hadronic showers are characterized by a particle multiplicity that rises logarithmically with the incident particle energy: the various possible mechanisms of interaction, represented in the sketch of Figure 1.4, do not generate the same signal in the detector and therefore give origin to large fluctuations in the hadronic response. Indeed, for each incident hadron, the shower development can differ significantly, due to the large fluctuations on the (small) number of π^0 produced and on their position along the shower profile. This consequently leads to large fluctuations in the energy deposition.

Similarly to electromagnetic showers, a quantity describing the average longitudinal development of the hadronic shower can be introduced: it is called *interaction length* λ_I and is defined as the mean distance that a hadron covers to lose $(1 - 1/e)$ of its energy in inelastic collisions, related to the mean distance that separates two consecutive nuclear interactions. It can be expressed as

$$\lambda_I = \frac{A}{N_A \rho \ \sigma_{inel}} \ cm \approx 35 \ A^{1/3} \ g/cm^2 \tag{1.15}$$

where ρ is the density of the material and σ_{inel} is the cross-section of a proton inelastic interaction, which scales as $\propto A^{2/3}$. The longitudinal profile of the energy deposition of a hadronic shower can be parameterized by a sum of Γ-functions convoluted with a descending exponential, representing the purely electromagnetic and the purely hadronic component of the shower, respectively.

An important parameter to describe a hadronic shower is the average fraction f_{em} of energy contributing to the electromagnetic component, mainly through π^0 and η^0 production. Its energy dependence can be approximated by the expression [30, 31]:

$$f_{em}(E) = 1 - \left(\frac{E}{E_0}\right)^{m-1} \tag{1.16}$$

in which E_0 is in the range 0.7 - 1.0 GeV and m can vary between 0.8 and 0.9 depending on the material properties.

1.2 The Physical Process of Scintillation

The scintillation mechanism is usually referred to as a general process converting the energy deposited by ionizing radiation into a light signal (great number of low energy photons) [1, 32]. This can occur in different ways depending on the particular nature of the material involved. A wide variety of scintillators are currently used for various applications. Scintillators can be in solid, liquid or gaseous physical state and are commonly divided into two main categories based on their composition: organic and inorganic scintillators.

The organic scintillators are made of aromatic hydrocarbon compounds which contain benzene ring structures bounded in various manners (anthracene, stilbene, naphthalene). In these materials, light is emitted as a consequence of transitions made by the free valence electrons of the molecules which occupy the molecular orbitals. This process, being very fast, leads to a luminescence which tipically decays within few nanoseconds. For this reason, they are mostly used for applications which require a fast response, such as time of flight measurements. Organic plastic scintillators, in which the primary fluorescent emitter is suspended in a solid polymer matrix, are largely used also because of their ability to be easily shaped and their relatively low cost.

Inorganic scintillators are usually crystals grown in high temperature furnaces, or silica-based materials, often with a small amount of activator impurity. In this case, the scintillation process is due to the electronic band structure that characterizes crystals, and is not molecular in nature, as in the case of organic scintillators. A particular advantage of this type of materials is their high density, which provides a good stopping power for incident radiation: this allows to contain and convert the whole particle energy into light signal.

1.2.1 Scintillation Mechanism in Inorganic Scintillators

The physical mechanism of scintillation is characterized by a complex sequence of phenomena: the main steps of the process, each characterized by different time constants, can be outlined as follows.

1. *Absorption of ionizing radiation*, such as X-rays of γ quanta of intermediate energy, leaves the scintillator in a non-equilibrium state: the energy of the incident radiation is completely absorbed by the solid, if the photoelectric effect is predominant. This initial energy release in the medium occurs in a time range limited by the transit time of the particle or γ quantum in the scintillator.
   The outcome of this first process is the creation of primary free electrons and inner shell holes, resulting from the scintillator relaxation toward a new equilibrium state ($A + h\nu \rightarrow A^+ + e$, where A is an atom of the scintillating material).

2. Relaxation occurs in an avalanche of secondary excitations, such as secondary electrons, holes, photons and plasmons. Fast electrons lose their energy mainly through inelastic scattering on electrons of the materials. This mechanism generates additional electron-hole pairs and is called *multiplication*. For low energy electrons, only electron-phonon

inelastic scattering occurs. This process is called *thermalization* and further described at item 3. An atom with an ionized inner shell (A^+) can relax either radiatively, by emitting a photon (typically X-rays), or non-radiatively, by generating a secondary electron (Auger effect): the probability of non-radiative decay is usually much greater than that of radiative decay. A fast electron can interact also with phonons, through scattering processes, or with valence electrons, producing collective oscillations of the electron continuum, known as plasmons.
The cascade ionization process continues until the resulting electrons and photons are no longer able to cause further ionization, because their energy falls below the *ionization threshold* (two times the energy gap E_g). The duration of the process is estimated to be $10^{-15} - 10^{-13}$ s, depending on the initial electron energy. At this point, all electrons in the conduction band have an energy smaller than $2E_g$ and all holes occupy the valence band if there is no core band lying above the Auger process threshold.

3. All the ionization processes finally create electron-hole (e-h) pairs and their resultant number N_{eh} is proportional to the energy E_γ of the incident radiation absorbed by matter:
$$N_{eh} = \frac{E_\gamma}{\xi_{eh}} \tag{1.17}$$
where ξ_{eh} is the average energy required to create a single thermalized e-h pair. ξ_{eh} approximates (1.5 - 2.0) E_g for ionic crystals and (3.0 - 4.0) E_g for the materials with a predominant covalent type of bonding.
Thermalization of the low energy secondary products, or *electron-phonon relaxation*, starts as soon as the electron energy falls below the ionization threshold and the electrons begin to interact with the environmental vibrations. This process results in low energy excitons and e-h pairs, whose number remains constant and whose energy is roughly equal to the band gap. The energy dissipated non-radiatively and converted into phonons during this process is lost since it cannot contribute to the scintillation signal. The thermalization losses represent the main part of the full energy losses in inorganic scintillators.
The carrier thermalization time in inorganic crystals is rather fast ($10^{-11} - 10^{-12}$ s), due to the high density of electron states, but it is longer than the duration of electron-electron relaxation. Therefore the two processes can be considered as events following each other. At the end of this stage, the electrons reach the bottom of the conduction band and holes reach the top of the valence band.

4. The *carrier migration* process is a transport stage ending in the excitation of the luminescent centers, which takes place through energy transfer from the migrating electronic excitations to the luminescent centers themselves, with characteristic time constants in the *ps* time range.
The energy losses during this stage depend essentially on the spatial distribution of electrons and holes relative to luminescent centers: if both partners, created in the track, are found adjacent to a luminescent center, the recombination process will be effective,

otherwise the carriers can be captured by traps. Deep traps remove electrons and holes from the process leading to the emission of scintillation signal, whereas carriers captured by shallow traps can be thermally released and then take part in the recombination. Therefore, this process involves a delay in the scintillation emission.
Various impurities and lattice defects can play a role in the electron and hole trapping, for example leading to the formation of F centers, which are stable electronic defects of an anion vacancy capturing an electron, or of V_k centers, resulting from the sharing of a hole between two neighboring anions (also called self-trapped hole STH). It can then occur that self-trapped excitons (STEs) are formed through the capture of free electrons by V_k centers and subsequently decay emitting a photon.

5. The last step of the scintillation process is the *recombination* of *e-h* pairs and the consequent emission of photons, in the case of radiative recombination, or phonons, if the recombination is non-radiative. The simplest emission process is the result of a direct recombination of free thermalized electrons in the conduction band with holes in the valence band or in deeper electronic shells ($e + h \rightarrow h\nu$): it occurs in direct band gap semiconductors. Usually, the recombination takes place when the energy of the electron and the hole has sufficiently decreased so that they can bind to each other creating an exciton with energy slightly lower than the band gap, which recombines emitting a photon.
Most scintillators are so called extrinsic since their matrix does not have sufficient scintillating properties, and a dopant element acting as a luminescent center is incorporated into the matrix, to enhance the probability of radiative recombination. These activators are usually rare-earth ions, like Ce^{3+}, because of its parity and spin-allowed transition $4f^{n-1}5d \rightarrow 4f^n$. Since, for most of the host matrices, the ground state ($4f$) and the lowest excited level ($5d$) lie in the band gap, the radiative recombination is more probable due to the smaller energy gap. Recombination through doping centers is therefore favored from the energetic point of view: moreover, in the presence of activating species A, the exciton luminescence is efficiently quenched, causing thus a sensitization of the activating ions luminescence. In this case, the excitation of radiative centers is the result of the energy transfer from excited matrix states ($e + h + A \rightarrow ex + A \rightarrow A^* \rightarrow A + h\nu$).
The direct excitation of activating centers by ionizing radiation ($A \rightarrow A^* \rightarrow A + h\nu$) provides an important contribution to scintillation in the case of heavily-doped or self-activated scintillators.
Electrons and holes can also recombine non-radiatively by interacting with the crystal lattice and emitting phonons. In this case the energy is dissipated thermally and does not contribute to the optical signal: the probability of non-radiative recombination increases with temperature due to the larger vibrations of the lattice.

The kinetics of scintillation is defined as the variation in time of the scintillation light intensity, related to the population of the luminescent centers excited states. Its magnitude is proportional to the light yield, defined as the amount of light emitted by a scintillator per unit energy deposited in the medium by ionizing radiation in a limited time range (usually $\sim 1\ \mu s$).

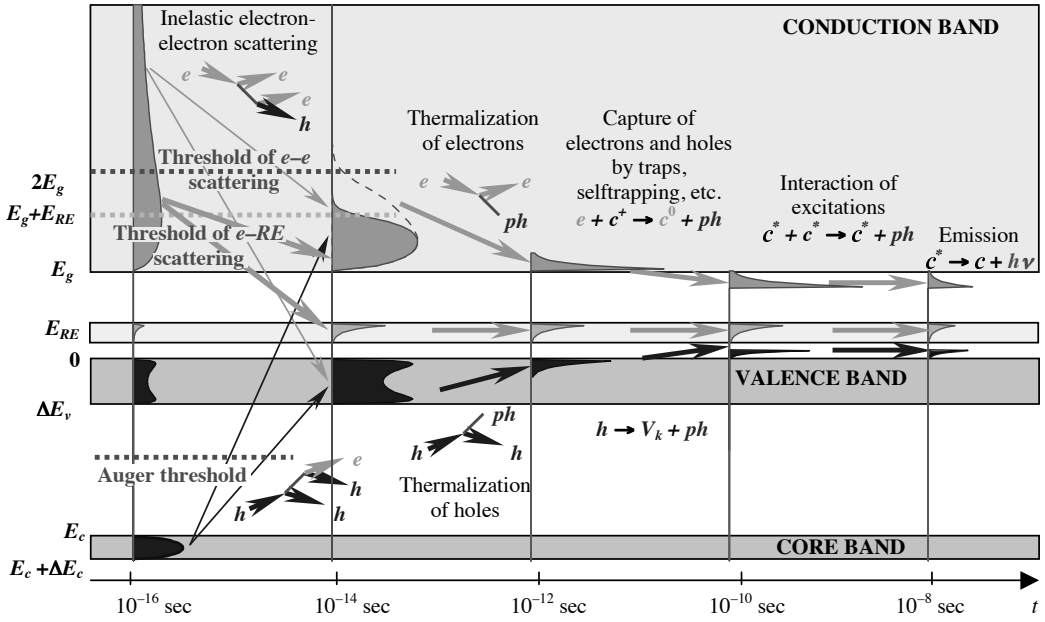

Figure 1.5: Schematic representation of the scintillation mechanism in an inorganic scintillator. The process is shown as a function of time and represents the evolution of particle energy during the several processes involved in the scintillation emission. The picture is taken from [33].

For a given material, a plurality of luminescent centers, whose radiative levels are localized in the forbidden zone, can coexist and interfere with each other: some of them are cations or anionic complexes of the lattice or dopant ions specifically introduced at the crystal growth, some others are generated by the interaction of the ionizing radiation with the medium. Such induced centers play an important role in the scintillation process, as they can sensitize or quench the luminescence or act as electron or hole donors for existing radiative centers via secondary excitation processes. This secondary excitation is generated not only by direct Coulomb interaction, but also by thermo-activation or electron tunneling from matrix host defects, which trap electrical carriers produced by the incident radiation.

The kinetics of primary and secondary excitation processes is different: defining ω_{int} as the frequency of interaction between primary and secondary luminescent centers, it is possible to distinguish two different cases, depending on how the mean time betweeen interactions compares with the time of formation τ_f of primary excited luminescent centers and with their radiative decay time τ_r.

If $1/\omega_{int} \sim \tau_f \ll \tau_r$, the kinetics of direct scintillation will dominate, characterized by a very fast rise time followed by a single exponential decay, whose time constant does not exceed a few nanoseconds, if the final state involves a core atomic band.

If, on the other hand, $1/\omega_{int} \gg \tau_r$ and $1/\omega_{int} \gg \tau_f$, direct recombination may be accompanied by a phosphorescence, which results from the delayed decay (with characteristic time constants in the μs - ms range) of the secondary luminescent centers.

In real cases the situation is often very complex, involving energy transfer between centers and temperature-quenching phenomena, and the resulting light emission kinetics is strongly non-exponential.

The general scheme of Figure 1.5 illustrates the scintillation mechanism, described in this section, in the case of crystals containing RE ions as luminescent activators: they can be regarded as one of the most important group of scintillators exhibiting a complex band structure. RE ions can indeed be directly excited through impact excitation, provided that their concentration is high enough: however, this excitation is efficiently produced only by electrons with kinetic energy above the electron-RE scattering threshold and below the electron-electron scattering threshold. These electrons cannot produce more electronic excitation and therefore it would be expected a high light yield for RE-doped crystalline scintillators.

1.2.2 General Characteristics of Inorganic Scintillators

From the scintillation process described above, it is clear that each material will have a different behavior depending on its physical properties, like band structure and defects concentration. There is a considerable interest in finding inorganic materials with optimal scintillation properties: the essential feature required for any scintillator is to be an effective converter of ionizing radiation into detectable light. Among the desirable characteristics of a good scintillator, high efficiency, fast scintillation and good energy resolution are the most important.

Light Yield Of crucial importance is the capability of a scintillator to convert the energy deposited by ionizing radiation into optical signal. It is therefore fundamental that the amount of light generated is as large as possible in order to be efficiently detected and converted into an electrical signal, usually by means of a photodetector. This property, called *light yield*, is defined as the number of photons produced per MeV of deposited energy E_{dep}

$$LY = \frac{n_{photons}}{E_{dep}} = \frac{E_{dep}\ \eta}{\langle h\nu \rangle\ E_{dep}} = \frac{\eta}{\langle h\nu \rangle} \tag{1.18}$$

where $\langle h\nu \rangle$ is the average energy of emitted optical photons and η the overall conversion efficiency. This number depends on the efficiency of energy conversion during the various processes of scintillation, from pair production to light emission. The number of electron-hole pairs generated depends on the energy ξ_{eh} required to create them via the relation

$$N_{eh} = E_{dep}/\xi_{eh} \tag{1.19}$$

where ξ_{eh} is related to the band gap E_g of the scintillator through

$$\xi_{eh} = \beta E_g \tag{1.20}$$

and the numerical coefficient β is around 1.5 - 2.0 for ionic crystals. Considering inefficiencies in the process of charge carrier migration to the luminescence centers and the quantum efficiency of photon emission, an additional factor α will contribute to the total efficiency.

Thus the overall conversion efficiency from energy to light can be written as

$$\eta = \frac{\alpha}{\beta}\frac{\langle h\nu \rangle}{E_g} \tag{1.21}$$

From Eq. 1.21 it can be observed that crystals with larger $\langle h\nu \rangle / E_g$ ratio can have in principle a higher scintillation efficiency.
In the following, the material parameters mandatory to achieve a good light yield are discussed.

Efficiency The efficiency of activated scintillators is strongly dependent on the ratio of the host band gap to the energy of the activator radiative state, as well as on the relative position of its ground and excited states to the top of the valence band and to the bottom of the conduction band, respectively.
The first requirement for an activator with an excited state energy E_r to be efficient in a host with a band gap E_g is

$$E_g \geq E_r \tag{1.22}$$

This condition prevents the self-absorption of the luminescence in the medium.
Another condition to avoid the delocalization of electrons from the activator excited state is related to the energy distance ΔE between the radiative level of the dopant ion and the bottom of the conduction band: therefore, if $\Delta E > 0$, the scintillation yield is $Y \geq 0$, otherwise $Y = 0$. Moreover, if $\Delta E \gg k_b T$ (where k_b is the Boltzmann constant and T the temperature), the scintillation yield is only weakly dependent on the temperature.

Time Response The time distribution of emitted photons is also relevant for most applications. It is usually important to have a fast signal, in order to allow operation at high rates without being affected by signal pileup effects. The intensity of emission $I(t)$ rises exponentially with a rise time constant which is very fast ($\approx 10^{-11}$ s) due to the short duration of the first steps of the scintillation process (e-h pairs creation and migration to the luminescent centers). Once all the luminescence centers are filled, the emission is close to its maximum and starts to decrease with an exponential behavior which depends on the number of luminescence centers N, their relative intensity P_i, and their decay $\tau_{d,i}$ and rise $\tau_{r,i}$ time constants. The general formula [34] describing the probability density function of scintillation photons to be emitted at a time t after the beginning of the scintillation process at time θ is

$$P(t|\theta) = \sum_i^N P_i \frac{1}{\tau_{d,i} - \tau_{r,i}} \left[e^{-\frac{t-\theta}{\tau_{d,i}}} - e^{-\frac{t-\theta}{\tau_{r,i}}} \right] \tag{1.23}$$

where, for most crystals, $\tau_{r,i} \ll \tau_{d,i}$ and the maximum of the emission occurs at $t \approx \theta$. In case several luminescent centers (> 3) with similar $\tau_{d,i}$ are involved, the time distribution loses its exponential behavior and the estimation of the different components becomes crucial. A more practical quantity τ_{eff} can be defined as the time interval containing a fraction $(1 - 1/e)$ of the scintillation light

$$\frac{\int_0^{\tau_{eff}} I(t)dt}{\int_0^{\infty} I(t)dt} = \left(1 - \frac{1}{e}\right) \approx 63\% \tag{1.24}$$

Such quantity, regardless of the specific kinetic of the color centers, gives an indication of the time evolution and allows to compare the time response of different scintillators.

Optical Properties In order to be detected, the light emitted has to reach the photodetector and to produce an electrical signal. For this reason it is very important to understand the processes occurring from the point of the emission of a photon to its detection. These processes are mainly absorption, Fresnel reflections and Rayleigh scattering. Their relative probability depends on the band gap width, the refractive index n of the material, and the amount of impurities in the lattice, which can result in the creation of absorption and scattering centers. A way to quantify these effects is to measure the transmission of a material, that is defined as the fraction of direct light transmitted through its thickness. Since absorption and scattering phenomena show a dependence on the wavelength λ, the transmission is usually measured by means of spectrophotometers, which can spread the light beam into its components. By comparing the intensity of the light before and after it traversed a certain thickness inside a material, it is possible to estimate the fraction of photons absorbed or diffused. Transmission measured using spectrophotometers has to account for Fresnel reflections which set an upper limit to the maximum amount of light transmitted, given by

$$T_{th}(\lambda) = \frac{(1-r)^2}{1-r^2} \tag{1.25}$$

where r is the reflection coefficient related to the refractive index $n(\lambda)$ according to

$$r(\lambda) = \left|\frac{n(\lambda)-1}{n(\lambda)+1}\right|^2 \tag{1.26}$$

By comparing the measured transmission T_{meas} with Eq. 1.25, the intrinsic absorption coefficient of a material can be defined as

$$\mu_0(\lambda) = \frac{1}{L}\ln\left(\frac{T_{th}}{T_{meas}}\right) \tag{1.27}$$

where L is the length of the material which the light beam passes through.

Emission Spectrum The band gap of the host matrix, as well as the band structure of activators in extrinsic scintillators, defines the wavelength distribution of emitted photons. Inorganic scintillators usually display wide luminescence bands, because the photon assisted transitions are broadened due to the strong interactions of carriers with phonons of the lattice. This property of scintillators has to be taken into account when the signal has to be detected by means of photosensors whose efficiency of converting light into electrical signal is λ-dependent. In particular, to optimize the detection of photons, it is important that the quantum efficiency of the photodetector is sufficiently high in the spectral region close to the maximum of the emission.

Phosphorescence A feature which characterizes some scintillators is a long-time luminescence with decay constants of several microseconds and more, which is usually called *phosphorescence* or *afterglow*. This effect is due to the thermal release of electrons and holes from traps, such as defects and impurities of the crystal lattice as well as defects induced by irradiation. The intensity of phosphorescence $J(t)$ usually decreases exponentially with a time constant τ_s, which is related to the probability for a charge carrier to be released. Considering a charge carrier trapped in a potential well of energy E, the probability to escape from the well at a temperature T is proportional to e^{-E/k_bT}, where k_b is the Boltzmann constant equal to $8.617 \cdot 10^{-5}$ eV K^{-1} [1]. The intensity of the afterglow (valid for $\tau_s \gg \tau_{d,i}$) can be described by the equation

$$J(t) = \frac{k_b N}{\tau_s} e^{-\frac{t}{\tau_s}} \tag{1.28}$$

where k_bN is the number of photons emitted by the luminescent centers excited by the electrons released from traps.
Depending on the particular band structure and on the relative position of traps and color centers energetic levels, trapped carriers can also migrate to neighboring luminescent centers due to tunneling effect. The tunneling effect has a temperature-independent probability to occur, which is proportional to t^{-1}, according to [35]

$$I(t) = -n_0 \phi e^{-Kt/t} \tag{1.29}$$

where $K = \nu e^{-\phi r}$ is the tunneling rate, with ν the frequency factor, r the electron-hole center separation and $\phi = 2(2mE)^{0.5}/\hbar$. Tunneling through a potential barrier would provide the electron with another means by which recombination with the positive charge could occur, with the resulting emission of a luminescence photon.

Radiation Hardness Even if scintillators are designed to measure ionizing radiation, radiation damage can occur upon exposure to high levels of ionizing radiation, and consists in the degradation of light production and collection efficiencies with accumulation of radiation dose. The interaction of ionizing radiation with the material invariably creates new traps and defects. Defects can be of different nature, as shown in Figure 1.6: Schottky defects are formed when oppositely charged ions leave their lattice site creating vacancies, Frenkel defects occur when an atom or cation leaves its place in the lattice creating a vacancy and becomes an interstitial by lodging in a nearby which is not usually occupied by an atom. Interaction of energetic hadrons with the crystalline structure can also create clusters of defects and a consequent distortion of the lattice which, in addition to absorption centers, introduces scattering centers diffusing light through Rayleigh scattering [36].
The properties of the scintillator under exposure to ionizing radiation can degrade in the following way:

1. An increase in the number of shallow traps enhances the phosphorescence.

2. The formation of new traps acting as color centers can result in new absorption features which absorb the photon emitted by the scintillation process on its path to the photodetector, lowering the detectable light.

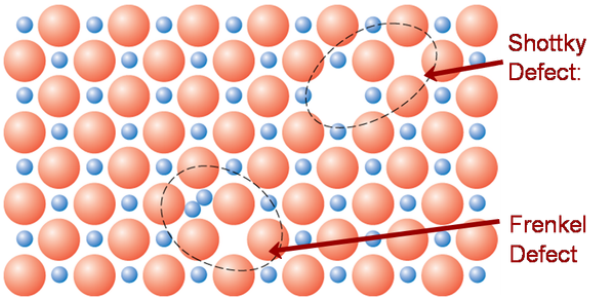

Figure 1.6: Schematic representation of the most common lattice defects.

3. New defects in the crystal structure can decrease the mobility of charge carriers and the efficiency of *e*-*h* pairs to recombine at luminescent centers, reducing the light yield.

4. Direct interaction of radiation with luminescent centers can modify the characteristics of the emitted light, such as emission spectrum and decay time.

5. High energy hadrons can activate the scintillator material leading to induced radioactivity which results in additional background phosphorescence.

Radiation hardness is not a well-defined quantity, but it is often used as a way to measure the maximum dose tolerated in actual detectors, which relates to the capability of a material to maintain its scintillating properties unchanged after irradiation. It has been suggested [37] to define the radiation hardness as a dose which should significantly reduce the transmittance at the emission peak wavelength (by 20 % to 40 %). Investigations on the radiation hardness of a material play a large role in the course of searching for new scintillating materials to be used in high energy physics detectors.

1.2.3 Signal losses in scintillators

The primary source of signal loss in scintillator-based detectors is non-radiative recombination: it always competes with the scintillation process, and although the choice of the synthesis technique and the band gap engineering can make non-radiative recombination less probable, it cannot in general be completely excluded. Other ways of energy loss occur upon thermalization of the charge carriers. In the following, the main sources of signal losses are described: thermal and concentration quenching are related to the presence of the activator, whereas carrier trapping and clustering of excitation densities affect the charge carrier transfer stage of the scintillation process.

Non-radiative recombination Various processes accounting for non-radiative recombination are reported in Figure 1.7. A *thermal quenching* of the luminescence occurs when the excitation energy is completely given up as heat to the lattice: the two parabolas of Figure 1.7a have a large offset, which leads to the presence of a crossing point. If the temperature is high enough, the electron in the relaxed-excited state may reach the crossing and a return to the ground state in a non-radiative manner is then possible: the larger the offset, the easier the transition occurs.

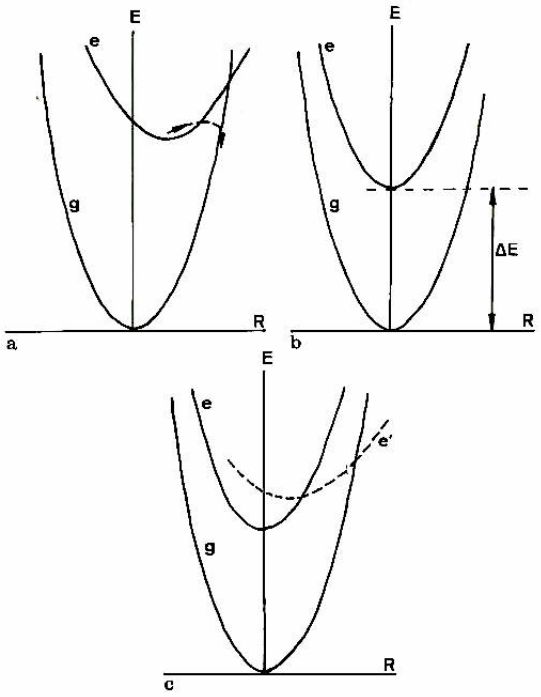

Figure 1.7: Configurational coordinate diagrams illustrating various non-radiative processes: they show the potential energy curves of the luminescent center as a function of the configurational coordinate, which is usually related to one of the vibrational modes of the center involved and to the mean inter-atomic distance R [38].

The *multi-phonon emission* is a process in which a few high energy vibrations are simultaneously excited. This occurs when the energy difference ΔE between the two parabolas is equal to or less then 4 - 5 times the higher vibrational frequency of the surroundings, as explained in Figure 1.7b, even if the parabolas are parallel and would never cross.
Figure 1.7c shows a situation where the level e' feeds the emitting level e in a three-parabolas diagram: the parallel parabolas belong to the same configuration, so that they are connected only by forbidden optical transition. The third one originates from a different configuration ad its connection with the ground state is probably allowed. The non-radiative transition between the two upper parabolas is easy and then emission occurs from the lowest one.

Concentration quenching When the concentration of activators is increased in the host matrix, more and more interactions between these luminescent centers become possible: the excitation energy can thus travel over a long distance in the solid. Increasing this distance results in a high probability for the charge carriers to meet a quenching site where the energy is lost non-radiatively. This phenomenon is called concentration quenching and, for most scintillators, it becomes effective at concentrations of few atomic percent. The emitted scintillation is usually faster but less intense.

Charge carrier trapping Luminescent centers like Ce^{3+} are efficient traps, but since the recombination occurs through these centers, the trapping actually favors the recombination process. However, structural defects in the host matrix are other sources of electron or hole trapping. In SiO_2 for example, the paramagnetic defect due to oxygen surplus not linking two

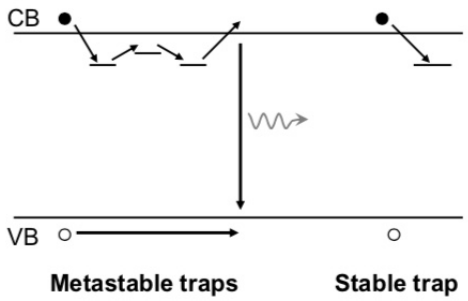

Figure 1.8: Metastable and stable electron traps.

silicon atoms (non-bridging oxygen [39]) leads to the formation of an empty hole trap next to the top of the valence band. This kind of trapping competes with luminescent centers and their respective concentration in the host matrix determines which effect is dominant.
In general, two types of traps can be distinguished: metastable and stable traps, represented in Figure 1.8. The stable ones trap the charge carriers for a long period, and once they are filled after irradiation, no longer play any role in competing with recombination on luminescent centers. On the other hand, metastable traps delay the light emission, significantly altering the signal collection: if the life time of the trap is slightly longer than the acquisition time, the trap emptying might indeed contribute to a misleading signal emission.
The charge carrier escape from traps is temperature dependent: thermal energy allows the carriers to reach again the conduction band, being released from the trap, and to subsequently recombine radiatively.
Thermally stimulated luminescence is a very efficient investigation tool for the study of trap distribution in a material: the technique and some applications are described in Chapter 5.

Electronic excitation clustering In general, the non-uniform distribution of electronic excitations can be related to a strong dependence of the electron mean free path on the energy; during thermalization, the energy is in fact deposited as separated small excitation clusters. In particular, one of the main mechanism of creation of clusters of electronic excitations is connected with Auger processes from core holes. Fast ionizing particles lose energy in scattering events producing each time a cluster of excitations in the material: in the high-energy part of the track, these clusters are not overlapped, but in the low-energy region of the track, overlapping plays a significant role. At the initial stage of relaxation of such clusters, the interaction of the nearest electron with the positive cluster core is much higher than in the individual electron-hole pair, and therefore the recombination probability at least for the inner electrons increases. The clustering phenomenon explains the difference in the excitation distribution when the excitation energy decreases at the low energy range.
Clustering can thus lead to quenching effects and to modification of the energy transfer process toward the activator centers: this results into a decrease of the yield and changes in the decay kinetic.

1.3 Cherenkov Effect

A technique used to produce an optical signal proportional to the particle energy is based on the *Cherenkov effect*. This phenomenon was detected for the first time in 1934 by the scientist Pavel Alekseyevich Cherenkov, who formulated a first explanation of it.
Detectors based on scintillation light are sensitive both to hadrons and electromagnetic particles: for some applications, such as particle identification, it is highly useful to measure only one of them. Detectors based on the Cherenkov effect are receiving a lot of interest as detectors dedicated to the detection of electromagnetic particles.

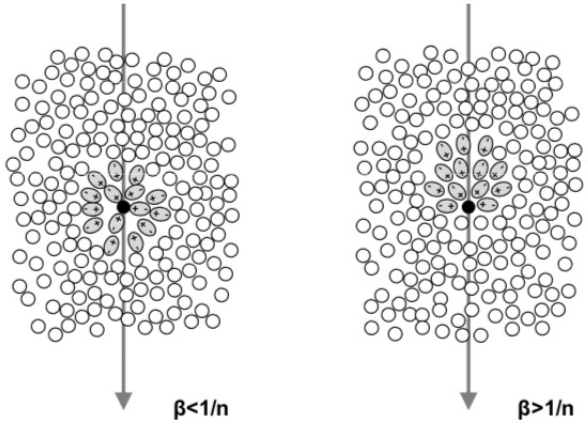

Figure 1.9: Polarization of the atoms of the medium leading to Cherenkov effect [40].

The Cherenkov radiation is generated when a charged particle travels in a medium, with refractive index n, with a velocity higher than the phase speed of light in that medium, given by $(v_\phi)_{light} = c/n$. It occurs when

$$\beta = \frac{v}{c} > \frac{1}{n} = \beta_{threshold} \tag{1.30}$$

For a particle with a given mass, it is possible to express this threshold in terms of energy, since the velocity of a particle and its energy are linked through the relativistic equation

$$E = mc^2 = \frac{m_0 c^2}{\sqrt{1 - \frac{v^2}{c^2}}} = \frac{E_{rest}}{\sqrt{1 - \beta^2}} \tag{1.31}$$

where m_0 and E_{rest} are respectively the mass and the energy of the particle at rest.
The kinetic energy corresponding to the Cherenkov threshold $(KE)_{ch}$ can thus be expressed as

$$(KE)_{ch} = (E - E_{rest})_{ch} = E_{rest} \left[\frac{1}{\sqrt{1 - \beta_{ch}^2}} - 1 \right] \tag{1.32}$$

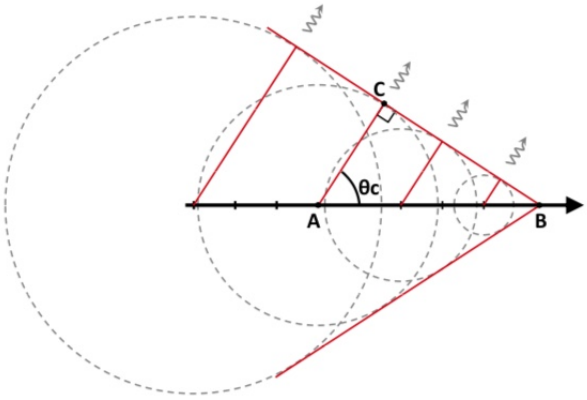

Figure 1.10: Schematic representation of Cherenkov light production for a charged particle with velocity v moving in a medium having refractive index n. Light is emitted at an angle θ_{ch} according to Eq. 1.33.

The fact that particles can travel faster than the speed of light becomes of high interest for charged particles. They can polarize the atoms in the neighborhood of their tracks when passing through matter. In most of the cases, this polarization is arranged symmetrically around the particle path and therefore, although each individual atom behaves as an electric dipole, no large scale dipole field is observed [40]. However, at high velocities, namely above the Cherenkov threshold, the particle in motion travels faster the the speed at which it interacts with its environment: the symmetry in the atoms polarization is then broken, as explained in Figure 1.9. The integrated dipole field is no more vanishing and the dipole moment leads to the formation of a wave front, represented in Figure 1.10. This results in the emission of the characteristic electromagnetic radiation, called Cherenkov radiation.

Cherenkov light is emitted in the forward direction at a characteristic angle θ_{ch} with respect to the track of the charged particle. It can be computed as follows: during Δt, the particle travels a distance $\Delta t\ \beta c$ whereas the photon moves by $\Delta t\ c/n$ (distances AB and AC respectively in Figure 1.10).
The Cherenkov angle is thus obtained by

$$\cos(\theta_{ch}) = \frac{AC}{AB} = \frac{\Delta t\ c/n}{\Delta t\ \beta c} = \frac{1}{n\beta} \tag{1.33}$$

As an example, for SiO_2 having refractive index $n = 1.47$, neglecting its wavelength dependence, the threshold velocity is $\beta_{threshold} = 0.68$ and the angle for Cherenkov emission is $\theta_{ch} \sim 47°$. It can be observed that the Cherenkov angle increases with the particles velocity and is maximum for relativistic particles ($\beta = 1$).

The number of Cherenkov photons emitted per unit wavelength and per unit path length in the medium is given by

$$\frac{d^2N_{ph}}{dL\ d\lambda} = 2\pi\alpha z^2 \frac{\sin^2\theta_{ch}}{\lambda^2} = 2\pi\alpha z^2 \frac{1}{\lambda^2}\left(1 - \frac{1}{n^2\beta^2}\right) \tag{1.34}$$

where $\alpha = 1/137$ is the fine-structure constant, z is the charge of the particle in units of e, λ the wavelength of the photon and dL the path length in the medium.
The spectrum of emitted Cherenkov photons thus exhibits a $1/\lambda^2$ dependence: as a consequence, most of the Cherenkov photons are emitted in the UV range. Cherenkov photons are not emitted in the X-ray range because in this region the index of refraction is $n = 1$, and the conditions for Cherenkov emission cannot be fulfilled.
It is worth noting that the number of the emitted Cherenkov photons is much lower with respect to the number of photons produced in a typical scintillation process for the same amount of deposited energy. Another important feature of the Cherenkov light is the non-isotropic nature of the process: the emitted photons are produced along a cone with opening angle θ_{ch} with respect to the particle trajectory. This represents an important difference with respect to scintillation light and has consequences on the choice of the geometry of Cherenkov-based detectors [41]. One of the advantages of Cherenkov light, which makes it of particular interest for applications at high rates, is its prompt emission: the Cherenkov effect occurs simultaneously with the passage of particles and the width of the produced signal is much shorter than the time constants involved in most of the scintillation processes [31, 42].

Chapter 2

Amorphous Silicon Dioxide by Sol-Gel Technique

An overview of the most important and specific features of amorphous silica, widely studied in the past twenty years, is illustrated in this chapter. The main stages of its synthesis by using the sol-gel method are introduced, and a description of the treatments silica undergoes to transform the material from a bulk form to a fiber shape is also given. Finally, a summary of the most relevant results previously obtained in the literature, concerning the properties of undoped silica and the effects of RE doping, is reported.

2.1 Introduction

Usually employed silica for both production of common glasses and technological applications (such as optical fibers, microelectronic components and scintillating glasses) derives from melting processes of SiO_2-based materials, like powder melting, thermal growth, chemical vapor deposition, etc.
Silica appears to be a promising host matrix for several reasons, such as its high band gap providing a high optical transparency and its easy integration with the optical fiber technology. Recently, one among several synthesis techniques has been considerably developed: the sol-gel method has been improved in order to produce silica via chemical means. The first observations leading to the development of this method date back to the beginning of the 20^{th} century, but only several years later the sol-gel method started to raise interest because of its possible technological applications. Nowadays, the sol-gel technique is employed to fabricate glassy and ceramic materials with unique structural and morphological properties.

Concerning the scintillators field of production, the sol-gel technique represents a promising way, because it was proven to allow a very good control of the purity of the starting raw materials and of the luminescent centers incorporation and dispersion inside the glass matrix.

In general, scintillators based on glass matrices are attractive systems: they have good mechanical properties, good chemical stability, they are not hygroscopic (hygroscopicity is a serious drawback of several common used scintillators) and glass matrices can host luminescent activators (as RE ions) in large amounts. However, at concentration above 1 mol.%, the formation of RE-rich clusters was detected: this phenomenon was found to affect the scintillation efficiency as well as the glass homogeneity [19, 43, 44]. Moreover, the amorphous isotropic structure of glass, leading to the isotropy of the thermal expansion coefficient, favors the coupling with other materials in detector systems, and provides easy shaping into the desired form. Another relevant point is that the technology of glass preparation should imply moderate costs of production.

Scintillating glasses are thus suitable materials for the development of optical fibers, which is extremely important for the image reconstruction in several modern radiation detectors, where remote sensing and position-sensitive detection are crucial aspects, for example in the manufacturing of two-dimensional sensors. Among the several requirements of scintillating optical fibers, fast luminescence response, good luminosity and radiation hardness need careful optimization [45]. Among the application perspectives of fiber sensors, real time dosimetry in medical devices [22] and high energy physics experiments raised a lot of interest in the last years; in HEP detectors fibers can be applied either as active scintillating materials or as wavelength shifters for the collection and transport of light [46].

Specific care has to be taken in the preparation technology to the very high purity of the starting materials, in order to limit the concentration of both impurity-related and intrinsic defects in the final glasses. Actually, these might give rise to non-radiative recombination channels, as well as act as precursors of radiation-induced defects, which may affect the radiation hardness especially in severe radiation environments, like those experienced by high energy physics detectors.
Since the concentration of defects depends on the amount of uncontrolled impurities, the radiation hardness of the undoped material should be the highest; the impurity level depends both on the purity of the raw material and on the growth conditions. Sol-gel glass synthesis can be performed by using high purity precursors, thus reducing the level of unwanted impurities [19].

The unique structures, microstructures and compositions that can be achieved by the sol-gel method open therefore many possibilities for practical applications.

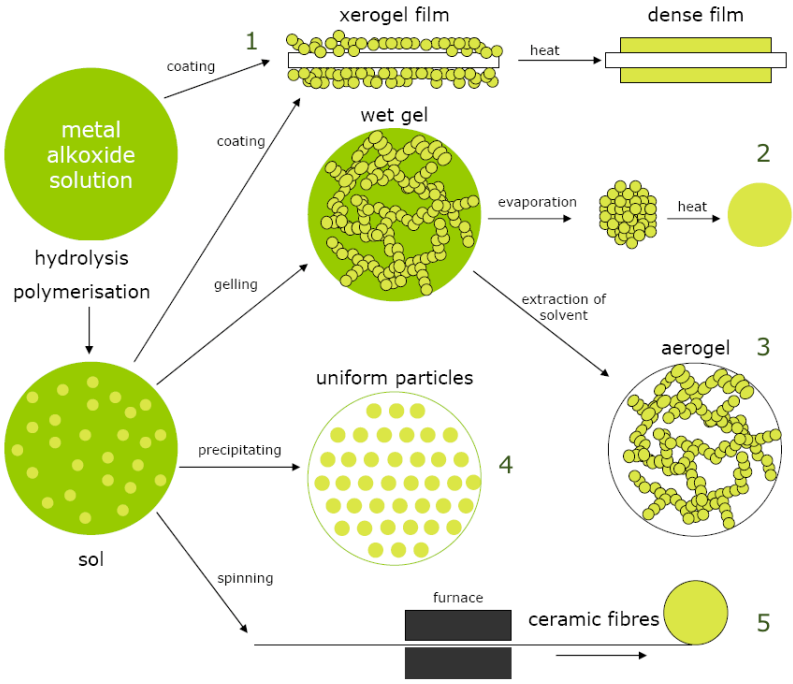

Figure 2.1: Schematic representation of the different stages and routes of the sol-gel processing.

2.2 Sol-Gel Synthesis Technique

The various stages and routes of the sol-gel technology are summarized in Figure 2.1: hydrolysis, condensation, drying and sintering can be pointed out as the four main steps of this process, described in detail in this section [47].

Hydrolysis and Condensation A *sol* is defined as a colloidal suspension of solid particles in a liquid: a *colloid* is in fact a suspension in which the dispersed phase is so small ($\sim 1 - 1000$ nm) that the gravitational forces are negligible and interactions are dominated by short-range forces, such as Van der Waals attraction and surface changes.
The precursors for the preparation of a colloid consist of a metal or metalloid element surrounded by various ligands: common precursors are inorganic salts or organic compounds. In sol-gel research, the most widely used class of precursors are metal alkoxides, which have an organic ligand attached to a metal atom; the most thoroughly studied example is tetraethyl ortosilicate (TEOS), $Si(OC_2H_5)_4$. Metal alkoxides react readily with water and this reaction is called *hydrolysis*, because a hydroxhyl ion (OH^-) belonging to the water molecule becomes attached to the metal atom.
Depending on the amount of water and catalyst, hydrolysis can go to completion, so that all the alcoholic groups are replaced by OH groups, or stop while the metal is only partially hydrolyzed. Two partially hydrolyzed molecules can link together in a *condensation* reaction, which liberates a small molecule such as water or alcohol.

Sol-Gel Transition The sequence of hydrolysis and condensation reactions can continue to build larger and larger silicon-containing molecules, in which Si atoms are linked by oxygen bridges, through the *polymerization* process. If a molecule reaches macroscopic dimensions, creating a three-dimensional lattice extended throughout the solution, the substance is said to be a *gel*. The *gel point* or *sol-gel transition* is the time (or degree of reaction) at which the last bond is formed, completing the macromolecule.
The sol-gel transition can be considered a proper phase transition. In the sol phase, only molecules on an atomic scale are present and the material has the properties of a liquid, whose viscosity gradually increases as the transition point approaches. Close to the transition point, a sudden viscosity increase occurs and bonds form at random between nearly stationary clusters (polymers or aggregates of particles), linking them together in a network. Once the transition has taken place, the resulting system is not comparable to a liquid anymore: it now can hold out against shear stress and elastically warp like an isotropic solid.
At this point, neither a conventional liquid nor a conventional solid exists anymore: the substance is now a gel that contains a continuous solid skeleton enclosing a continuous liquid phase of colloidal dimensions.
Gelation can occur after a sol is cast into a mold, in which case it is possible to make objects of the desired shape. Alternatively, gelation can be produced by rapid evaporation of the solvent.

Drying and Sintering Bond formation does not stop at the gel point: in first place, segments of the gel network can still move close enough together to allow further condensation. Moreover, there is still a sol within the gel network, and those smaller polymers or particles continue to attach themselves to the network.
The structure and properties change after gelation is called *aging* process and may involve further condensation, dissolution and reprecipitation of monomers, or phase transformations. Shrinkage of the gel, due to the capillary pressure rising when liquid evaporates during *drying*, involves deformation of the network and transport of liquid through the pores. The resulting dried gel, called *xerogel*, is often reduced in volume by a factor 5 to 10 compared to the original wet gel. On the other hand, if the wet gel is dried under supercritical conditions, there is no interface between liquid and vapor, so there is no capillary pressure and a relatively little shrinkage: the product is an *aerogel* which may be mostly air, having volume fractions of solid as low as ~ 1 %. Xerogels and aerogels are useful in the preparation of dense ceramics, but are also interesting in themselves because of their high porosity and surface area. The thermal treatment leading to the xerogel formation induces the solvent evaporation and the condensation reaction completion, with the creation of oxygen bridges.

Most gels are amorphous even after drying, but many crystallize when heated. If the aim of the process is to produce a pore-free material, it is necessary to heat the gel to a temperature high enough to cause the collapse of the pores driven by the surface energy, in a process called *sintering*: the maximum temperature reached during this process is called *densification temperature*. It is important to understand the relative weights of sintering and crystallization, because densification is easiest if sintering can be completed before crystals appear.

During the sintering process, some parameters such as temperature ramps or atmosphere composition can be varied to obtain materials with specific properties: for example, the average pore size can be controlled, the formation of crystalline phases can be observed as well as changes in the valence state of dopant ions.

2.2.1 Rapid Thermal Treatment

Once the sintering stage is concluded, an additional treatment at very high temperature, called *rapid thermal treatment* (RTT), can be performed on silica glasses. During this process, the glass is heated up quickly (in about 5-7 s) to a temperature usually in the 1500 °C - 1700 °C range, by means of an oxygen-hydrogen flame; it is kept at this elevated temperature for about 10 s and then rapidly cooled down in air.

Previous works spent much effort in the study of the effect of RTT on the optical emission and absorption properties of silica glass doped with RE ions.

Measurements of Ce-doped silica before and after RTT demonstrated that the RTT process causes a particularly strong increase in the Ce^{3+} RT RL intensity (of about a factor 6), without significant spectral shape modifications [48]. On the other hand, the RTT treatment neither affects the temperature dependence of the RL emission, nor the fast components of the decay curve. The enhancement of the emission intensity as a consequence of RTT might be ascribed to several factors:

1. a further decrease of the OH content in the glass, that can be monitored by infrared spectroscopy as demonstrated in Section 3.2.3;

2. a conversion of Ce^{4+} ions into Ce^{3+} luminescent ions, observed by optical absorption spectroscopy as reported in Figure 2.7;

3. a dissolution of Ce-based aggregates, leading to a better dispersion of the Ce ions, both in the 4+ and in the 3+ valence states;

4. a quenching of the defect-related non-radiative recombination channels, which can be investigated by thermally stimulated luminescence, as discussed in Section 5.5.

The dissolution of Ce^{3+}-Ce^{4+} dimers with the disappearance of the related absorption band and the improved efficiency of carrier transfer to Ce^{3+} ions were demonstrated to be the main cause of the RL efficiency increase after RTT [19]. The intensity of the charge transfer band of Ce^{4+} is also slightly enhanced ($\sim$ 20 %) by RTT, indicating that this treatment leads to a small increase of the number of Ce^{4+} ions in the glass.

The TSL intensity was observed to be strongly increased by the RTT process, although the distribution of the glow peaks was not significantly altered [49]. The TSL increase is mostly due to an improved efficiency of the free carrier transfer to the RE luminescent centers and not to an increased concentration of traps. It was suggested that also the observed enhanced stability of the RL signal under prolonged irradiation after RTT could be ascribed to the improved efficiency of the free carrier transfer towards the recombination centers during

irradiation. Such effect is possibly due to the removal of non-radiative recombination paths in the proximity of the luminescent center.

Recently, it was pointed out that the heating process required for the fiber drawing, better described in the next section, influences the trap distribution in a way qualitatively similar to the effects of RTT on bulk glass [50]. Moreover, it was recognized that RTT strongly influences the concentration and physical dimensions of RE aggregates in highly doped silica, giving rise to a significant improvement in the material transparency and scintillation efficiency.

These results further corroborate the hypothesis that RTT and fiber drawing modify the network surrounding RE ions and change the spatial distribution of intrinsic defects.
The demonstrated positive influence of RTT on the scintillation properties of sol-gel silica suggests that this kind of treatment should be considered an essential step in the glass preparation technology in order to improve the optical performances.

2.3 Fiber Drawing

The typical stages of the manufacture of optical fibers consist in the preform fabrication, fiber drawing, cooling and coating, as illustrated in Figure 2.2. The silica glass preform is drawn to the desired fiber diameter by radiation heating to above its melting temperature under an applied axial tension, leading to a drastic change in preform diameter and temperature. Upon exiting the furnace, the temperature of the drawn fiber is lowered down from around its melting point of approximately 1900 K to below 500 K through convective and radiative cooling. The neck-down from the preform dimension to the final fiber diameter is therefore critical, since it governs the geometry in the furnace and in turn the final fiber quality.
Molten glass can be drawn directly from the furnace to make tubing, sheets, fibers and rods with an uniform cross-section: therefore, temperature and drawing speed and rate must be precisely controlled to obtain accurate final size.
As external capillary coating, many types of materials can be employed: they are applied either during the drawing operation or at a later time: the addition of specific agents to the coating material can bring unique functionality to the resulting capillary.
The fiber drawing process was demonstrated to maintain the amorphous character of the silica network and a good RE dispersion [23]: the structural and optical properties of active fibers are further investigated in this work and compared to those of the parent bulk glass, aiming at understanding the influence of the drawing process on the scintillation performances of the material.

The principle of light guiding inside an optical fiber takes advantage of the total internal reflection phenomenon, occurring only if certain conditions are fulfilled.
When a ray of light, incident upon the interface between two transparent optical media of different refractive index, is incident from the direction of the more dense material and when the angle made by the ray and the normal to the interface is greater than the critical angle, the light will be reflected, and not refracted. The critical angle θ_c is dependent only on the indexes of refraction of the two media, n_1 and n_2:

$$\theta_c = \arcsin\left(\frac{n_2}{n_1}\right) \tag{2.1}$$

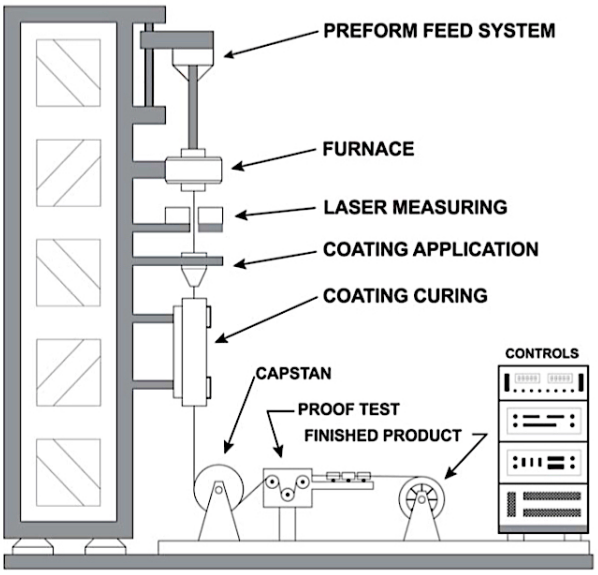

(A) Modern drawing tower [51].

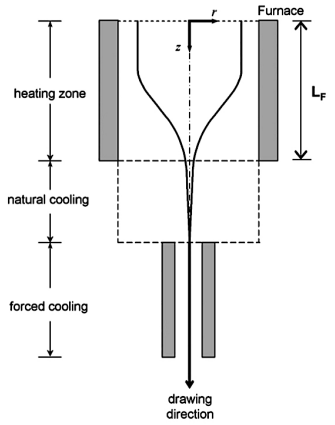

(B) Enlargment of the preform feed system and of the first part of the drawing neck [52].

Figure 2.2: Schematic representation of the fiber drawing process, showing on the right an enlargement of the neck-down region in the furnace.

This principle applies both at the fiber - air interface and at the fiber core - fiber cladding interface, if a coating is present: to obtain an efficient total internal reflection, the difference between the refractive index of the fiber cladding and the refractive index of the core should be the highest. For this reason commercially available fluorine-doped silica is employed as cladding: the amount of fluorine introduced in the silica matrix determines the value of the refractive index, being lower than that of pure silica or lightly RE-doped silica.

The reflection at the core-cladding interface must be very efficient in optical fibers to obtain useful light transmission over long distances: light is transmitted over the length of the fiber with a constant reflection angle. Scattering from the true path can occur due to irregularities in the core/cladding interface of the fiber, surface scattering at the interfaces, and scattering in the bulk material. Light will be scattered in proportion to the fiber length and depending on the angle of incidence: to be functional, long fibers must have an optical quality superior to that of short fibers.

A basic optical characteristic of a specific fiber configuration is its numerical aperture (NA): it can be thought of as representing the size or "degree of openness"of the input acceptance cone, as sketched in Figure 2.3. Mathematically, the numerical aperture is defined as the sine of the half-angle of the acceptance cone ($\sin\theta$). Snell's law can be used to calculate the maximum angle within which light will be accepted into and conducted through the fiber:

$$NA = n_0 \sin\theta_{max} = \sqrt{n_1^2 - n_2^2} \tag{2.2}$$

where θ_{max} is the half-angle, n_0 the refractive index outside the fiber end ($n_{air} = 1.0$), n_1 the refractive index of the core and n_2 the refractive index of the cladding. It should be noticed that this formula for the calculation of the numerical aperture does not take into

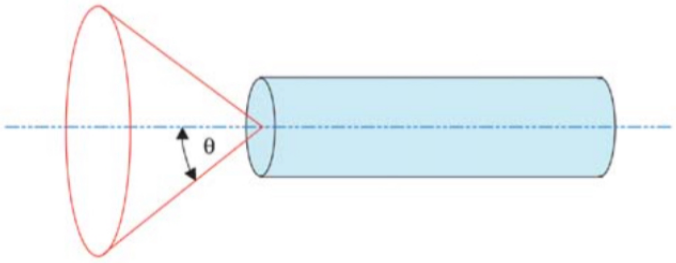

Figure 2.3: Schematic representation of the numerical aperture and the acceptance cone for a generic fiber.

account surface irregularities and diffraction, all of which tend to decollimate the beam bundle. Decreasing the cladding refractive index and/or increasing the core index will increase the NA, which in turn increases the full acceptance angle and the field of view.

2.4 Optical Properties and Point Defects in Silica

An amorphous solid is defined as a material lacking a long-range order at a microscopic level. However, the atomic positions are not randomly distributed in space, because glasses have a high degree of short-range order in common with crystals, as a consequence of the chemical bonding responsible for holding the solid together. Therefore, while the lack of long-range order implies randomness at large separation, the atomic-scale structure is highly nonrandom for a few interatomic distances about any given atom.

The silica structure is well described by the *continuous random network* model, as well as covalently bonded amorphous solids: it implies a general homogeneity of the glass and a gradual loss of correlation of atomic positions, which occurs without discontinuities. The parameters describing the matrix short-range order, such as bond lengths and angles, are continuous distributions in glass, whereas in quartz and crystals they assume discrete values.

The band structure of amorphous silica has been calculated through the *tight-binding* method and the presence of an energy gap of $E_g = 8.1$ eV between the valence and the conduction band has been demonstrated, although its value depends on the degree of order of the system.

The absence of a long-range order becomes of crucial importance when defects or impurities are introduced in the silica matrix: they originate continuously distributed energy levels inside the band gap, responsible for the so-called *inhomogeneous broadening* observed in the absorption and emission bands of amorphous materials, where all optical centers differ from site to site, due to the absence of translational symmetry.

During the last years, an extensive investigation of the optical response of SiO_2 has been performed both on undoped and RE-doped silica host matrix.

Point defects and impurities characteristic of amorphous silicon dioxide become responsible for absorption and emission bands when excited. They are optically active oxygen-deficiency-related centers, due to the presence of oxygen vacancy or surplus: the most common are the

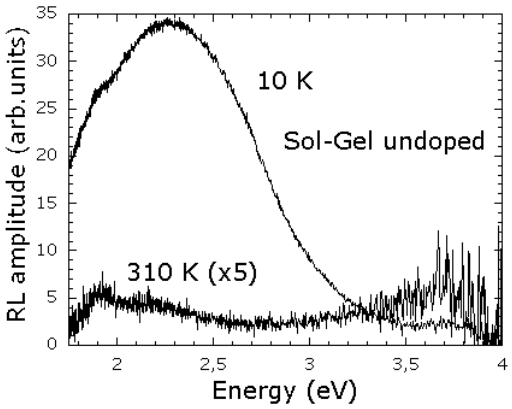

Figure 2.4: RL spectra of sol-gel undoped silica, at 10 K and at RT, under 20 kV X-rays excitation [21]: the main band at 2.4 eV can be ascribed to radiative de-excitation of self-trapped excitons, while the origin of the 2.7 eV band is assigned to the triplet-to-singlet transition of the twofold coordinated silicon defects.

non-bridging oxygen, occurring when an oxygen atom does not link two silicon atoms, and the *peroxil bridge*, precursor of the peroxil radical [39].

Point defects in pure silica, acting as shallow traps for free carrier created by ionizing radiation, can largely affect the scintillating properties of the material: according to their depth, they can cause slow tails in the scintillation time decay or lower the overall scintillation efficiency, by permanently trapping carriers. For this reason, thermally stimulated luminescence has been deeply studied [53]: a similarity between the glow curves of samples with different doping and obtained by varying synthesis parameters has been observed, pointing out the intrinsic nature of the traps responsible for the TSL signal. The hole nature of the investigated recombination centers demonstrated that oxygen deficient centers seem the most probable candidates to act as electron traps involved in the TSL process in silica, in order to achieve local charge compensation.
The random differences among the nearest-neighbors configurations are responsible for the broadening of trap energy levels in an amorphous matrix. The presence of a very large distribution of traps [53], ranging from a few meV up to nearly 2 eV, indicates that such electron traps can influence in a complex way the scintillation properties: shallow traps can be linked to the occurrence of a phosphorescence emission at room temperature (RT), while deep levels trap carriers in a stable way during irradiation.

The X-ray induced RL study of defect related emissions detected in undoped silica samples provided a valuable basis to analyze RL properties of the doped ones [21]. At low temperature (10 K), the sol-gel undoped silica displays a dominant emission band at around 2.4 eV, with weaker shoulders at 2.0 eV and 2.7 eV, as illustrated in Figure 2.4; by temperature increasing, a strong quenching of the main emission occurs and a weak and broad feature appears in the 4.0 eV region.

The incorporation of Ce in the silica host was found to quench the luminescence of the intrinsic silica centers [54]. In the investigation of structural and optical properties of sol-gel glasses, particular attention was paid to the influence of the concentration of the dopant ions and to

the different phases of the xerogel densification process governing the glass formation [20], in order to tune and optimize the glass synthesis parameters.

At high concentrations, namely above 1 mol.%, the spontaneous formation of RE-rich nanocrystalline aggregates, whose size depends on the concentration and the thermal treatments and extends up to several tens of nanometers, was disclosed and confirmed by morphological studies and Raman spectroscopy [55]. The clusters were proven to have a silicate-like structure: RE clustering in silica as $(RE)_2SiO_5$ may be favored by the survival of tetrahedral SiO_4 groups, which contribute to reduce the mismatch with the host matrix. Nanophase crystallization can be pursued by modifying synthesis conditions, to obtain a nanocomposite material where crystalline phases are embedded in amorphous SiO_2: they have been proposed as luminescent phases or as nanometric hosts for a different activator in the case of low intrinsic luminescence light yield [44].

Previous works focused on the properties of RE ions, such as Gd [56] and Tb [49, 57], and especially much attention was devoted to the study of Ce, as a good luminescent activator [20, 23]. Recently, Yb-doped silica fibers were investigated as a good solution for real time dosimetry applications [22, 50], and Pr-doped silica was studied for its fast transition, interesting for high energy physics applications [58].

2.4.1 Spectroscopy of rare-earth ions doped silica

As already introduced in the previous sections, rare-earth (lanthanide) ions are excellent activators for many compounds, and are characterized by an incompletely filled $4f$ shell. These orbitals are shielded from the surroundings by the filled $5s^2$ and $5p^6$ ones; therefore, the influence of the host lattice on the energies of the optical transitions within the $4f^n$ configuration is small, although it can be a source of information in the determination of the RE environment symmetry. Moreover, the transition probabilities can be strongly affected by the RE host site symmetry. Figure 2.5 reports a substantial part of the energy levels originating from the $4f^n$ configurations as a function of the number of electrons n for the trivalent ions: the width of the bars gives the order of magnitude of the crystal field splitting.

Optical transitions within the $4f^n$ configuration are forbidden as electric-dipole transitions by the parity selection rule ($\Delta l = 0$), but the uneven components of the crystal field, present when the RE ion occupies a crystallographic site without the inversion symmetry, mix a small amount of opposite-parity wave functions (like $5d$) into the $4f$ ones. In this way, the (forbidden) $4f - 4f$ transitions steal some intensity from the (allowed) $5d - 4f$ transitions and the parity selection rule is somehow relaxed. Thus, in the absorption and emission spectra, $f - f$ transitions can be seen as sharp and weak lines, so-called forced electric-dipole transitions: the luminescence intensity of these transitions is strongly influenced by the presence of multi-phonon relaxation phenomena among $4f$ levels and the occurrence of non-radiative recombination paths. Since the parity does not change, the lifetime of the excited state is long ($\sim 10^{-3}$ s).

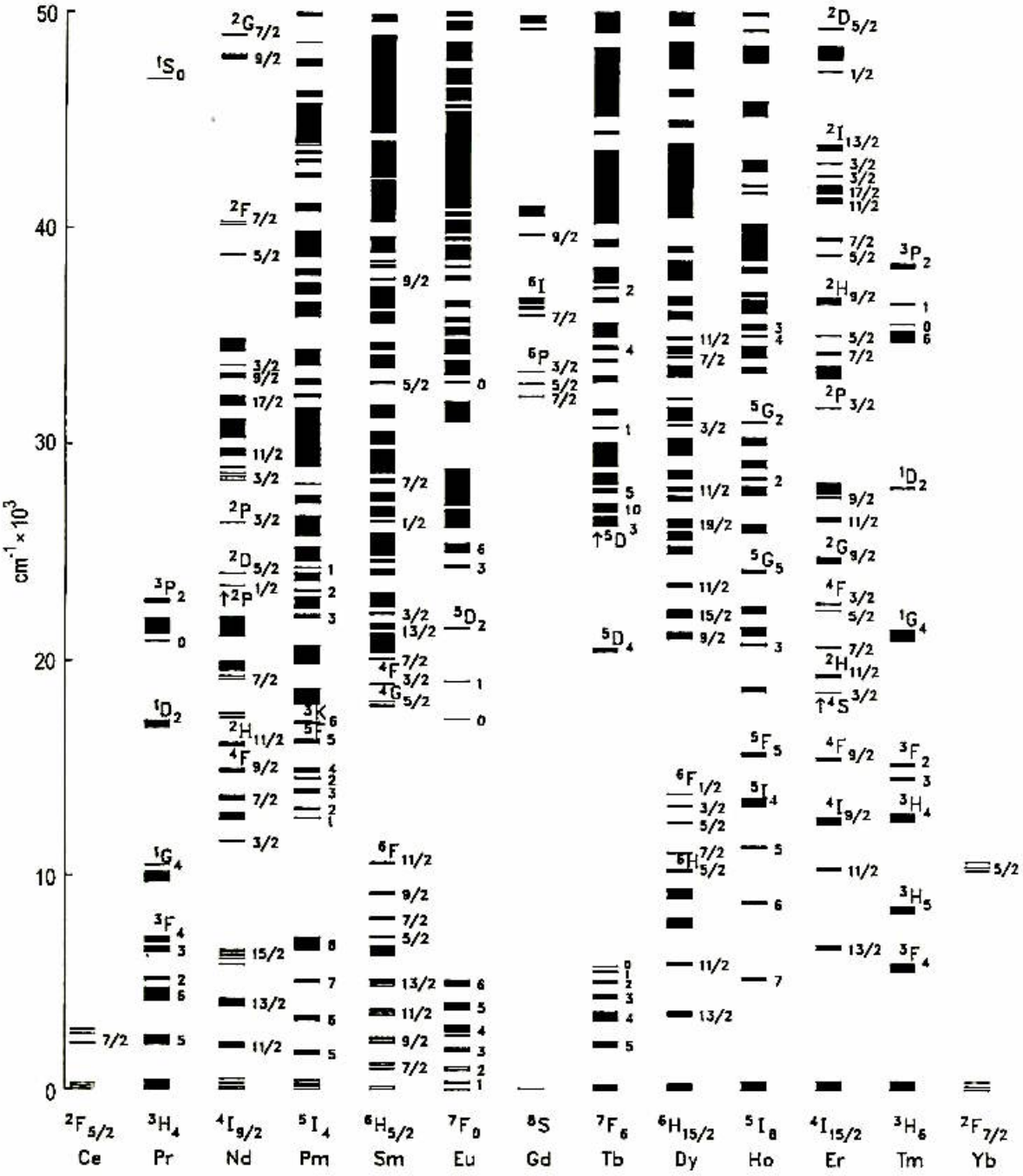

Figure 2.5: Energy levels of the $4f^n$ configurations of trivalent lanthanide ions [38].

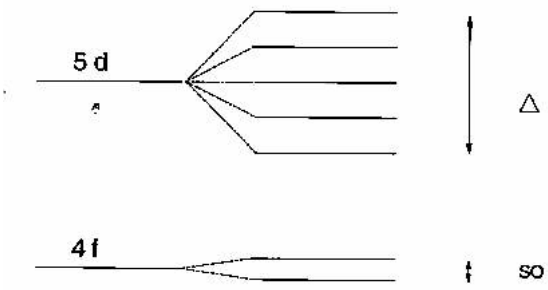

Figure 2.6: Simplified energy level scheme of Ce^{3+} ion: the spin orbit coupling (SO) splits the $4f$ level into two components and the crystal field (Δ) splits the $5d$ level into five components.

At higher energies, it is possible to observe allowed interconfigurational transitions, which consist in two different types: $4f^n \rightarrow 4f^{n-1}5d$ transitions and *charge transfer* (CT) transitions ($4f^n \rightarrow 4f^{n+1}L^{-1}$, where L is a ligand). Both are allowed and appear in the spectra as broad absorption bands, because of the strong electron-phonon interaction.
The trivalent ions that have a tendency to become divalent (Sm^{3+}, Eu^{3+}, Yb^{3+}) show charge transfer absorption bands in the UV; the trivalent ions that have a tendency to become tetravalent (Ce^{3+}, Pr^{3+}, Tb^{3+}) show $4f \rightarrow 5d$ absorption bands in the UV.
Since Ce^{3+} and Pr^{3+} were considered as activators for sol-gel silica in this work, a more detailed description of their energy levels is illustrated in the following.

Cerium (Ce^{3+})

The trivalent Ce has only one electron in the $4f$ shell, and its excited configuration is $5d^1$. The $4f^1$ ground state configuration yields to two spectroscopic terms ($^2F_{5/2}$ and $^2F_{7/2}$) separated by about 2000 cm^{-1} ($\sim$ 0.25 eV), due to spin orbit coupling. The $5d^1$ configuration is split by the crystal field in 2 to 5 components, whose total energy splitting amounts to some 15000 cm^{-1} ($\sim$ 1.86 eV). A schematics of the energy levels of Ce^{3+} is reported in Figure 2.6. The emission occurs from the lowest crystal field component of the $5d^1$ configuration to the two ground state levels; this gives to the Ce^{3+} emission the typical double-band shape, although in glassy matrices it appears as a single band because of the inhomogeneous broadening. Since the $5d \rightarrow 4f$ emission transition is parity allowed, its decay time is short, of the order of a few tens of ns.
The spectral position of the emission band depends on three factors: (1) covalency, which reduces the energy difference between $4f^1$ and $5d^1$ configurations, (2) crystal field splitting of the $5d^1$ levels, and (3) electron-phonon coupling.

In Figure 2.7, the optical absorption spectra of SiO_2:Ce sol-gel glasses are reported as an illustrative example of the influence of the valence state of the ion on the favored transition. The effect of the sintering atmosphere on the valence state of the ions, as introduced in Section 2.2, is remarked. The spectra obtained for glasses densified in reducing atmosphere (Ar/H_2) display the absorption band characteristic of Ce^{3+} ion and ascribed to the $4f - 5d$ transition.

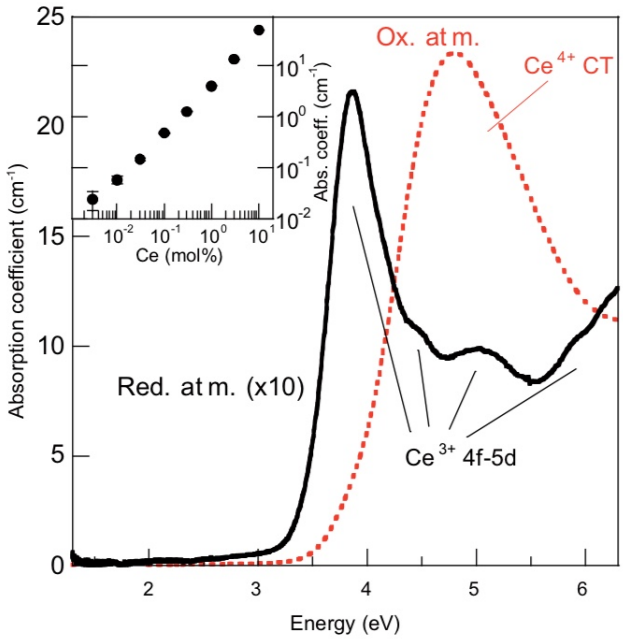

Figure 2.7: Absorption spectra of SiO_2:Ce sintered in oxidizing (red dashed line) and reducing (solid black line) atmosphere. The inset shows the expected linear dependence of the absorption coefficient on Ce nominal concentration [59].

At variance, optical absorption spectra of silica densified in oxidizing conditions (under O_2 flux) are dominated by the charge transfer band of Ce^{4+} ion centered at 4.8 eV; a shoulder at 3.9 eV, only barely detectable, indicates that a small fraction of Ce is nevertheless incorporated in its 3+ oxidation state [59].

When Ce-doped silica is exposed to ionizing radiation, the electrons and holes created are sequentially trapped at the excited and ground state of the luminescent center: this phenomenon gives rise to a temporary change in the valence state, as depicted by the sequence of reactions 2.3.

$$\begin{aligned} &Ce^{4+} + e \rightarrow Ce^{3+*} \\ &Ce^{3+*} \rightarrow Ce^{3+} + h\nu \ (scintillation\ light) \\ &Ce^{3+} + h \rightarrow Ce^{4+} \end{aligned} \tag{2.3}$$

Then the radiative recombination occurs by emission of light. Indeed, it has been shown that despite the much different number of Ce^{3+} ions present in the matrices of Ce-doped silica obtained in different atmospheres, contrary to expectation their RL efficiency does not significantly depend on the densification conditions, whether oxidizing [19] or reducing [59]. A typical room temperature RL emission spectrum of Ce-doped silica is displayed in Figure 2.8. Therefore, a role of Ce^{4+} in the recombination mechanism can be hypothesized and the following model is proposed. It may be possible that during X-ray irradiation, which causes temporary bond breaks, Ce^{4+} ions located in the silica matrix are temporarily reduced to Ce^{3+}, thus giving rise to the observed RL signal [43].

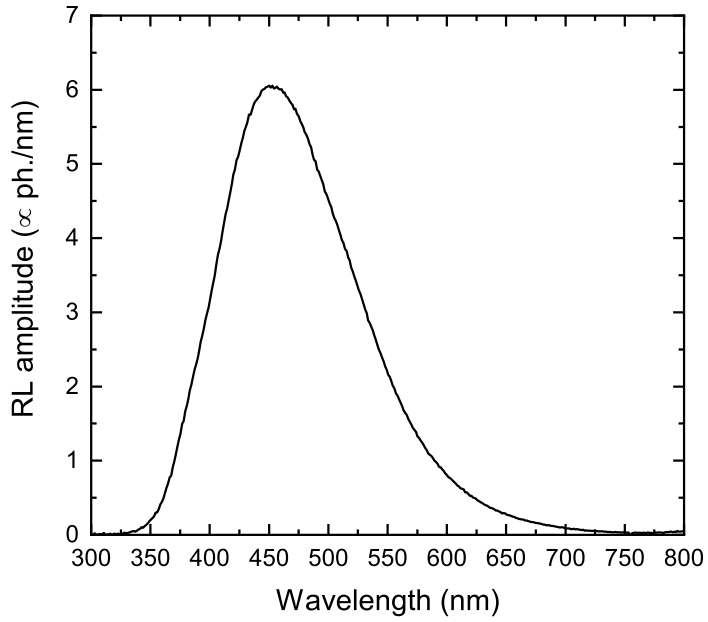

Figure 2.8: Room temperature radio-luminescence spectrum of Ce-doped silica.

Praseodymium (Pr^{3+})

Pr^{3+} ion ($4f^2$) shows both a broad emission band, ascribable to the allowed $5d \rightarrow 4f$ transition, and some sharp emission lines, related to intraconfigurational $4f \rightarrow 4f$ transitions. Concerning the latter, the emission color depends strongly on the host lattice: if the emission originates from the $^3P_0$ level, it may be red or even green, while it is in the red or near-infrared if the transitions start from the $^1D_2$ level. The decay time of the $^3P_0$ emission is quite short (tens of μs): there is no spin selection rule and also the $4f$ orbitals are probably more spread out in the lighter RE (with lower nuclear charge), facilitating the mixing with the opposite-parity states. If the excitation energy is high enough, also the $5d \rightarrow 4f$ emission band can be observed in the UV region.

Figure 2.9 gives the configurational coordinate diagram for Pr^{3+} in two different host lattices. If the offset of the $4f5d$ state is small, a radiative return to the $4f^2$ configuration has a higher probability than the non-radiative transition: this is case I in Figure 2.9, where excitation into I yields $d \rightarrow f$ emission (arrow 1). On the other hand, if the offset is large as it is for parabola II, excitation into $4f5d$ leads to emission from the $4f^2$ configuration after a non-radiative $4f5d \rightarrow 4f^2$ transition. The excited state of Pr^{3+} ion can emit, so that the Stokes shift can be measured and information on the relaxation process and on the parabola offset can be gained.

Emission and excitation spectra of Pr^{3+} in sol-gel silica are illustrated in Figure 2.10 [58]. The two main groups of transitions can be identified in both radio- and photo-luminescence (PL) emission spectra: the $5d-4f$ transition gives rise to a broad band peaking at around 300 nm. On the other hand, the emission lines in the VIS-NIR region are related mainly to the

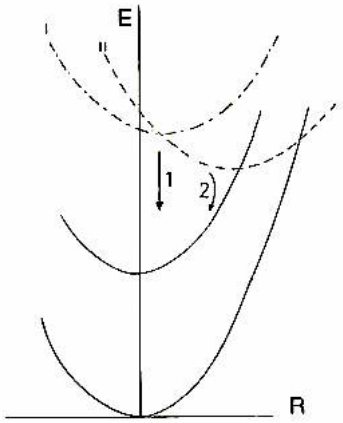

Figure 2.9: Schematic configurational coordinate diagram for Pr^{3+}: solid parabolas relate to the $4f^2$ configuration, whereas the broken parabolas indicate two possible situations for the $4f5d$ configuration [38].

transitions from the $^3P_0$ level to the various ^3H_j and ^3F_j sublevels. Referring to the energy level scheme of Figure 2.5, the $5d$ levels can be located below the $^1S_0 4f$ level, in agreement with the observation of the $5d - 4f$ emission.

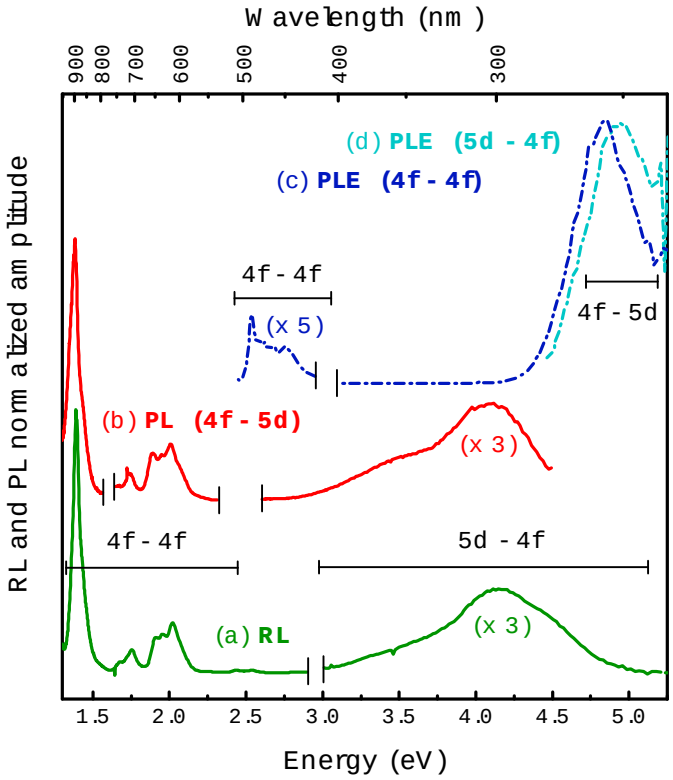

Figure 2.10: (a) RL and (b) PL emission spectra (λ_{exc} = 255–260 nm) of SiO_2:Pr normalized to the $4f - 4f$ emissions. (c) and (d) PL excitation spectra taken integrating the emission in the 580–670 nm and 305–330 nm range, respectively [58].

Chapter 3

Description of silica samples and influence of the fiber drawing

In this chapter, a description of the morphology and the geometry of the silica samples investigated in this work is provided, along with the details of the sol-gel synthesis process.

The structural, optical, and scintillation properties of sol-gel silica fibers are presented and compared to those of the parent bulk glass, in order to give an insight of the influence of the fiber drawing on the performances of this material. As already reported in Chapter 2.3, during fiber drawing the silica glass preform is heated to above its melting temperature under an applied axial tension; upon exiting the drawing furnace, the temperature of the fiber is abruptly lowered down from around its melting point of 1900 K to below 500 K. These drastic temperature drop in the glass has been demonstrated to maintain the amorphous character of silica network and a good dispersion of RE dopant ions.

However, a careful comparison of the fiber and bulk glass characterization reveals differences especially in the optical and mechanical properties; in fact, a readjustment of the Si-O network, induced by the high temperature treatments associated with the drawing process, is known to occur.

The effect of the fiber drawing on the radiation hardness of sol-gel silica will be extensively discussed in Chapter 4: the process turns out to positively induce a reduction of the concentration of radiation-induced defects acting as color centers, leading to an improvement of the resistance to radiation damage.

The aim of this chapter is to establish and put in evidence a correlation between the morphological and optical properties and the stage of the drawing process the investigated silica sample derived: a detailed characterization has been carried out from performs to fibers through the intermediate stages. In Section 3.2, photo-luminescence excitation (PLE) , Raman, and Fourier transform infrared spectroscopy (FTIR) are studied. In Section 3.3, the mechanical properties of sol-gel silica are investigated through a nanoindentation analysis, performed in collaboration with *Saint Gobain Research* (Aubervilliers, Paris, France).

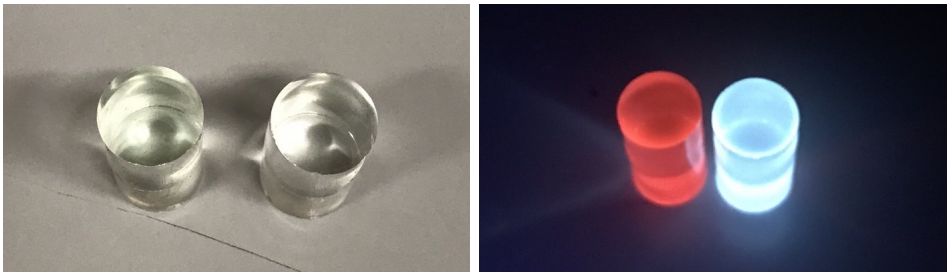

Figure 3.1: Pictures of Pr- and Ce-doped sol-gel silica preforms under visible light (left) and under UV light (right). Pr-doped silica (on the left of each picture) shows a greenish, although transparent, color because of the presence of Pr as dopant ion. If excited with UV light it emits in the red, due to the $f - f$ transitions: its $d - f$ transition occurs in a region of the UV spectrum not visible to the eye. Ce-doped silica has a blueish emission because of its $5d - 4f$ transition peaking at around 500 nm.

3.1 Description of the samples

Silica samples investigated in this work were produced in the Department of Materials Science at the University of Milano - Bicocca. Sol-gel method, already described in Section 2.2, was employed as synthesis technique, using tetramethylorthosilicate (TMOS) and Pr(III) or Ce(III) nitrate as precursors. Alcogels were obtained after gelation and subsequently dried in a thermostatic chamber for a few weeks. The obtained xerogels were densified up to 1225 °C under oxygen flux in order to obtain RE-doped preforms of 70 mm in length and 10 mm diameter. A slice of Pr- and Ce-doped preform is shown in Figure 3.1, under visible and UV excitation.

The preforms were then drawn at a temperature of about 1900 K into fiber by *Polymicro Technologies* (Phoenix, USA) and by the *Optoelectronic Research Center* (Southampton, UK) using a fluorinated silica cladding wrapping the RE-doped core, in order to guarantee the light guiding by the core-cladding interface, as discussed earlier in this work. The fibers were then left uncoated. The final core diameter is 0.6 mm and the final fiber diameter is 0.75 mm. Fibers were cut into 20 cm pieces for measurements purposes. The numerical aperture of these fibers is estimated to be approximately 0.17.

In Figure 3.2, a sketch of the neck-down from the preform dimension to the final fiber diameter is represented. The three intermediate samples are denoted as *melted samples* and can be considered as residuals of the drawing: they experienced the high temperature treatment of fibers, but still have a bigger diameter, and therefore are not completely drawn.

A picture of a Ce-doped silica fiber is displayed in Figure 3.4. The propagation of a narrow laser beam (2 μm wide) inside the optical fiber is captured: in the last portion of the fiber, also scattered light is visible. The laser wavelength (406 nm) falls in the tail of the Ce activators excitation band, and thus the blue light we can see can be ascribed to Ce emission. A model for the propagation of light and the calculation of the critical angles for the fibers studied in this work are sketched in Figure 3.5: the presence of RE dopants does not affect the refractive index of the pure silicon dioxide, which is assumed to be 1.4745, neglecting its dependence on the frequency. On the other hand, the presence of fluorine in the silica cladding decreases the refractive index to about 1.4648, depending on the fluorine concentration.

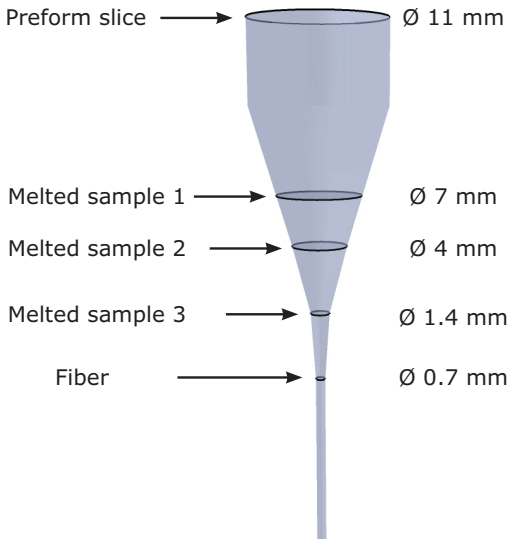

Figure 3.2: Schematic sketch of the final part of a drawn preform. The five samples investigated, marked by the arrows, were taken as representative of different stages of the fiber drawing process. Their diameters are also reported in the figure.

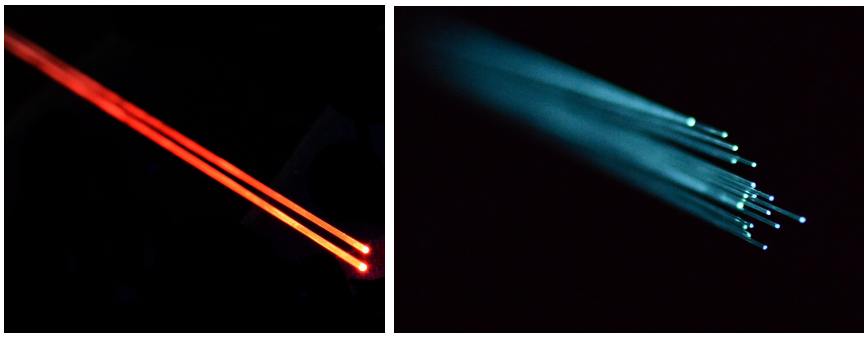

Figure 3.3: Pictures of Pr- (left) and Ce-doped (right) sol-gel silica fibers under UV light.

Pictures of the UV induced luminescence of Pr- and Ce-doped silica fibers are displayed in Figure 3.3: the light emitted by the activator centers and generated inside the core efficiently propagates along the fiber. A bright emission is also visible by eye.

Fiber samples with two different concentrations of Ce in the core, namely 0.0125 mol.% and 0.05 mol.%, were produced in order to determine the influence of the dopant concentration on the resistance to irradiation.

The results obtained on fiber samples were compared with the parent bulk glass to check how the fiber drawing affects the optical properties and radiation resistance of silica, as illustrated in Chapter 4. To this purpose, the following set of samples was prepared:

- a slice of Pr-doped bulk preform prior to drawing (⌀ 11 mm, thickness 2.3 mm), treated with post-densification RTT at about 1500 - 1700 °C for 10 s (the treatment is described in Section 2.2.1)

- a Pr-doped sample, cut from the residual of the fiber drawing process, with dimensions ⌀ 7 mm and thickness 2 mm

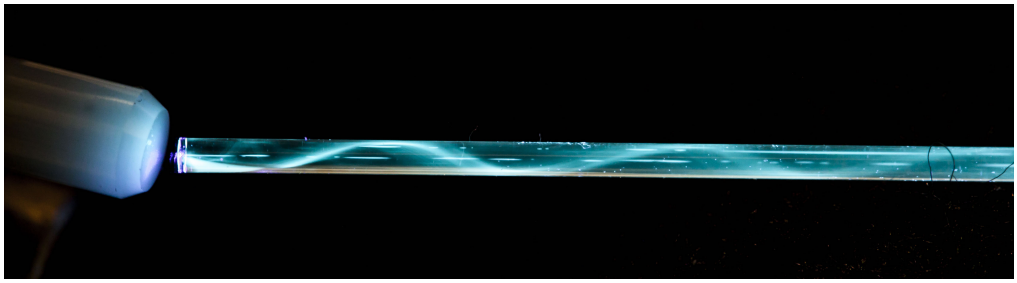

Figure 3.4: Picture of the propagation of a 406 nm laser beam 2 μm wide inside a silica-based optical fiber: the internal reflection phenomenon is clearly visible and various propagation paths are present in the first part of the fiber, depending on the injection angle of the laser beam.

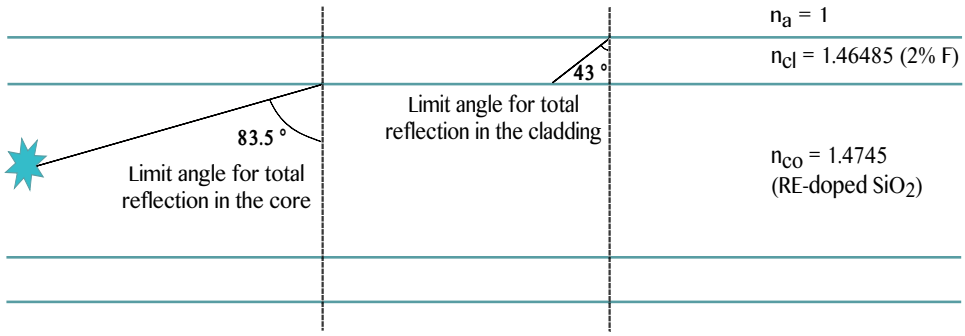

Figure 3.5: Model for the light propagation inside the core of a cladded fiber: the critical angles for total internal reflection in both the core and the cladding have been calculated.

- a Ce-doped melted sample with dimensions ⌀ 8.5 mm and thickness 2.5 mm
- Ce-doped fibers (length of 20 cm)

For the Raman and FTIR absorption spectroscopy, the following samples were used:

- a slice of Pr-doped preform (⌀ 11 mm, thickness 0.5 mm)
- a Ce-doped melted sample with dimensions ⌀ 8.5 mm and thickness 2.5 mm
- a piece of Ce-doped fiber (length of 10 mm)

Radio-luminescence and thermally stimulated luminescence analysis reported in Chapter 5 were performed on bundles of Ce-doped silica fibers.

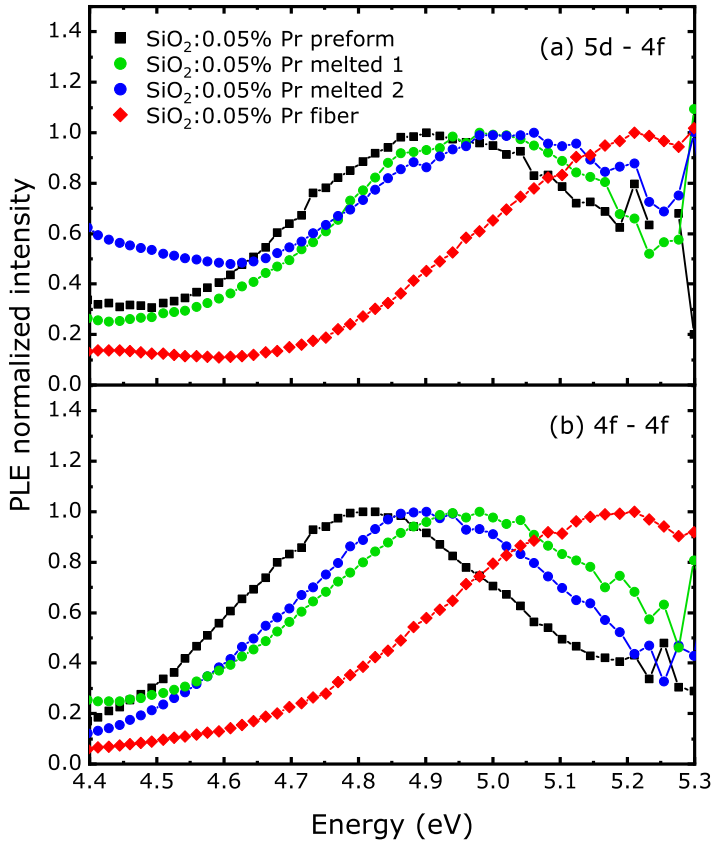

Figure 3.6: PL excitation spectra of SiO_2:Pr. Top panel: the $5d-4f$ emission region has been considered with E_{em} = 3.5 - 4.3 eV. Bottom panel: the integration has been performed on the $4f-4f$ emission range with E_{em} = 1.8 - 2.1 eV.

3.2 Optical properties

3.2.1 Photo-luminescence excitation

PLE spectra of Pr-doped silica are reported in Figure 3.6, in order to put in evidence a shift of the excitation bands towards higher energies going from preform to fiber through melted samples, as explained in the legend. The legend refers to the labels reported in Figure 3.2. The PLE spectrum of the $4f-4f$ emissions of Pr^{3+} features a main broad band peaking at about 5 eV, ascribed to the $4f-5d$ transition [60]. This band characterizes also the PLE spectrum related to the $5d-4f$ emission, although slightly shifted at higher energies and broadened. Interestingly, we observed (1) a high energy shift of both PLE spectra going from preform to fiber through melted samples; (2) a systematic shift towards higher energy of the excitation of the $5d-4f$ transition with respect to that of the $4f-4f$ lines, which progressively reduces from preform to fiber.

Concerning the former effect, it could be explained by crystal field modifications due to the fiber drawing. In fact, an analogous shift of the emission energy of the band peak is also observed in Figure 3.7, from 4.1 eV in the preform to 4.3 eV in the fiber.

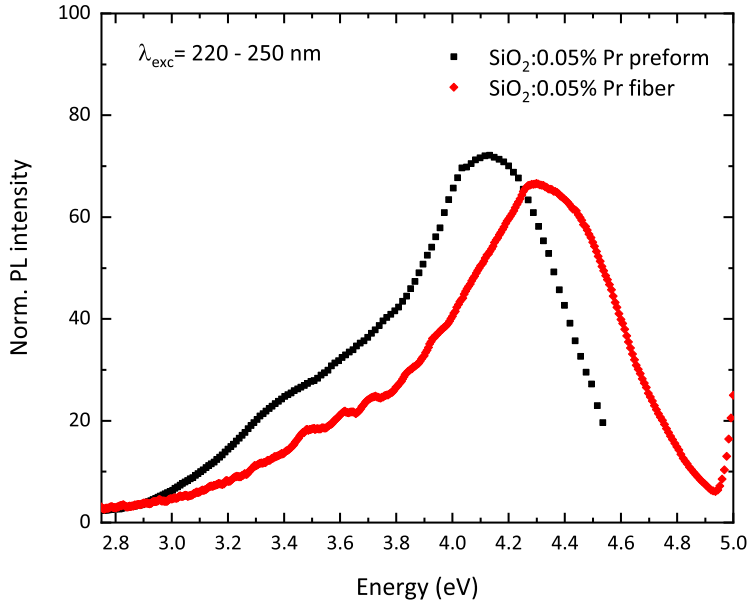

Figure 3.7: PL emission spectra (E_{exc} = 4.9 - 5.6 eV) of SiO_2:Pr in preform and fiber forms. The emission related to the $5d-4f$ transition occurring in the UV spectral range is reported.

The latter effect is more difficult to interpret: as a suggestion we can tentatively propose the interaction of Pr^{3+} energy levels with an optically active defect that is able to selectively excite in the short wavelength side the $5d-4f$ transition by non-radiative or radiative energy transfer, whose concentration is reduced by the drawing process. However, this phenomenon deserves further investigation.

3.2.2 Raman Spectroscopy

Raman spectra of RE-doped sol-gel silica at different stages of the drawing process were obtained by exciting with a He-Ne laser at 632.8 nm, and they are displayed in Figure 3.8: the labels refer to the vibrational assignments, made according to the literature [61, 62]. The general features resembling those corresponding to pure silica glass can be detected: Raman structures of SiO_2 are observed at about 440, 800, and 1060 cm^{-1} (ω_1, ω_3, and ω_4 bands, respectively) [63], corresponding to the Si - O symmetric stretching vibration of bridging oxygens and to the mixed stretching-bending Si - O vibration. The D_1 and D_2 peaks at 490 and 610 cm^{-1} are due to symmetric breathing modes of fourfold and threefold planar tetrahedra rings of SiO_2 [64].
No crystalline aggregates are evidenced, confirming that the fiber drawing process does not modify the amorphous character of the silica network and provides a good dispersion of RE ions [55].

Previous Raman measurements performed on sol-gel silica bulk and fibers revealed that the relative intensity of the D_1 peak with respect to the ω_1 band was higher in the fiber with respect to the bulk [23]. This is also in accordance with the results of the study of silica samples

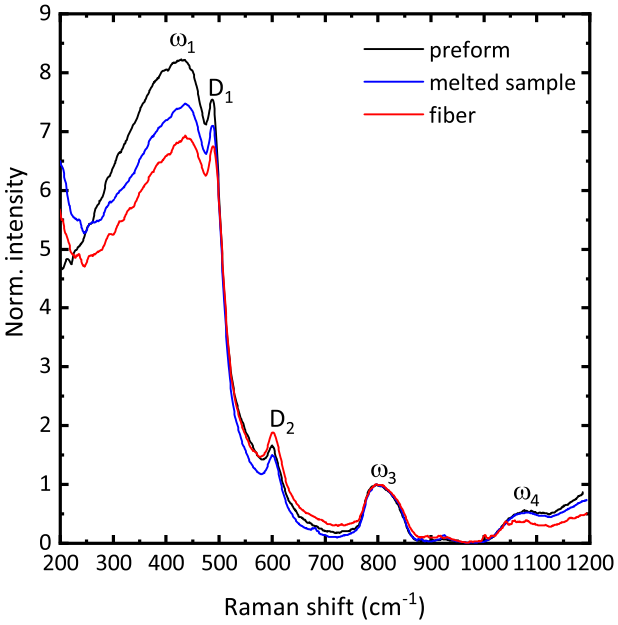

Figure 3.8: Raman spectra normalized to the ω_3 band maximum of sol-gel silica at various stages of the drawing process, as reported in the legend.

subjected to thermal treatments at different temperatures, where the formation of fourfold and threefold rings of SiO_2 tetrahedra was found to increase exponentially by temperature increasing [61]. A behavior, similar to that reported in [23], of the D_1 peak intensity compared to that of the ω_1 band as a function of the stage of the drawing process can be observed in Figure 3.8: in the fiber sample indeed, the intensities of the two structures are comparable, whereas the amplitude of the ω_1 band is more pronounced in the preform slice.

Raman spectra give also useful information on the local microstructure, crystalline order, and stress state of a material: indeed, peak shifting provides a direct relationship between processes conditions and residual stresses. Tensile stresses stretch the lattice and cause the Raman active peaks to shift towards lower wavenumbers; on the other hand, compressive stresses cause peak shifting towards higher wavenumbers [65]. The wavenumber shift is in proportion to the magnitude of the residual stress. Raman spectroscopy can thus be considered a non-intrusive stress measurement technique, which can be coupled to the nanoindentation method in the next section, for the investigation of residual stresses.

In samples subjected to high temperature treatments (melted and fiber sample), Raman peak position was found to slightly shift to higher wavenumbers as illustrated in Table 3.1, without any decrease of the peak width with respect to that of the bulk preform, confirming again that the fiber drawing maintains the amorphous features of silica glass.

Therefore, the fiber drawing process might have left thermally induced residual stresses in the fibers, possibly caused by the rapid cooling of the glass and by differences in the coefficient of thermal expansion of the fluorinated silica cladding and the RE-doped fiber core. Indeed, the thermal history experienced by the fibers can create axial, tangential and radial stresses.

Table 3.1: Position of the maximum of the D_1 and D_2 peaks for the three samples investigated. A little shift to higher wavenumbers occurs in the thermally treated samples.

	Preform	Melted	Fiber
D_1 (cm^{-1})	486.6	487.7	488.7
D_2 (cm^{-1})	600.1	601.9	602.2

Table 3.2: Concentration of residual OH groups in the three samples taken from different stages of the fiber drawing. The evaluation of the OH content was made following the procedure illustrated in [66].

	Preform	Melted	Fiber
OH content (ppm)	300	180	160

3.2.3 Fourier Transform Infrared Spectroscopy

FTIR spectroscopy can be applied to detect the vibrational spectra of OH groups, as belonging either to residual H_2O or to Si-OH, and the possible shift of the intrinsic Si-O-Si overtone stretching mode, as a consequence of the high temperature treatment.

FTIR spectra in the 700 - 4000 cm^{-1} region are reported in Figure 3.9, in reflection (left) and transmission (right) mode, for the three Ce-doped silica samples belonging to different stages of the drawing process, already measured by Raman spectroscopy. The fundamental structural band (ν_1) at 1120 cm^{-1} can be identified as related to the Si-O-Si bond antisymmetric stretching; the overtone (ν_2) of the fundamental structural band is visible at 2260 cm^{-1}, related to the average of the distribution of the Si-O-Si bonding angle, along with the Si-OH stretching mode at 3670 cm^{-1}, useful to monitor the OH presence [19].

The Si-OH concentration was evaluated by following the calibration procedures proposed for fused silica [66], based on the measurement of either the peak amplitude or the area subtended to the absorption band at 3670 cm^{-1}. The results are reported in Table 3.2: the high temperatures of the drawing process turned out to induce a reduction of the OH content in silica.

The weak and broad shoulder at around 2650 cm^{-1}, more pronounced in the FTIR spectrum related to the preform sample, could be ascribed to the crystal field transition between the $^2F_{5/2}$ and $^2F_{7/2}$ manifolds due to the unique $4f$ electron of Ce^{3+}; it can be considered a signature of Ce^{3+} embedded in the disordered silica matrix [67].

The fundamental Si-O-Si stretching mode and its overtone were found to shift to higher frequencies with the increase of the average Si-O-Si bond angle in the glass structure; a slight shift of less than 10 cm^{-1} between the preform and the treated samples is fairly visible in the left panel of Figure 3.9. It can be also associated to a densification of the glass matrix [68]. This observation can be considered another signature of the occurrence of a modification of the silica network upon thermal treatments.

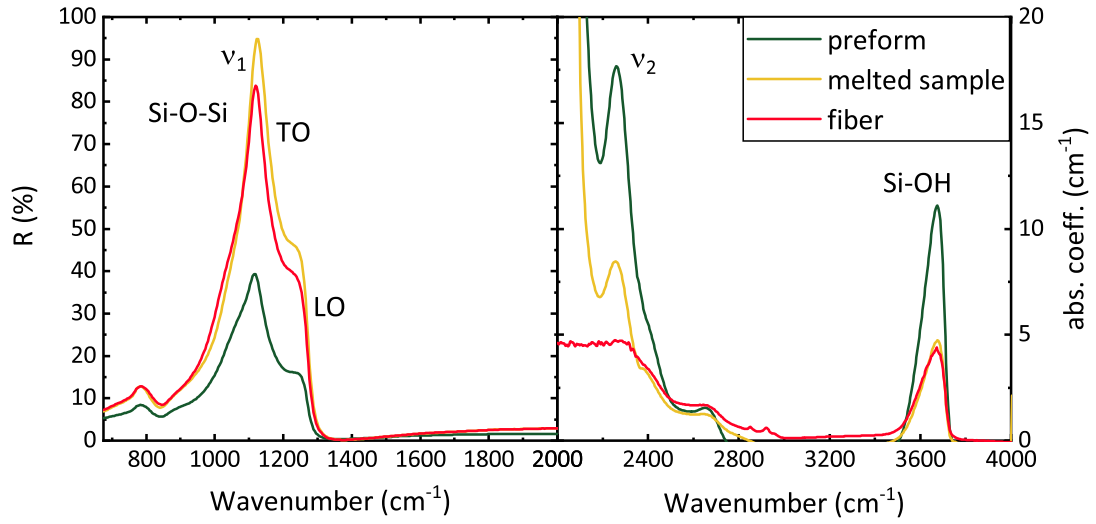

Figure 3.9: Infrared bands related to the fundamental structural band at 1120 cm^{-1} of the Si-O-Si bond antisymmetric stretching in reflection mode (left). Optical transmission spectra in the infrared spectral region (right): the main features are related to the overtone of the fundamental structural band at 2260 cm^{-1} and to the Si-OH stretching mode at 3670 cm^{-1}.

3.3 Mechanical properties

Nanoindentation technique is a powerful tool for determining the hardness, elastic modulus, and other mechanical properties of materials at small scales. Its attractiveness is largely due to the fact that mechanical properties can be determined directly from indentation load and displacement measurements, without the need to image the hardness impression. Moreover, it allows an insight of the mechanics of the elastic-plastic behavior of materials, and a direct measurement of residual stress levels. Exhaustive reviews of the method, from its introduction to the latest advancements, can be found in [69, 70].

A set of silica samples was measured by nanoindentation at Saint Gobain Recherche (Aubervilliers, Paris, France) in order to deepen the knowledge about the potential influence of the fiber drawing process, the irradiation, and the type of RE dopant ions on the mechanical properties of sol-gel silica glass. In particular, the following samples were measured:

- Corning 7980 bulk glass, used as reference
- two slices of Pr-doped preform, one irradiated with X-rays up to 1 kGy and the other not irradiated
- two Ce-doped melted samples, one subjected to irradiation with 1 kGy X-rays and the other not irradiated
- three pieces of silica fibers, doped with Pr, 0.05 % Ce, and 0.0125 % Ce, embedded in resin

The measurements were performed using a cube-corner indenter tip and varying the applied load in the 1 - 10 mN range.

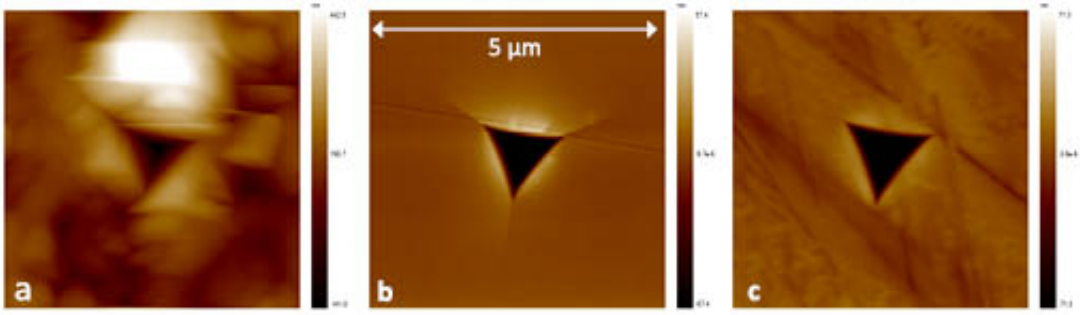

Figure 3.10: Raster scan with a nanopositioning stage of the residual impressions after an indentation in sol-gel silica glass with a cube-corner indenter at 9 mN. Width of field 5 μm. (a) Sol-gel silica preform. (b) Sol-gel silica sample after a high temperature treatment. (c) Sol-gel silica fiber core. The images were used to evaluate the length of the cracks, if present.

Images of the residual impression after a nanoindentation measurement with maximum load 9 mN are reported in Figure 3.10: for the bulk preform (panel a), the nanoindentation test did not provide any useful result, probably due to the poor quality of the sample surface, which resulted isotropically rough even after polishing. This observation can be correlated with the absence of any high temperature treatment on this sample.
The formation of cracks is visible only for the melted sample (panel b), because in the case of fibers (panel c), cracks are present only at higher maximum load: this suggests the occurrence of an increase of the hardness of silica induced by the drawing process.

A second set of measurements was performed on fibers by increasing the maximum load in the range 10 - 100 mN and revealed that the critical load for fiber samples is around 20 mN: the first cracks appeared when this value was reached. The presence of a critical load for cracks formation points towards the existence of strong compressive residual stresses and to the increase of toughness in fiber samples. Above 60 mN of applied load, the nanoindentation impression images do not provide any useful information for the evaluation of crack length because of the occurrence of a high level of chipping. Figure 3.11 shows an image obtained at the microscope of the residual impressions in the fiber core, highlighted in red, related to this latter set of measurements.

Cracks formed under the cube-corner indentation are "quadrant" or quarter-penny shaped: it was demonstrated that cube-corner indentation crack lengths can provide a good estimate of residual stress with the distinction that stresses are sampled over small volumes [71]. It is the residual component of the contact stress field that determines the ultimate radial crack size. From the direct measurement of the crack traces c on the indented surface as a function of the load P, the toughness K_c can be calculated via Eq. 3.1. It is an important fracture parameter, defined as the ability of a material to absorb energy and plastically deform without fracturing. Eq. 3.1 is valid only in the case of a cube-corner indenter geometry. In Figure 3.12, the characteristic dimensions of quarter penny-like/median crack are shown: the parameter c is the one involved in the evaluation of K_c [72].

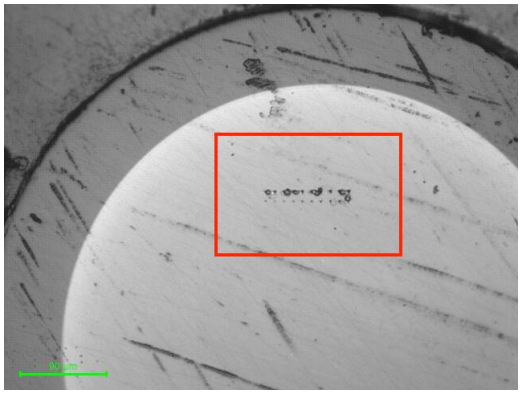

Figure 3.11: The sequence of nanoindentation measurements, highlighted in red, on the fiber core is visible with the use of a microscope. The image was acquired in transmission mode.

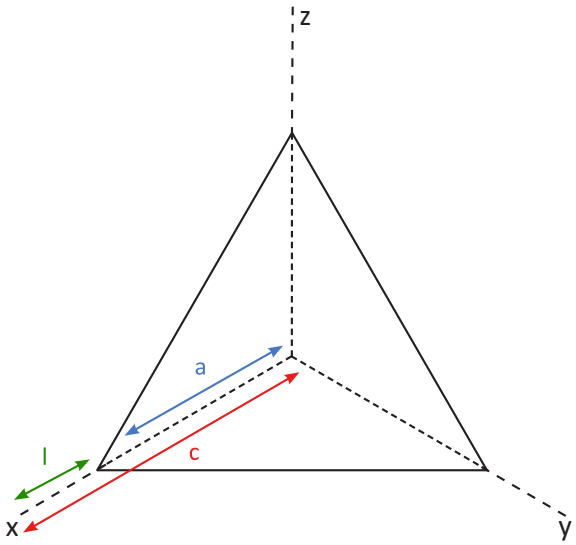

Figure 3.12: Schematic of a cube-corner indentation site. Three such cracks occur, one at each cube-corner site, if the critical load is reached. The characteristic dimensions l, a, and c of quarter penny-like radial/median crack and hardness impression are shown.

$$K_c = 0.036\sqrt{\frac{E}{H}}\frac{P}{c^{3/2}} \tag{3.1}$$

In Figure 3.13, load-displacement curves are reported as a function of increasing maximum load (left panel) and as a function of the stage of the drawing process (right panel). For the bulk sample, no significant results were obtained: therefore, only the curves related to a melted sample and a fiber sample are displayed. Since the indenter tip is very sharp, it was possible to separately measure the fiber core and cladding, in order to check the influence of fluorine on the hardness of silica.

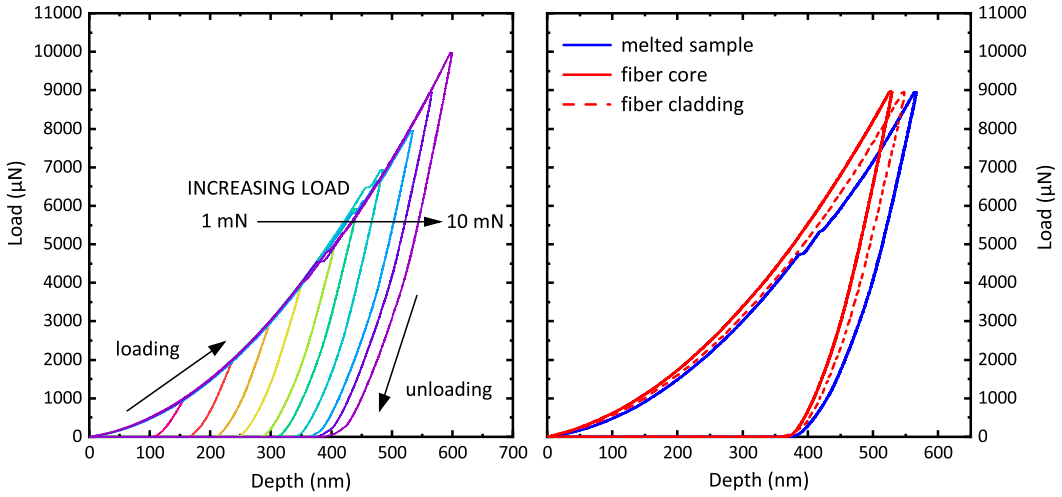

Figure 3.13: Load-displacement curves for nanoindentation measurements in sol-gel silica, showing elastic-plastic behavior. Left panel: load-displacement curves as a function of increasing load. The formation of cracks is evident in the steps of the loading segment. Right panel: load-displacement curves for samples from different stages of the drawing process.

Assuming a sharp transition from elastic to plastic behavior, the load-displacement curve can be modeled according to [70]:

$$P = E^* \left[\frac{1}{\sqrt{\pi}\tan\alpha} \sqrt{\frac{E^*}{H}} + \left(\frac{2(\pi - 2)}{\pi} \right) \sqrt{\frac{\pi}{4}} \sqrt{\frac{H}{E^*}} \right]^{-2} h^2 \tag{3.2}$$

where P is the load, E^* is the effective elastic modulus, H is the hardness, assumed to be constant, and α is the equivalent cone angle, dependent on the indenter tip. The hardness is the measure of the resistance to localized plastic deformation induced by either mechanical indentation or abrasion; it is dependent on the material microdurability and cannot be considered a fundamental material property, but represents instead an arbitrary quantity used to provide a relative idea of material properties. The elastic modulus E^* measures the resistance of a material to be deformed elastically when a stress is applied and is evaluated as the combined elastic modulus of the contacting bodies, namely the indenter and the sample: in practice, the indenter is usually made of diamond, and so E^* is dominated by the elastic properties of the investigated specimen for most materials. It can be calculated via:

$$\frac{1}{E^*} = \frac{(1 - \nu^2)}{E} + \frac{(1 - \nu'^2)}{E'} \tag{3.3}$$

where $E' = 1141$ GPa and $\nu' = 0.07$ describe the elastic modulus and Poisson's ratio of the diamond indenter respectively; the value of ν for fused silica has been considered. This formulation takes into account the fact that elastic displacements occur in both materials.

The important feature of Eq. 3.2 is that the load depends on the square of the displacement. In the portion of the curve related to the loading phase, the formation of cracks is pointed out by the appearance of a step in the curve, visible only for the highest applied loads.

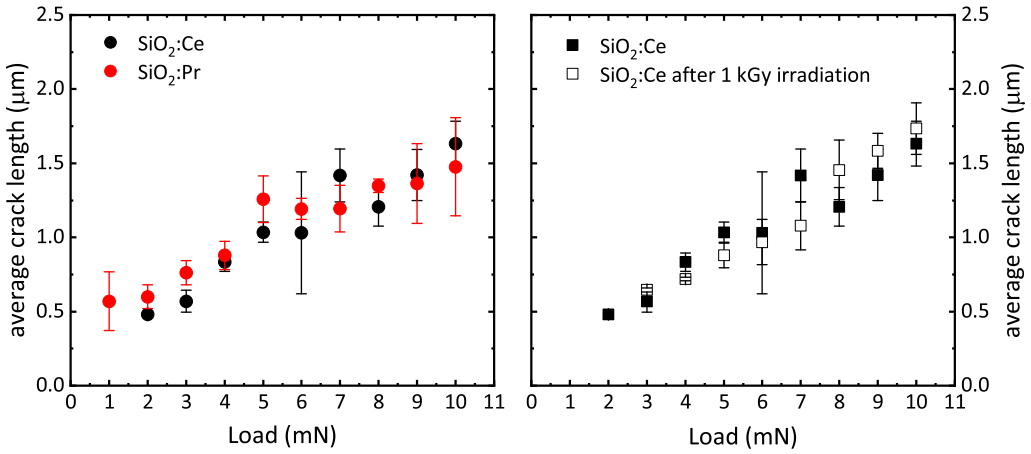

Figure 3.14: Crack length as a function of increasing load: each data point corresponds to the average over the three cracks when they occur. Left panel: same stage of the drawing process but different dopant RE ions. Right panel: for the same sample, the effect of X-ray irradiation is investigated.

During unloading, there is some degree of elastic recovery as the elastically strained material outside of the plastic zone relaxes and tries to resume its original shape. This is prevented by happening entirely by the presence of the plastic zone; therefore a residual impression remains in the surface, like those reported in Figure 3.10. In fact, deformation during loading is assumed to be both elastic and plastic in nature.
On the load-displacement curves, elastic recovery is evidenced by a reduction in displacement with decreasing load. In the case of sol-gel silica, an elastic-plastic contact occurs; indeed, the unloading curve is different from the loading curve and the area enclosed between them represents the energy lost (as heat) during plastic deformation. In the ideal case of a fully elastic contact, the unloading curve lies on top of the loading curve. The unloading behavior is assumed to be entirely elastic.

In order to evaluate the hardness of the material, the initial part of the unloading curve is the most significant: in principle, the hardness can be obtained by fitting a polynomial expression of the second order to the unloading data, according to Eq. 3.2, and then find the derivative and the slope. However, it can be noticed that the unloading response is fairly linear in the initial part, and thus the contact appears to have a linear dependence on the load, justifying the use of a linear fit to the upper portion of the unloading data.

The average cube-corner indentation crack length as a function of load is reported in Figure 3.14 for Ce and Pr-doped silica (left panel), and for Ce-doped silica before and after 1 kGy X-ray irradiation (right panel). Since the length of the cracks formed in an indentation measurement is the most important parameter to characterize the mechanical behavior of a material, the comparison of the results obtained for Ce- and Pr-doped silica shown in Figure 3.14 could allow the investigation of the role of the dopant specie in the mechanical properties of RE-doped silica. The incorporation of Pr ions, with respect to Ce ions, does not seem to influence the nanoindentation response; moreover, also the X-ray irradiation does not turn out to affect the mechanical behavior of silica.

Table 3.3: Average values of hardness, elastic modulus, and toughness evaluated for the silica samples measured by nanoindentation. Missing data when no formation of cracks is observed. The uncertainty associated to the data can be ascribed to the great scattering of crack length data.

	Corning 7980	Preform	Melted	Fiber
H (GPa)	8.6 ± 0.5	8.2 ± 2.3	8.1 ± 0.4	9.3 ± 0.7
E (GPa)	72 ± 3	78 ± 11	73 ± 3	79 ± 3
K_c (Pa · $m^{0.5}$)	580 ± 130		547 ± 100	875 ± 260

In Table 3.3, the parameters describing the mechanical properties of silica samples are listed and compared to those related to a sample of bulk glass Corning 7980 used as reference. Nanoindentation measurements on the preform sample were affected by a poor quality of the rough surface; therefore, a bigger uncertainty is associated to the obtained parameters, ascribed to a great scattering of the data. In the fiber an increase in the values of H and E was evidenced, compared to the other samples, thus confirming a strengthening of the hardness induced by the fiber drawing. Toughness could be evaluated only when the formation of cracks occurred: also in this case, the value of K_c resulted higher in the fiber. Furthermore, the parameters obtained for sol-gel silica samples are close to those of the reference bulk glass.

We can conclude that the fiber drawing positively influences the hardness of silica: the fiber form turned out to be a harder material, more resistant to the application of an external load, with respect to the preform it derives from.

Chapter 4

Radiation damage and formation of radiation-induced defects

As introduced in Section 1.2.2, the interaction of ionizing radiation with inorganic scintillating materials involves the host matrix, intrinsic defects as well as impurities, whose presence enhance the probability of formation of radiation-induced color centers, and invariably creates radiation damage, causing a loss of transparency and leading to severe degradation of the scintillation performances.

The use of RE-doped silica fibers in HEP experiments requires an extremely good radiation hardness of the material, because of the harsh environment in which it would be employed. The most challenging requirements are expected in the High Luminosity Large Hadron Collider phase [73], in which the radiation-induced absorption coefficient of the detector material should be kept below 1-2 m^{-1}, even after a cumulated dose of 300 kGy. Radiation tolerance requirements strongly depend on the kind of experiment and on the position of the material in the detector with respect to the beam line.

Silica fibers have been recently proposed as the active scintillating material in sampling electromagnetic calorimeters [10, 74], or as the scintillating component in dual-readout calorimeters [11, 75], coupled with undoped fibers exploiting Cherenkov emission. Their use as wavelength shifters for the collection and transport of light in HEP detectors has also been investigated [46].

The degradation of the scintillation and optical properties and of the attenuation length of Ce-doped crystalline fibers during irradiation has already been intensively studied: the response of LuAG:Ce [11, 12] and YAG:Ce [76] single crystal fibers has been investigated under high levels of γ and proton irradiation fields.

In this chapter, a detailed study of the optical properties under X-rays and γ irradiation and of the radiation resistance of Pr- and Ce-doped sol-gel silica fibers is presented. The formation of radiation-induced defects is evidenced in the optical absorption spectra as new absorption bands: the dependence of the radiation-induced absorption coefficient on the amount of delivered dose is investigated. The possibility of a spontaneous recovery of the damage at RT

or after annealing treatments at high temperature is also disclosed. The attenuation length of fiber-shaped silica is evaluated for different concentrations of RE ions and for both as-received and irradiated materials. The effect of the high temperature treatments, undergone during the fiber drawing, is discussed as well as the influence of the dopant concentration on the radiation resistance of silica glasses.
The content of this chapter has been published in [58] and [77].

4.1 Degradation of the optical transmission of Pr-doped silica

Praseodymium dopant has been considered as an interesting luminescent activator, because of its fast (a few tens of ns) $5d-4f$ transition leading to an emission band located in the UV spectral region [78]. The properties of Pr^{3+} ions incorporated in various crystalline matrices [79, 80, 81], perovskite compounds [82, 83] or silicates [84] have been extensively studied. In few cases, luminescence and scintillation properties of SiO_2:Pr glass have been considered in view of scintillator or laser applications [85, 86].

In this section, the resistance of Pr-doped sol-gel silica under X-ray irradiation fields up to 1 kGy is investigated: as a candidate for applications in HEP detectors, this material should have an extremely good radiation hardness. The doses applied in this study are far away from the levels reached in the severe environment of HEP experiments, but are enough to induce the formation of color centers affecting the optical transparency and scintillation performances of SiO_2:Pr, as reported in the following.

4.1.1 Decay time of Pr^{3+} luminescence in silica

At first, the decay time of the $5d-4f$ transition of Pr^{3+} in a silica host has been evaluated, both related to PL and to scintillation emission. PL time decay measurements were carried out with a FLS980 Spectrometer (Edinburgh Instruments) featuring a pulsed light emitting diode (EPLED-250) with 920 ps pulse width as excitation source. The detector was a Hamamatsu R928P photomultiplier tube (PMT) working in time-correlated single photon counting (TCSPC) mode.
The time response of the X-ray excited luminescence was measured using a custom-made pulsed X-ray system consisting of an ultrafast laser (200 fs pulses at 165 kHz), a light-excited X-ray tube, a Hamamatsu R3809U-50 microchannel PMT and an Ortec 9308 ps time analyzer. The impulse response of the system is 100 ps full width at half maximum (FWHM) [87].

In Figure 4.1, pulsed scintillation (X-RL) and PL ($\lambda_{exc} = 250$ nm, $\lambda_{em} = 295$ nm) time decay measurements in a 2 μs time window are reported together to allow their comparison. Distorted, not pure exponential decays are observed in both curves. The decays have been fitted in an operative way by the sum of exponential contributions.
The PL decay is characterized by an initial fast component with 5 ns decay time and relative intensity 30 %, and by a main contribution (70 %) of about 35 ns.

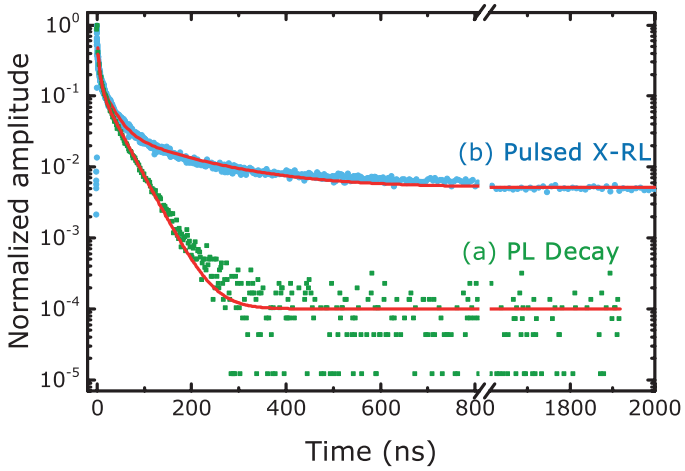

Figure 4.1: (a) PL decay ($\lambda_{exc} = 250$ nm, $\lambda_{em} = 295$ nm) and (b) spectrally unresolved scintillation decay, obtained with a pulsed X-ray source, of Pr^{3+} luminescence. Red lines: exponential fit to the experimental data. The deconvolution of the PL decay signal with the PL impulse response function was carried out. Data normalized to their initial value.

On the other hand, the scintillation decay features a faster part fitted by two components with 2.7 ns (10 %) and 25 ns (40 %) decay times, accompanied by a much slower contribution with about 160 ns decay time (50 %).
The initial decay distortions observed in both curves and approximated by the fit as very fast components are attributed to the presence of non-radiative recombination paths and/or energy transfer processes. The contribution with 25–35 ns decay time is representative of the $5d_1 - 4f$ transition of Pr^{3+}. The slow component, evidenced in the scintillation decay, can be attributed to the presence of defects temporarily trapping free electrons and then releasing the carriers with their characteristic emptying time, even if we cannot exclude the contribution of the slower emission in the red spectral region related to $4f - 4f$ transitions, already described as typical of Pr^{3+} ions.

4.1.2 Defect-related induced absorption and radiation damage

A picture of a Pr-doped glass prior to irradiation is shown in Figure 4.2(a): the glass appears transparent and colorless. After exposure to 1 kGy X-ray irradiation, the sample got a brownish color in the core, where the luminescent activator is present.
The X-ray irradiation was performed by a Machlett OEG50 X-ray tube with tungsten anode, operated at 32 kV: at this voltage, the X-rays generation mechanism exploits mainly the *bremsstrahlung* process, leading to a characteristic continuous distribution energy spectrum.

Figure 4.3 illustrates the optical absorption (OA) spectra of SiO_2:Pr before and after X-ray irradiation, superimposed to the RL emission spectrum. OA measurements were acquired by a Varian Cary 50 Spectrophotometer. RL measurements, reported here and in the following, were performed using a homemade apparatus featuring a liquid nitrogen-cooled, back-illuminated and UV-enhanced CCD detector (Jobin-Yvon Spectrum One 3000) coupled to a monochromator (Jobin-Yvon Triax 180) equipped with a 100 grooves/mm grating as detection system. RL excitation was obtained by X-ray irradiation through a beryllium window, using a Philips

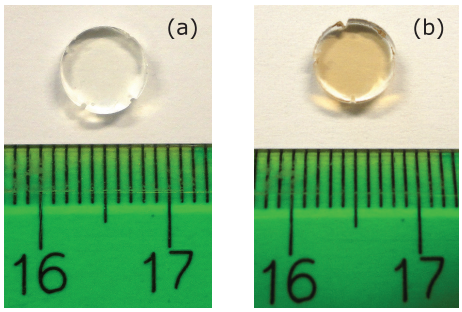

Figure 4.2: Picture of SiO_2:Pr before (a) and after (b) 1 kGy X-ray irradiation.

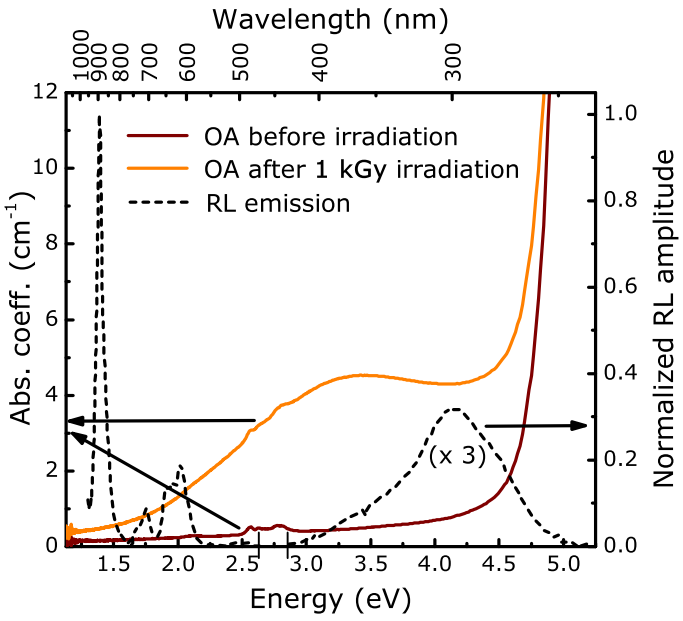

Figure 4.3: Solid lines: optical absorption spectra of SiO_2:Pr before and after 1 kGy X-ray irradiation. Dashed line: RL emission spectrum under 20 kV X-ray excitation.

PW2274 X-ray tube with tungsten anode operated at 20 kV. RL spectra were corrected for the spectral response of the acquisition system. No shape modifications occur in the RL emission spectrum after exposure to ionizing radiation.

In both OA spectra, the Pr^{3+} absorption lines from the $^3H_4$ ground state to the $^3P_2$, $^3P_1$ and $^3P_0$ excited states are fairly visible at 2.58, 2.64, and 2.75 eV, respectively. Strong absorption is also detected above 4.5 eV, likely related to the $4f - 5d$ transition of Pr^{3+} and possibly also to defect-related bands.
In addition, after irradiation, a broad absorption band becomes evident, overlapping with the $5d - 4f$ emission in the UV region (at about 4.0 eV). The UV light emitted by the RE luminescent centers can thus be likely re-absorbed by the material itself.

A comparison between the response of a slice of SiO_2:Pr preform and a melted sample, described in Section 3.1, has been carried out to understand the effects of high temperature treatments on the radiation resistance of the material. For both samples, the radiation-induced absorption spectra, obtained as the difference between the spectra acquired after irradiation

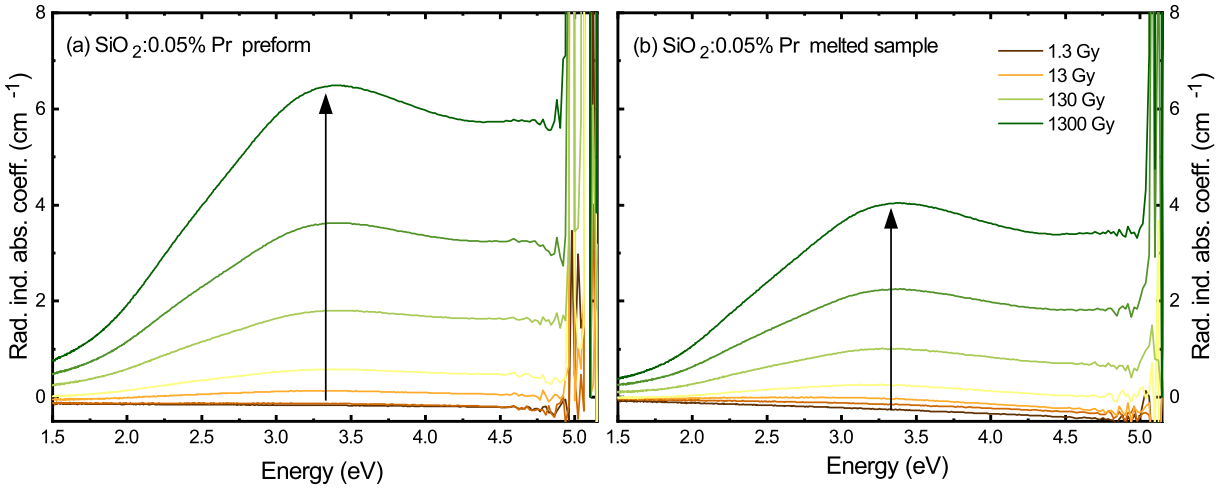

Figure 4.4: Radiation-induced optical absorption spectra of (a) SiO_2:Pr preform and (b) SiO_2:Pr melted sample as a function of increasing dose. In the melted sample, the induced absorption coefficient is significantly lower.

and the spectrum obtained before, as a function of increasing dose up to about 1 kGy are reported in Figure 4.4. A monotonic increase of the absorption is noticed in both cases, without any substantial shape modification.
A significantly lower damage occurs in the melted sample with respect to the as-prepared preform, pointing towards a positive effect of the high temperature treatment on the radiation resistance of doped silica.

In Figure 4.5, the numerical fit of the radiation-induced absorption spectrum in terms of the minimum number of Gaussian components necessary to obtain a satisfactory spectrum reconstruction is shown: the presence of various induced absorption bands is thus evidenced. A main broad band is clearly visible at about 3.3 eV accompanied by a weaker structure at about 2.3 eV, appearing as a shoulder on the main absorption peak; the two components display 0.6 and 1.4 eV FWHM, respectively. The latter feature is less pronounced in the melted sample with respect to the preform. This effect can be a consequence of the rearrangement of the matrix during the drawing process, which the melted sample results from, leading to the removal of some defects. The low energy band and the tail of the main induced absorption band, extending in the visible region, are responsible for the color appearing in the core of the sample after a high delivered dose, as shown in Figure 4.2(b). Considering that coloration mostly occurs in the Pr-doped region of the sample it can be suggested that defects responsible for the formation of induced absorption are likely related to the RE presence.
At energies higher than 4.0 eV, the spectral shape suggests the presence of additional unresolved features. This high energy part was taken into account by adding a third very broad component to the fit, which permits a satisfactory qualitative reconstruction of the experimental data. We recognize that, while the two lower energy bands are well defined, the parameters of the third one have poor physical meaning, because in this energy region possibly even more than one band as well as scattering contributions can be present.

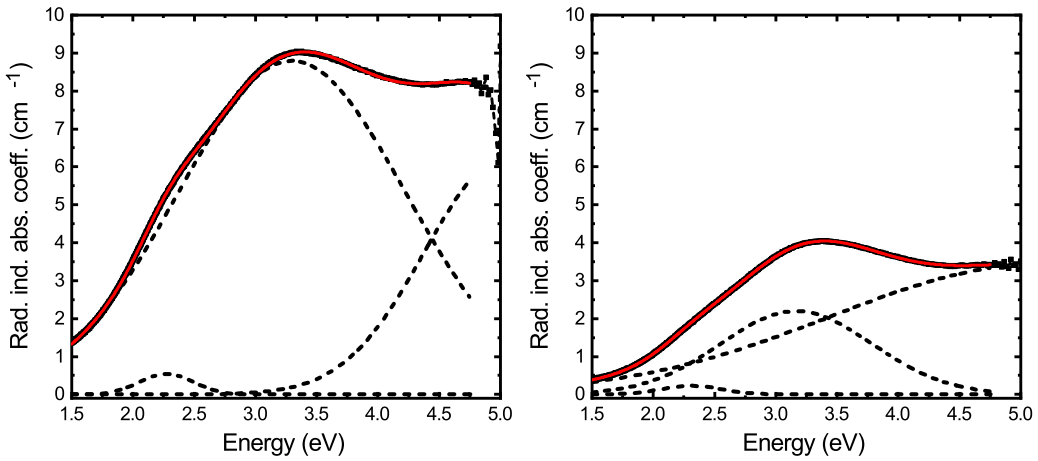

Figure 4.5: Numerical fit (red solid line) of the radiation-induced optical absorption spectrum of SiO_2:Pr preform (left) and melted sample (right) after 1 kGy irradiation, carried out as a sum of three Gaussian components (black dashed lines).

The evolution of the optical absorption spectra as a function of dose, RT recovery time and annealing temperature is reported in Figure 4.6. Each data point corresponds to the amplitude of the related Gaussian component. Only the two main bands have been considered for this analysis, because the third one was recognized to have a poor physical meaning.

A monotonic increase of both bands as a function of dose is evidenced, with a tendency to saturation that is more pronounced for the 2.3 eV band, as shown in panel (a) of Figure 4.6. This behavior can be explained as follows. The optical absorption depends on the number of defects populated after a given delivered dose: an easy way [88] to estimate the number of filled traps assumes the filling rate to be directly proportional to the dose D and to the vacancies in the centers. If the total number of trapping sites is N, out of which n are already filled up at any time, the incremental filling dn by a small incremental dose dD may be given by

$$dn = \alpha(N - n)dD \tag{4.1}$$

where α is the fraction of vacant traps which get filled up per unit dose. Using the initial conditions that $n = 0$ when $D = 0$, the solution of the previous equation is

$$n = N(1 - e^{-\alpha D}) \tag{4.2}$$

During irradiation, both trap filling (resulting in color centers production) and emptying mechanisms coexist, yielding to a dose rate dependent transmission loss. The induced absorption reaches a saturation value when the rate of defect filling becomes equal to their emptying one. This mechanism is particularly evident for shallow defects characterized by relatively short lifetimes.

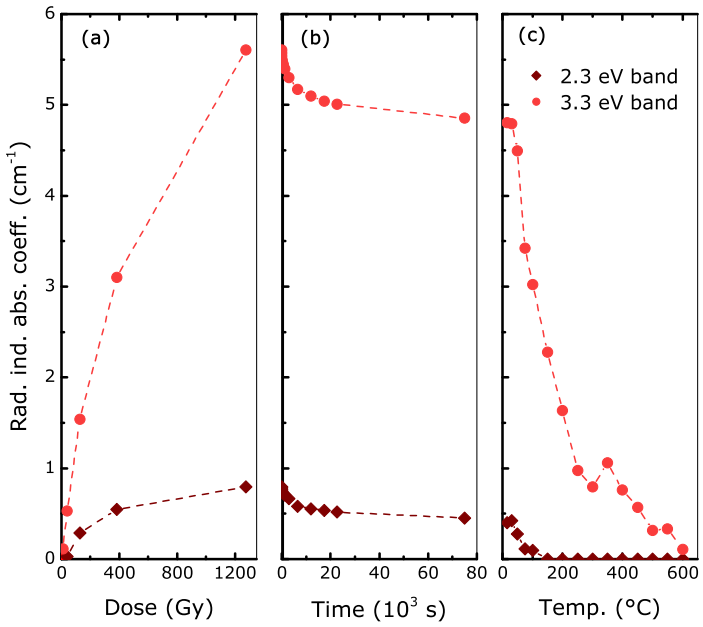

Figure 4.6: Radiation-induced absorption coefficient of SiO_2:Pr preform as a function of dose (a), RT recovery time (b), and annealing temperature (c). The behavior of the two main Gaussian components is reported. The ordinate scales are the same in the three panels. Dashed lines are guides for the eyes.

The induced defects responsible for the 2.3 and 3.3 eV bands are unstable and exhibit partial recovery at room temperature after irradiation. This spontaneous RT recovery is an important feature for a good scintillator because it reduces the radiation damage effect without requiring any treatment on the material, like thermal annealing or optical bleaching. This recovery can be caused by the spontaneous thermal escape of the carriers trapped at the absorbing center, or by their recombination with carriers of opposite sign freed from other unstable defects.

The spontaneous recovery at room temperature is well understood and explained [89, 90], and a phenomenological model to describe the observed effect has been proposed [91].

The evolution of the OA spectra as a function of recovery time has been investigated for a total time of about 20 h. The intensity of the induced absorption decreased monotonically; the transmission recovery turned out to be about 15 % for the main band peaking at 3.3 eV and much faster (about 45 %) for the lower energy component, as shown in panel (b) of Figure 4.6.

As the last step, the glasses were treated with thermal annealing cycles up to 800 °C, to check the thermal release of charges from deeper traps responsible for color centers and the possibility of a complete recovery of the radiation damage. The samples were heated up, in steps of 50 °C, by holding them in a preheated oven for 15 min at each temperature step. By this procedure also carriers in deep traps were released and a complete recovery was obtained after heat treatment at around 200 °C and at 600 °C for the 2.3 eV and for the 3.3 eV bands, respectively.

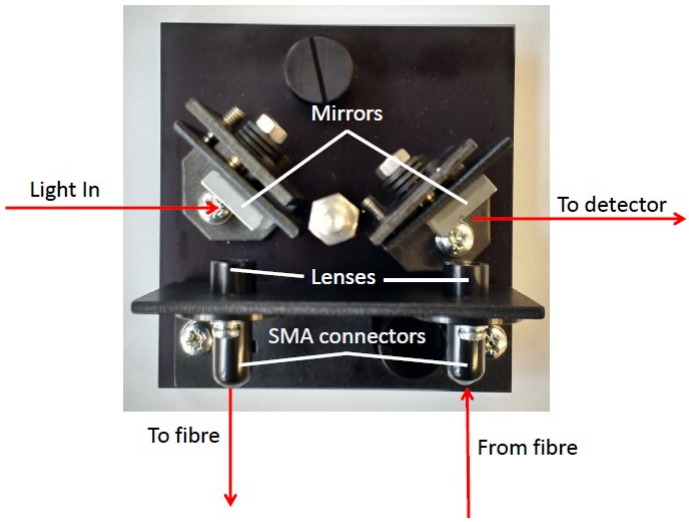

Figure 4.7: Top view of the Perkin Elmer Lambda 950 accessory for optical fiber measurements without the external cover. Red arrows show the optical path of the incident beam light.

From the results reported in this Section, it is evident that Pr-doped sol-gel silica is much affected by the formation of defects upon irradiation exposure: the poor radiation hardness can be considered the main drawback for the use of this material in applications involving high levels of ionizing radiation.
Therefore, new possibilities have been explored by considering Ce as luminescent activator is sol-gel silica host.

4.2 Radiation hardness of Ce-doped silica

Sol-gel silica fibers with Ce concentrations of 0.0125 mol.% and 0.05 mol.% have been characterized by means of optical absorption spectroscopy and attenuation length measurements before and after irradiation. The two different techniques gave comparable results, as illustrated in the following, and evidenced the formation of a main broad absorption band related to radiation-induced defects acting as color centers. The results were compared with those obtained on parent bulk silica.

4.2.1 Optical absorption spectroscopy on fibers and bulk silica

Optical absorption spectra of fiber samples were acquired using a Perkin Elmer Lambda 950 UV/VIS double beam spectrometer featuring a Transfer-Optic (B0509546) accessory for fiber measurements, which injects and collects light into and from suitably designed optical fibers. The spectrometer is able to cover the entire UV-VIS-NIR range, with a maximum photometric range of 6 absorbances.

The accessory for fiber measurements, shown in Figure 4.7, is composed of two curved mirrors and two lenses to focus the beam on the fiber core and match the fiber numerical aperture with that of the instrument: according to the producer, the accessory should have a throughput in the range of 10 to 20 % when using fibers with 600 μm core diameter.

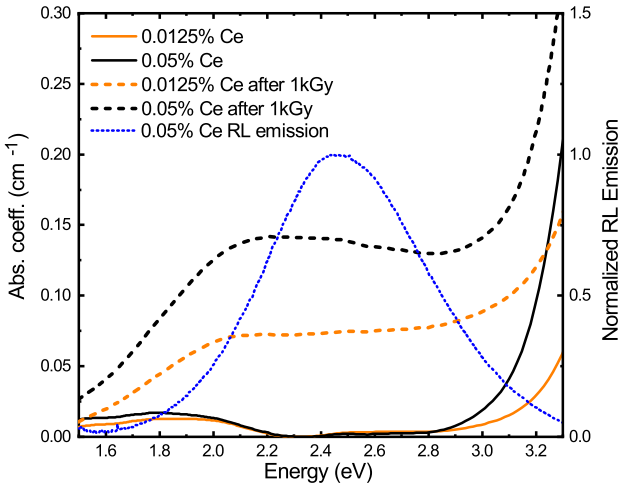

Figure 4.8: Optical absorption spectra of SiO_2:0.0125 % Ce- and SiO_2:0.05 % Ce-doped fibers before (solid lines) and after (dashed lines) 1 kGy γ irradiation. Dotted line: RL emission spectrum of Ce-doped silica fibers.

In order to reliably couple the accessory with the fibers to be tested, two *launch* fibers have been prepared, drawn by Polymicro Technologies: they are characterized by numerical aperture 0.22 and 600 μm core diameter, and are equipped with a SubMiniature A (SMA) connector on the side to be connected to the adapter, and a ferrule connector (FC) on the other. The choice of FC connectors to join the *launch* and the to-be-measured fiber should guarantee a reliable and repeatable alignment. The fibers were enclosed in a black heat-shrinkable case to eliminate possible cladding modes.

In Figure 4.8, the OA spectra of SiO_2:0.0125 % Ce- and SiO_2:0.05 % Ce-doped fibers before and after 1 kGy γ irradiation are displayed. The irradiation of the SiO_2:0.0125 % Ce-doped fibers was carried out at the Faculty of Nuclear Sciences and Physical Engineering (Prague, Czech Republic) with a dose rate of approximately 40 Gy/h; the irradiation of the SiO_2:0.05 % Ce-doped fibers was performed at the IONISOS facility (Dagneux, France) with a dose rate of 1 kGy/h. In both cases, a ^{60}Co source was used and the total cumulated dose was 1 kGy.
A ^{60}Co radioactive source emits 2 γs, of energy 1.33 MeV and 1.17 MeV, per disintegration: they are assumed to be uncorrelated in space and their difference in time is so small that they can be viewed in coincidence. Their angular correlation is indeed very weak, and an average energy of 1.25 MeV can be considered. The geometry of the irradiation facilities allows to obtain a uniform dose rate along the longitudinal axis of the fibers.

The RL spectrum of Ce-doped silica fibers is reported in Figure 4.8 as well, to better understand the possibility of self-absorption by the radiation-induced color centers. It consists in a broad band peaking at 2.45 eV, independently on the Ce concentration, whereas the absolute RL intensity was found to be proportional to the Ce content. RL spectra were acquired with the setup described in the previous section.

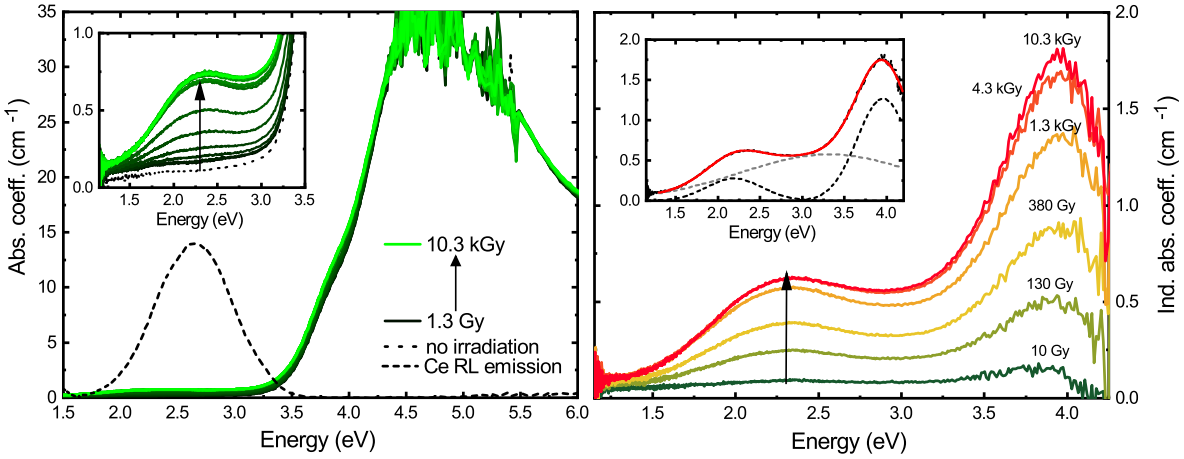

Figure 4.9: Left panel: optical absorption spectra of SiO_2:0.05 % Ce glass sample as a function of increasing dose. In the inset, an enlargement of the 1.0 - 3.5 eV region is displayed. The arrows indicates increasing dose. Dashed line: RL emission spectrum. Right panel: radiation-induced absorption spectra of SiO_2:0.05 % Ce glass sample. In the inset, numerical fit (red solid line) of the radiation-induced absorption spectrum after 10.3 kGy carried out as a sum of three Gaussian components (black and gray dashed lines) is shown.

OA measurements were limited to 3.3 eV because the interesting region for Ce^{3+} luminescence is in the visible range. Moreover, at higher energies, the measurements have poor reliability because of absorbance saturation and distortions related to luminescence contributions. The spectra are characterized by an evident absorption just above 3.1 eV, which is likely related to charge transfer of Ce^{4+} as well as Ce^{3+} $4f-5d$ transition [59] as already discussed in Section 2.4.1. Moreover, a broad and weak absorption structure is visible in the non-irradiated samples below 2.2 eV: this broad band could be ascribed to intrinsic defects [19, 39].

The irradiated samples show an evident increase of the absorption coefficient in the 1.5 - 3.0 eV energy range, due to the formation of a very broad radiation-induced absorption structure: the maximum absorption coefficient evaluated at 2.2 eV is 0.07 cm^{-1} and 0.14 cm^{-1} for the SiO_2:0.0125 % Ce- and SiO_2:0.05 % Ce-doped fibers respectively.
This new absorption contribution is superimposed to the RL emission of Ce^{3+}, leading to a reduction of the transmitted scintillation light.

The radiation-induced absorption coefficient is clearly lower for the less concentrated Ce-doped fiber: this points to a dominant role of the Ce content in the way doped silica is affected by irradiation.

For a deeper understanding of the transmission losses as a consequence of exposure to ionizing radiation, the OA spectra of the Ce-doped melted sample were studied as a function of irradiation dose, using a Varian Cary 50 Spectrophotometer. For practical aspects, X-ray irradiation was employed for these measurements, performed by a Machlett OEG50 X-ray tube with tungsten anode, operated at 32 kV.

In Figure 4.9, both absorption spectra (left) and radiation-induced absorption spectra (right) are reported. A monotonic increase of absorption as a function of dose is observed, also evident in panel (a) of Figure 4.10.

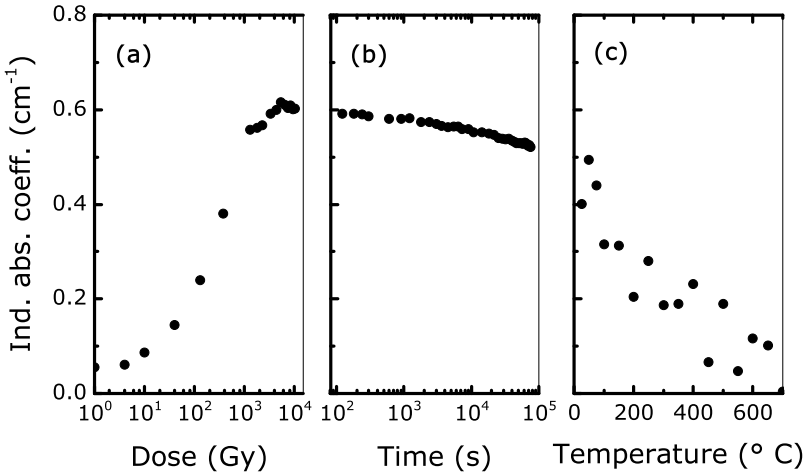

Figure 4.10: Radiation-induced absorption coefficient at 2.2 eV of SiO_2:0.05 % Ce-doped melted sample as a function of (a) dose, (b) RT recovery time, and (c) annealing temperature. The ordinate scales are the same in the three panels.

The inset of the right panel of Figure 4.9 shows the numerical fit carried out on the OA spectrum obtained after 10.3 kGy irradiation. It can be analyzed as a sum of three Gaussian components, peaking at 2.2 eV, 3.3 eV, and 3.9 eV with FWHM 0.8 eV, 2.5 eV, and 0.7 eV, respectively; the very broad width of the bands points towards the presence of contributions from defect distributions. The two lower energy bands overlap with the emission spectrum of Ce-doped silica and thus can cause re-absorption of the emitted light, leading to degradation of the optical transparency.

The samples studied in this work have been densified in oxidizing atmosphere: Ce is thus present mainly in its 4+ oxidation state, as suggested by the shape of the OA spectra of Figure 4.9 (left panel), dominated by the charge transfer band of Ce^{4+}. The correlation between the sintering atmosphere and the valence state of the incorporated Ce ions has been demonstrated in [59], and discussed in Figure 2.7. Moreover, the radiation-induced absorption band peaking at 3.9 eV might be related to the formation of additional Ce^{4+} ions, originating by the ionization of Ce^{3+} centers. A role of Ce^{4+}/Ce^{3+} balance in the response of silica glass to UV light exposure has been proposed in [92], and related to the difference in the environment surrounding ions with different valence state. It may be further disclosed in the case of ionizing radiation by studying and comparing the evolution of the OA spectra of silica samples sintered in reducing atmosphere.

In Figure 4.11, pictures of a Ce-doped fiber and the parent melted glass sample before and after irradiation are shown. After the exposure to ionizing radiation, Ce-doped silica displays coloration mostly in the doped core, where the luminescent activator is present. This observation corroborates the idea, introduced with the study of Pr-doped silica, that defects acting as color centers and responsible for the formation of the radiation-induced absorption bands in the visible range are likely related to the RE presence.

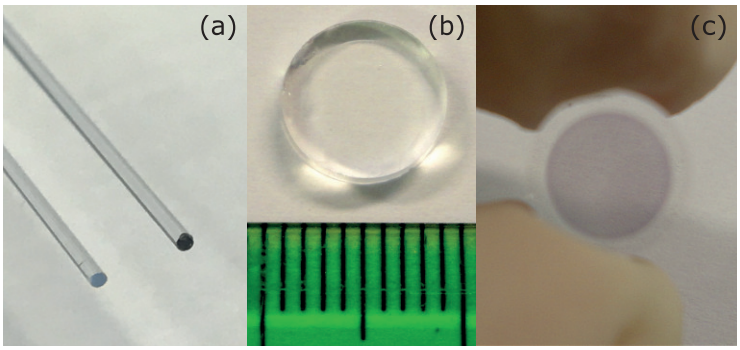

Figure 4.11: Pictures of 0.05 % Ce-doped optical fibers (a) before (on the left) and after (on the right) 1 kGy irradiation. Panels (b) and (c) display the parent silica bulk glass before and after irradiation, respectively.

The OA spectra of the Ce-doped melted sample and fibers show a similar absorption shape, suggesting that the drawing process does not modify the nature of the centers responsible for the radiation-induced absorption. On the other hand, it is interesting to evidence that the maximum absorption coefficient in the visible region is higher by about a factor 4 in the 0.05 % Ce-doped melted sample with respect to the corresponding fiber. This result confirms the positive influence of the fiber drawing process on the reduction of the concentration of defects created by the exposure to ionizing radiation: this effect can be related to a rearrangement of the silica network occurring during the high temperature process.

The evolution of the absorption coefficient evaluated at 2.2 eV as a function of dose, RT recovery time and annealing temperature is reported in Figure 4.10. As already noticed, the induced absorption increases monotonically with increasing dose, reaching a saturation level after about 5 kGy.

The behavior of the absorption coefficient as a function of recovery time was monitored for a total time of about 20 h. The absorption decrease turned out to be about 10 %, as shown in panel (b) of Figure 4.10.

Since only a partial recovery could be achieved at RT, the thermally activated recovery was also investigated by performing annealing cycles up to 700 °C: the glass sample was heated up in steps of 50 °C by holding it in a preheated oven for 15 min at each temperature step.
A complete recovery of the radiation damage was observed at 700 °C, which corresponds to the thermal activation energy of the color centers: at this temperature all carriers are freed and the glass became transparent again.

4.2.2 Attenuation length of light propagation

The results obtained by optical absorption spectroscopy are supported by the evaluation of the attenuation length of PL emission of Ce-doped fibers. For a fiber geometry, the propagation of the light is an important parameter to insure a good collection efficiency. To this aim, the attenuation length can be considered as the main practical parameter to characterize fibers, due to their small cross-section and high aspect ratio. Indeed, the importance of lateral surface state becomes crucial for an optimal propagation of the emitted light along the fiber itself.

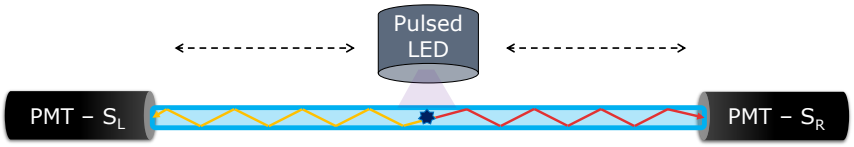

Figure 4.12: Sketch of the setup for the attenuation length measurement based on a double-side readout: the pulsed LED light source at about 1 cm distance is moved along the longitudinal axis of the fiber.

The attenuation length measurements were performed with a homemade setup, by illuminating the fiber with a 370 nm pulsed LED moving at constant speed (2.6 cm/s) along its longitudinal axis, as shown in Figure 4.12, and monitoring the luminescence output through dry coupling both fiber extremities to two Hamamatsu H6610 PMTs working at 2.3 kV. Long-pass filters (ThorLabs FGL420) were used to avoid parasitic excitation light. The LED was coupled through an optical fiber to a collimator, providing a beam size of about 2-3 mm. The double-side readout of the light allows to correct the measurement in case of small variations of the LED intensity and to compensate for fluctuations along the fiber, improving the reliability of the attenuation measurement and simplifying the readout procedure, as discussed in [11].

The results are shown in Figure 4.13. Assuming the defects to be homogeneously distributed along the fiber axis, the attenuation length profiles can be modeled as a single exponential decay according to Eq. 4.3, where S_{right} and S_{left} are the signal intensities recorded by the two photodetectors, x is the position along the fiber, and l_{att} is the attenuation length of the fiber, defined as the distance at which the incident beam is reduced of a factor $1/e$.
Eq. 4.3 can be derived by expressing the signal of each channel (S_{right} and S_{left}) as a single exponential decay $S_{left,right} = A_0 \ \exp\left(-\frac{L_0/2 \pm x}{l_{att}}\right)$, where L_0 is the total length of the fiber. Eq. 4.3 is thus obtained by computing the ratio of the two single channel signals.

$$\frac{S_{right}}{S_{left}} = A_0 \ \exp\left(\frac{-2x}{l_{att}}\right) \tag{4.3}$$

In practice, the reciprocal of the attenuation length has a physical meaning similar to that of the absorption coefficient for spectrally unresolved measurements.

Panel (a) of Figure 4.13 displays the attenuation length curves for SiO_2:0.0125 % Ce- and SiO_2:0.05 % Ce-doped fibers: the attenuation length value was estimated to be around 80 cm and 45 cm before irradiation and around 10 cm and 5 cm after irradiation, respectively (first data point of panel (b) of Figure 4.13). Following several repetitions of the experiment, a statistical uncertainty of 25 % has been associated to the attenuation length values.

The attenuation length trend as a function of dose is reported in panel (b) of Figure 4.13: in this case, a γ irradiation up to 22 Gy was performed at a CERN irradiation facility with a ^{60}Co source at a low dose rate of about 1 Gy/day. The shaded region of the figure shows the attenuation length values after 1 kGy irradiation, performed as described in the previous section.

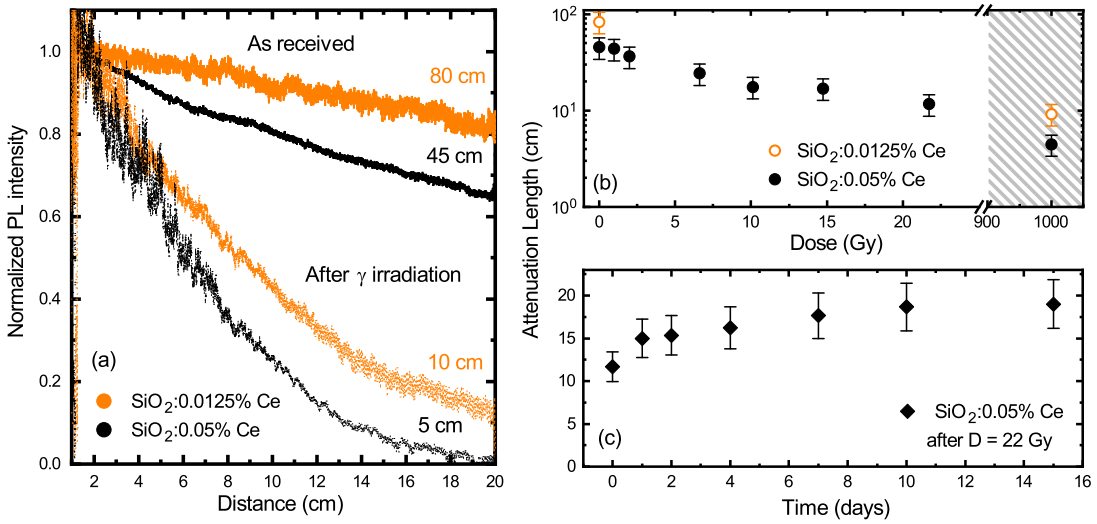

Figure 4.13: (a) Attenuation length curves for SiO_2:0.0125 % Ce- and SiO_2:0.05 % Ce-doped fibers before (solid lines) and after (dotted lines) 1 kGy γ irradiation. Right panels: attenuation length values as a function of dose (b) and of RT recovery time after 22 Gy irradiation (c).

Panel (c) of Figure 4.13 reports the attenuation length as a function of RT recovery time after 22 Gy irradiation: a recovery of about 22 % followed over 15 days can be observed. After 1 day, the recovery was estimated to be around 10 %, thus being comparable to what obtained for the melted sample, monitored by OA spectroscopy, as shown in Figure 4.10.

It is important to underline that the attenuation length results are in good agreement with OA measurements: attenuation length values after irradiation (10 cm and 5 cm) are in fact rather consistent with the absorption coefficient in the maximum of the visible region (0.07 and 0.14 cm^{-1}). The two methods allow thus a direct comparison of the response of the investigated materials in fiber shape, although with slight differences in their working principle.

Attenuation length measurements permit to detect the light emitted directly by luminescent centers, reproducing conditions more similar to those found during the effective operation of HEP detectors. However, the evaluation of the attenuation does not consider variations in the emitted light spectral shape, but only a uniform reduction of the luminescence intensity. On the other hand, in the OA measurements, the light injected in a fiber from one end is detected at the opposite side and no emission phenomena are aimed to be considered: this procedure give hints on intrinsic absorption of the bulk, presence of cracks and defects, self-absorption, and quality of the polishing. The introduction of an incident angle takes into account a larger amount of light paths and assesses the quality of the light guiding, although the propagation angle inside a fiber is rather small.

An effect of Ce concentration on the radiation hardness of silica fibers has been confirmed by both the measurement techniques: by comparing OA spectra and attenuation length curves before and after 1 kGy γ irradiation, it can be observed that an improvement of the radiation resistance of the material is achieved by a reduction of the Ce content inside the fiber core.

Moreover, also the intrinsic attenuation length could reach higher values by decreasing Ce concentration. Therefore, a good compromise between a longer attenuation but a lower emission intensity, both following the reduction of the dopant content, has to be found for future optimization of sol-gel silica fibers.

4.3 Conclusions

Optical absorption measurements after exposure to ionizing radiation reveal a high level of radiation damage of Pr-doped sol-gel silica, which affects the light transmission inside the doped glasses, because of a strong self-absorption starting even at a relatively low dose.

On the other hand, as the result of irradiation tests on Ce-doped sol-gel silica using X- and γ-rays up to 10 kGy, the formation of induced absorption bands could be observed, but with a lower value of the absorption coefficient than for Pr-doped silica. Therefore, the use of Ce as luminescent activator turned out to be a good solution for the improvement of the radiation resistance of sol-gel silica. Moreover, Pr-doped silica showed a slower recovery of about a factor 2, although after a thermal annealing up to 600 °C a complete recovery of the radiation damage was obtained for all the samples.

The most relevant result in the improvement of the radiation hardness can be considered the observation of a reduction of the concentration of the optically active defects acting as color centers under irradiation, obtained after fiber drawing both in Pr- and Ce-doped silica. A link between this phenomenon and a structural readjustment of the Si-O amorphous network, better incorporating the RE ions, and of the traps distribution, induced by the high temperature treatment associated with the fiber drawing process, can be established.

Moreover, both through a spectroscopic and a practical approach, it has been shown that also a reduction of Ce content inside the silica fiber core leads to an improvement of the radiation hardness, suggesting that radiation-induced defects are related to the presence of the dopant. The measurement of the attenuation length revealed to be an efficient and practical technique for the evaluation of the evolution of the luminescence performance of fiber-shaped materials after radiation exposure.

The results presented in this work help to increase the fundamental comprehension of the incorporation of RE ions in the SiO_2 matrix synthesized by sol-gel route and could stimulate the improvement of synthesis techniques aimed at the control of the material defectiveness. Finally they can guide the future engineering of scintillating silica fibers, which will take into account the possibility to reach a satisfactory optimization of both emission intensity and radiation hardness.

Since the most promising results were obtained for Ce-doped silica fibers, they were chosen as the active scintillating material to be embedded in a small calorimeter prototype, tested during a test beam campaign with high energy electrons in June 2017. The experiment and its outcome are described in Chapter 6.

Chapter 5

Trap distributions and slow scintillation tails in silica fibers

A fast and efficient energy transfer from the host matrix to the emission centers is of great importance to achieve scintillating materials with high efficiency and fast scintillation response. As introduced in Chapter 1.2, a fundamental stage in the scintillation process is the transport to the luminescent centers of carriers generated by ionizing radiation; the efficiency and speed of carrier transfer through the host lattice are often largely affected by the presence of trapping levels in the forbidden gap of the material, which can temporarily capture migrating charge carriers and thus delay their radiative recombination at emission centers, according to the lifetime of the traps involved.

Point defects acting as traps for free carriers created during irradiation are detrimental for the performances of scintillators. Shallow traps, with lifetime in the μs - ms time scale, are responsible for slow tails in the scintillation decay. Deep traps, stable at room temperature, can store the carriers for very long time and lower the overall scintillation efficiency by competing with luminescent centers in charge capture. On the other hand, applications other than scintillators, like dosimetry, exploit deep stable traps, whereas traps with lifetimes of several hours are looked for in persistent luminescent phosphors. The terms *shallow* and *deep* are not uniquely defined, because the same trap in a material can be considered shallow or deep depending on the time scale of optical transitions: a sketch of the two types of traps is displayed in Figure 5.1.

The investigation of trapping processes is an important aspect both for the fundamental comprehension of the material properties and for its application-oriented engineering.
In Chapter 4, the effect of induced defects on the loss of transparency of RE-doped silica glasses has already been reported.

Several different techniques exist for the investigation of the influence of defects on the scintillation properties of a material and in this work they have been employed in correlated experiments: among them, time decay measurements at varying temperature and excitation

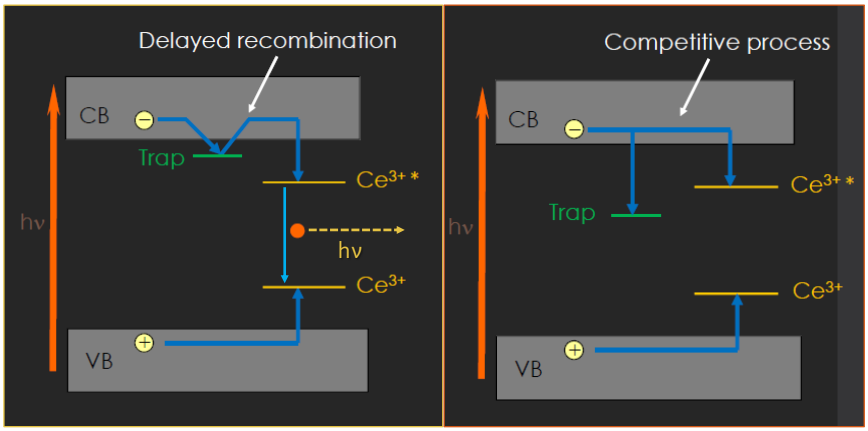

Figure 5.1: Simple scheme of the role of traps in affecting the recombination at luminescent centers (Ce^{3+} in this example). On the left, shallow traps introduce a delay in the recombination process according to their lifetime; on the right, the permanent capture of charge carriers by deep traps can be considered as a competitive process with respect to radiative recombination.

energy, wavelength-resolved thermally stimulated luminescence, phosphorescence, and temperature evolution of radio-luminescence efficiency. Experimental investigations of traps are aimed at finding their characteristic parameters, like the thermal depth, the frequency factor, and the order of kinetics, later discussed in this chapter, that enable to predict their lifetime at a given temperature and, consequently, their expected influence on the scintillation properties.

In this work, the presence of a distribution of trap levels and its correlation with the observation of slow tails in the μs time range in the scintillation decay are discussed, in order to deepen the knowledge of the mechanisms governing the recombination and the scintillation emission in RE-doped sol-gel silica glass. Ce-doped silica fibers, already presented in Section 3.1, have been chosen as the illustrative material for this study.

5.1 Role of defects in scintillation

The recombination between carriers freed from traps and luminescent centers often include carrier transitions into the conduction or valence bands, before the recombination occurs (Section 5.1.1). However, sometimes the recombination process does not involve the delocalized bands, but it concerns only the levels of the trap and of the recombination center: this phenomenon is indicated as *localized transition* or *tunneling recombination* (athermal or thermally assisted). In particular, the latter definition is used when the trap and the luminescent center are closely lying but distinct defects, with states located at similar energy levels in the band gap [93]. In Figure 5.2, the possible ways of detrapping and consequent recombination are sketched.

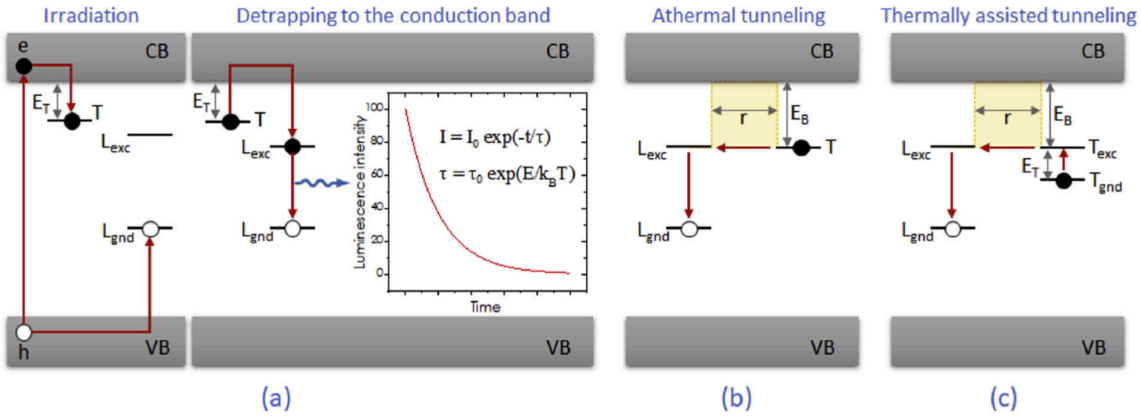

Figure 5.2: Scheme of electron trapping during irradiation followed by detrapping and luminescent emission. (a) Detrapping involving the delocalized bands; (b) athermal tunneling between trap and recombination center; (c) thermally assisted tunneling between trap and recombination center. Picture taken from [93].

5.1.1 Thermal detrapping through delocalized bands

A model that takes into account only the case in which the time spent by electrons in the excited state of the luminescent center is much shorter than the lifetime of the electron traps involved in the trapping process is considered. The probability P_T of an electron being thermally released from its trap is exponentially related via Eq. 5.1 to the *trap depth* (E_T), which is the energy difference between the trap and the edge of the corresponding delocalized band:

$$P_T = \nu \ \exp\left(-\frac{E_T}{k_b T}\right) = \frac{1}{\tau_T} \tag{5.1}$$

ν is the frequency factor of the trap, k_b the Boltzmann constant, and τ_T the decay time of the trap. Carrier retrapping is neglected in this description, which means that a first order recombination process, displayed in Figure 5.2(a), is considered. The process is depicted involving electron traps, but the opposite process can also be considered (i.e. hole trapping).

Once the electrons become trapped at a level T, recombination can only take place if the trapped electrons absorb enough thermal energy E_T to be released back to the conduction band, from where the recombination is possible. Thus the luminescent emission is delayed by an amount governed by the mean time τ_T spent by the electrons in the trap [35].
If the trap depth is such that, at the temperature of irradiation T_0, $E \gg k_b T_0$, any electron which becomes trapped will remain so for a long period of time, so that after removal of the irradiation, there will exist a substantial population of trapped electrons. The return to equilibrium can be speeded up by raising the temperature above T_0 such that $E \leq k_b T$, which in turn will increase the probability of detrapping P_T.

Considering the subsequent capture of electrons by the excited states of the luminescent centers, followed by their prompt radiative decay, the emitted light intensity as a function of time is proportional to the rate of recombination of electrons freed from traps, following the formula:

$$I(t) \propto \frac{dN_e}{dt} \propto \frac{dN_T}{dt} \propto N_0 \exp(-P_T t) = I_0 \exp\left(\frac{-t}{\tau}\right) \tag{5.2}$$

where N_e is the number of electrons in the excited state of the luminescent center, N_T is the number of trapped electrons, N_0 is the number of traps initially filled by irradiation, and I_0 represents the initial intensity.
This leads to the conclusion that the exponential decay of luminescence becomes faster by temperature increasing.
The proportionality relationship (instead of identity) in Eq. 5.2 between the decay rate of trapped electrons, the decay rate of electrons in the excited state of the luminescent center, and the luminescence intensity is due to (1) the possibility that after detrapping electrons do not undergo capture by the luminescence center, and (2) the possibility of an alternative non-radiative recombination path of the electrons from the excited state of the luminescent center to the ground state.
The possibility of retrapping can be included in the model, introducing kinetic recombination orders higher than 1: in this case, the decay is no longer a simple exponential, but an acceleration by temperature increasing is observed. Moreover, the recombination can occur at different luminescent centers, if present in the material, giving rise to a composite emission spectrum. Eq. 5.2 is no longer valid when very shallow traps are present whose lifetime is comparable or shorter than the radiative decay time of the luminescent center. To account also for these cases, more complicated equations were developed, that were able to explain not only scintillation decays, but also scintillation rise times [94].

5.1.2 Temperature independent recombination: athermal tunneling

Localized trap-center recombinations often manifest a phenomenology that involves the occurrence of a quantum tunneling effect. The experimental characteristics of athermal tunneling recombination, like the lack of retrapping and the presence of only one recombination center, are in principle compatible also with a thermally activated process in those cases in which the number of luminescent centers is much larger than the number of traps, and one recombination center is dominant, as it occurs when intentional doping with luminescent ions is performed.
The most important signature of the occurrence of an athermal tunneling recombination is the independence of both the phosphorescence signal and decay rate upon temperature. A simple sketch of this phenomenon is reported in Figure 5.2(b).

The temperature independent tunneling probability P_{AT} can be written as the product of two terms

$$P_{AT} = C\ W(r) \tag{5.3}$$

where C has the dimensions of the inverse of time and $W(r)$ is the tunneling probability; for a rectangular barrier with height E_B, it is defined as

$$W(r) = \exp\left(\frac{-4\pi}{h}(2mE)^{1/2}r\right) \tag{5.4}$$

where r corresponds to the trap-center distance, m is the electron mass, and h is the Planck's constant.

The luminescence decay is therefore exponential and strongly dependent upon the barrier configuration.

$$I(t) \propto \frac{dN_T}{dt} = I_0 \exp\left(-\frac{t}{\tau}\right) = I_0 \exp(-CWt) \tag{5.5}$$

Usually, such single exponential behavior is hardly observed, because in a solid there are several trap-center distances due to the random distribution of traps. Therefore, the signal is the combination of all contributions from pairs at different distances. In this case, it can be demonstrated that, after an initial transient time, the decay follows a t^{-1} law [95, 96].

$$I(t) = \frac{I_0}{t - \delta} \tag{5.6}$$

Although there are no specific limitations for the trap-center separations involved, it is reasonable to assume that they are limited to a few interatomic distances: in fact, as the trap-center distance increases, the wave functions overlap soon becomes negligible. Since the trap-center distance is a crucial parameter in athermal tunneling, a dependence of the phenomenon on the concentration of traps and centers is expected.
Tunneling can hardly occur from traps to centers at large distance, without the participation of several traps providing a chain-like path toward the luminescent center that the charge can cover step by step with successive tunneling events. However, this is not likely to occur in the case of trapped carriers, unless the defects are in a very high concentration.

5.1.3 Distribution of trap levels

A power law decay similar to that of Eq. 5.6 is expected to occur also in the case of a continuous distribution of trap energy levels; in this case, it is accompanied by broad and structureless thermo-luminescence features. Distribution of trap levels usually occurs in amorphous materials, because of the presence of inhomogeneous broadening induced by disorder [97]. It is the case of Ce-doped silica fibers studied in this work, as it will be reported in the following.

For the case of traps uniformly distributed in energy, it was shown that the emitted light intensity is given by [98]

$$I = \int_0^\infty N_E s \exp\left(-\frac{E}{k_b T}\right) \exp\left[-st \exp\left(-\frac{E}{k_b T}\right)\right] dE \tag{5.7}$$

where N_E is the number of traps with depth between E and $E + dE$, and s is the frequency factor. Upon integration and assuming that $\exp(-st) \ll 1$, Eq. 5.7 becomes

$$I(t) = \frac{n_0 k_b T}{t + \delta} \tag{5.8}$$

n_0 being the initial population of the trap distribution, and δ a constant.
Other, more limited but more realistic, energy distributions like Gaussian ones give rise to similar t^{-1} time decays that indeed feature some temperature dependence at variance with

tunneling decays [97, 99]. Therefore, in principle it is possible to distinguish between the two mechanisms by looking at the presence of a temperature dependence of the decay curve intensities, which mostly occurs in the initial stage of the decay.
As it will be pointed out in the next sections, the presence a continuous distribution of defect levels or the occurrence of an athermal tunneling recombination process in Ce-doped silica fibers can be investigated in detail by coupling the analysis of the scintillation decay to the thermo-luminescence results.

To deeply disclose the role of defects in the scintillation mechanism of Ce-doped silica, several techniques have been employed, and the results discussed in the following.
In Section 5.2, the RL emission as a function of temperature in a wide temperature range (10 - 400 K) is investigated, and an intense RL signal is detected: a mechanism to explain the observed behavior of the RL efficiency upon increasing irradiation dose is also suggested. The intensity of the slow component of the scintillation decay has been monitored as a function of temperature in Section 5.3 and correlated with the continuous distribution of trap energy levels observed by thermo-luminescence in Section 5.5: a good accordance between the results obtained with the two different methods can be established. In Section 5.4, the isothermal phosphorescence signal detected after X-rays excitation is discussed and analyzed.

5.2 Radio-luminescence efficiency below and above RT

RL spectra of Ce-doped silica fibers as a function of temperature in the 10 - 320 K range under 20 kV X-rays excitation are shown in Figure 5.3: no shape modifications can be observed, and the spectrum features the $5d-4f$ emission band related to the radiative transition of Ce^{3+} ions peaking at around 460 nm.

In the inset, the temperature dependence of the integral of the RL emission band is reported: the complex shape can be ascribed to the progressive disappearance of competitive recombination channels and to the influence of traps. Indeed, during the RL process, besides a prompt recombination, free carriers experience trapping at defects sites, whose stability strongly depends upon temperature: this can be evidenced by following the RL temperature dependence of stable radiative centers, like RE ions, which do not undergo a marked proper intrinsic quenching below RT.

The results reported in the inset confirm the RL temperature dependence already observed in the literature for SiO_2:Ce [21]: furthermore, the effect of the history of the sample is here investigated. The sequence of RL spectra has been carried out both increasing (from 10 K to 320 K) and decreasing the temperature (from 320 K to 10 K): in this way, the influence of the trap filling on the Ce RL emission intensity can be disclosed. We expect that no trace of the previous irradiation should be seen when the measurements are performed by decreasing the temperature from 320 K to 10 K: in fact, the traps filled at each irradiation are not stable at the following temperature step. On the other hand, this is not the case when the temperature ramp goes upwards; however, only a slight decrease of the RL intensity was observed in the latter measurements, but no changes in the behavior, as demonstrated in the inset of Figure 5.3.

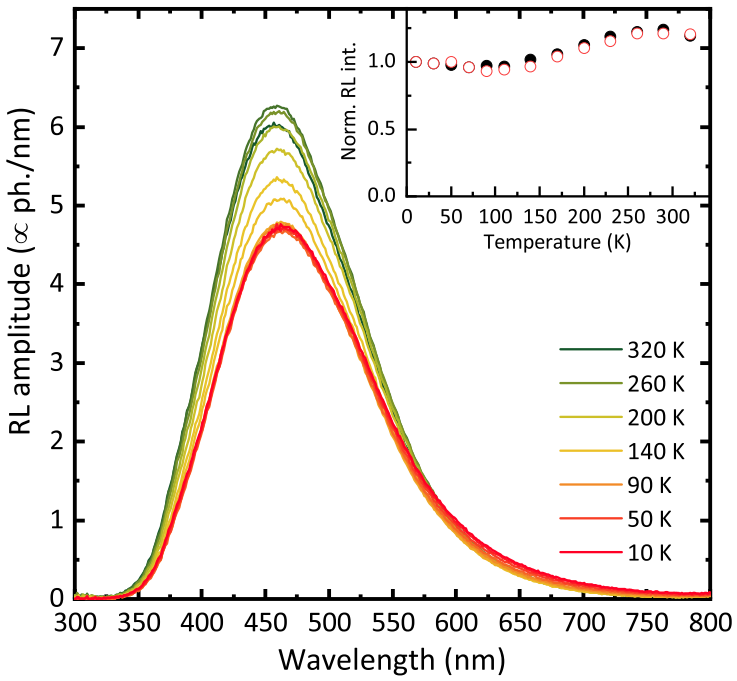

Figure 5.3: RL spectra under 20 kV X-ray excitation as a function of temperature. The inset shows the temperature dependence of the RL intensity, evaluated as the integral of the Ce emission in the 350 – 750 nm range. Full symbols: temperature sequence from 320 K to 10 K. Open symbols: temperature sequence from 10 K to 320 K.

We can conclude that the RL intensity below RT is not strongly affected by the presence of defects evidenced by TSL experiments reported in the Section 5.5.

The stability of the RL signal has been verified also above RT, in collaboration with the Lawrence Berkeley National Laboratory, where the measurements have been performed: the homemade setup is equipped with an X-ray tube with a rotating copper anode operated at 50 kV as excitation source and a CCD Pixis 100B (Princeton Instruments) coupled to a monochromator with a 300 grooves/mm grating as detection system. A temperature ramp rate of 1 K/s is provided by a Lakeshore 336 Temperature Controller coupled to a ARS2HW Compressor, using a close circuit and a water cooling system. At each temperature step, a stabilization time of 10 minutes was chosen to provide a good thermalization of the sample. RL spectra were acquired with a temperature step of 10 K from 400 to 290 K for Ce-doped silica fibers; a comparison with Pr-doped silica fibers has been carried out and reported in Figure 5.4. Each data point corresponds to the integral of the RL spectrum in the emission range, namely 365 - 700 nm and 240 - 415 nm for Ce and Pr-doped silica, respectively.

A quite good stability of the RL signal for Ce-doped fibers is observed in the temperature range explored, compared to a strong decrease of the RL intensity of Pr-doped fibers: in the former case, a signal loss of only 15 % occurs at the highest temperature reached. In the case of Pr doping, the loss of signal is almost 80 %, pointing towards a strong thermal quenching of the RL emission, due to the increased probability of non-radiative recombination channels at temperature well above RT.

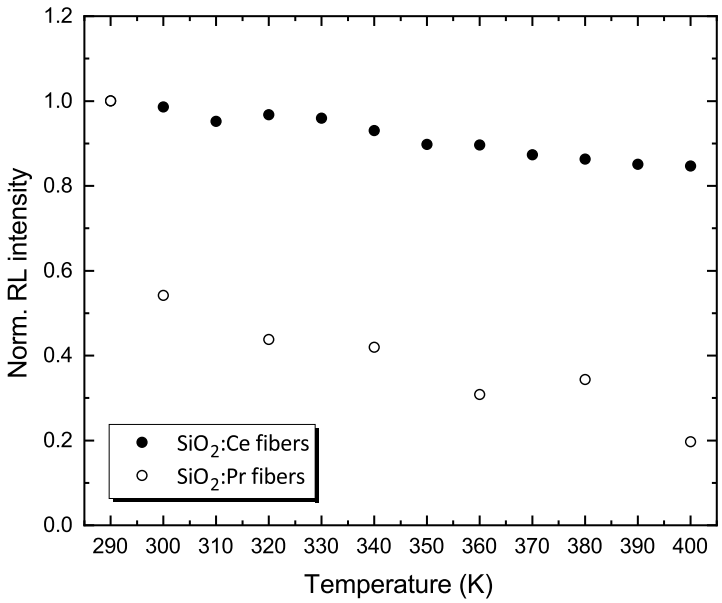

Figure 5.4: Temperature dependence of the RL intensity under 50 kV X-ray excitation above RT.

This experiment can be considered the first step to investigate the possible application of RE-doped silica fibers as scintillators in harsh environments involving high temperatures: indeed, a good stability of the luminescence signal is the main requirement for such application. Moreover, this experiment opens perspectives for Ce-doped silica fibers to achieve a complete recovery of the damage induced by irradiation, as explained in Section 4.2: by keeping the material at high temperature during its use as scintillator, it could be possible in principle to avoid the damage, inducing a simultaneous recovery. Further studies are planned in the future, to deeply investigate this application perspective.

5.2.1 Radio-luminescence sensitization in Ce-doped silica

In the field of scintillators, the increase of light yield due to a prolonged irradiation exposure is known as hysteresis or *bright burn* phenomenon. The microscopic origin of the bright burn was investigated in several materials, like CsI:Tl at first [100], then Al_2O_3:C [101], and recently silicates, such as LYSO:Ce [102] and LPS:Pr [103], perovskites [104], garnets [103], and Tb-doped SiO_2 [49].

The origin of this phenomenon has been ascribed to a progressive filling of deep traps, which causes their neutralization as competitors with the luminescent recombination centers in free carrier capture. It can have a temporary or permanent character, according to the temporal stability of the traps responsible for it. A temporary effect is produced by rather shallow traps, which are emptied in a relatively short time and give rise to an afterglow signal.

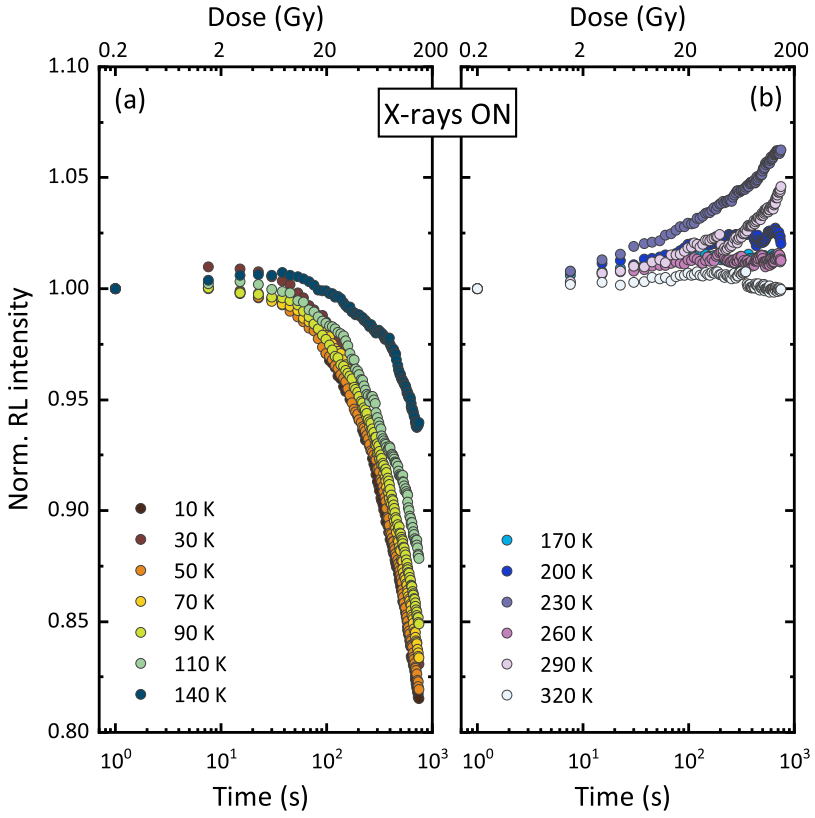

Figure 5.5: RL intensity as a function of time during X-ray irradiation at different temperatures. In panel (a), the 10 - 140 K temperature range is reported, in panel (b) the 170 - 320 K range. RL efficiency has been calculated as the integral of the emission band in the 350 - 700 nm range. The curves are normalized to their initial value.

However, if the traps involved are very deep and stable, no afterglow can be observed in a laboratory measurement time frame, but their filling gives rise to a permanent increase of the RL intensity, due to the progressive reduction of trapping probability for free carriers with respect to radiative recombination. In this case, the phenomenon produces a memory of previous irradiations, which remains stored in the material.
It has been demonstrated that the enhancement of RL intensity as a function of irradiation is a common characteristic of several scintillators, whose dose dependence and overall relevance are peculiar of each material and might reflect the different concentrations, stabilities, and capture cross-sections for carrier traps as well as their spatial correlation with the recombination centers.

Sequences of RL intensity measurements as a function of X-ray cumulated dose were performed on Ce-doped silica fibers by varying the temperature in the 10 - 320 K range. The results are displayed in Figure 5.5 as a function of time; the total dose is proportional to irradiation time at the fixed dose rate of $\sim$ 200 mGy/s. Data points represent the integral of the RL emission spectrum in the 350 - 700 nm range, corresponding to the Ce emission band. The measurements have been carried out using the apparatus for RL measurements previously described, with the X-ray tube operated at 20 kV; after each sequence, the fibers were heated to 320 K to empty all the filled traps and restore the pristine RL response.

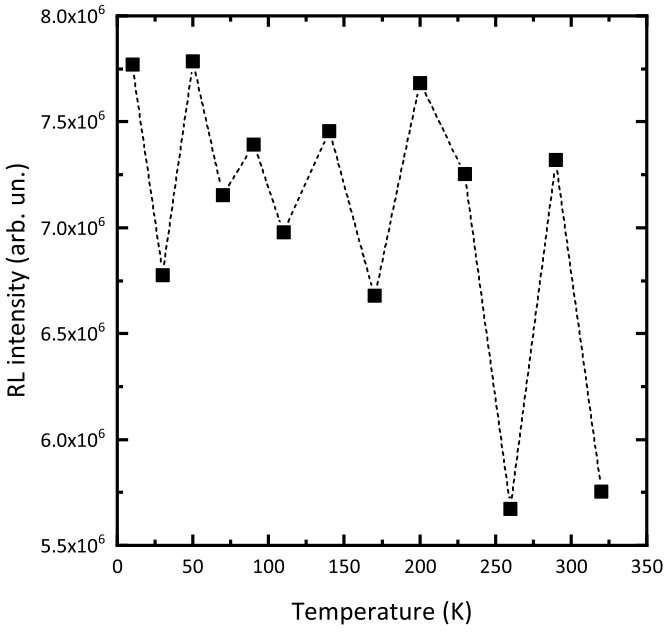

Figure 5.6: Initial value of the curves displayed in Figure 5.5 as a function of temperature. No normalization procedure has been performed. After each measurement, the silica fibers were heated up to 320 K in order to empty all the traps previously filled by irradiation: a great scattering of the experimental data can be observed. Dashed lines are guides for the eye.

The initial value of each curve displayed in Figure 5.5 is reported as a function of temperature in Figure 5.6: a great scattering of the data and no temperature dependence can be observed, thus confirming that all the traps are emptied when heating the sample up to 320 K before each RL intensity versus time sequence. Figure 5.6 should be compared to the inset of Figure 5.3: the only difference between the two is that in this latter case the fibers were heated up to 320 K after each RL measurements sequence, whereas in the former they were not heated. This observation points to a complex influence of the irradiation history on the RL intensity response, affecting the measurements reported in Figure 5.3, which needs further investigation.

It is interesting to notice that, for T $<$ 150 K (left panel of Figure 5.5), a decrease of the RL intensity upon cumulated dose is evident, and it reaches almost 20 % at the minimum temperature of 10 K.
On the other hand, for T $>$ 150 K (right panel of Figure 5.5), the bright burn phenomenon occurs and an increase of the RL intensity can be observed, more pronounced at 230 K: above this temperature, the RL signal becomes more stable and only a slight increase is visible.

The latter case is already well understood and ascribable to the competition between traps and recombination centers in capturing free carriers created upon irradiation: once a dynamical equilibrium is achieved, a saturation level is reached.
On the contrary, there are only few evidences in the literature of a decrease of the RL intensity with prolonged exposure to irradiation, occurring at low temperature [105].

The observed phenomenon can be explained by taking into account the formation of defects, induced also by a relatively low irradiation dose, which lead to self-absorption of the emitted light, but are unstable at higher temperatures, in this case above 150 K. This hypothesis can be further tested by measuring the temperature stability of radiation-induced absorption bands below RT, by means of OA spectroscopy at cryogenic temperatures.
Alternatively, defects in the proximity of Ce^{4+} ions could be created by irradiation, inducing a charge compensation which inhibits the $Ce^{4+} \rightarrow Ce^{3+*}$ transition.

Finally, an influence of the spatial correlation between traps and luminescent centers in the hysteresis phenomenon can be taken into account. In general, a close proximity between traps and centers is expected to enhance the bright burn effect because they directly compete in capturing the carriers during the very final stages of their path, when their energy is too small to produce additional lattice ionization and excitation. However, if the trap-center distance is really small (of the order of a few Angstroms) and if a correspondence between their energy levels exists, then the hysteresis phenomenon can be made less evident thanks to the occurrence of a direct tunneling recombination.
In the following sections, the presence of a tunneling process is further investigated by means of phosphorescence decay and thermo-luminescence measurements.

5.3 Scintillation decay as a function of temperature

Scintillation decay curves of Ce-doped silica fibers as a function of decreasing temperature from 350 K to 10 K are reported in Figure 5.7(a). Scintillation measurements have been performed at the Lawrence Berkeley National Laboratory using 40 keV X-rays as excitation source [106]. The scintillation profiles have been fitted in an operative way in order to identify the various components of the decay.

Two separated temperature regions have been distinguished in the following analysis.
For T $<$ 200 K, the best function reproducing the experimental data consists in a sum of two exponential contributions and a power law decay component:

$$I(t) = A_1 \, e^{-\frac{(t-t_0)}{\tau_1}} + A_2 \, e^{-\frac{(t-t_0)}{\tau_2}} + B(t-t_0)^{-p} \tag{5.9}$$

where p converges to about 0.85 and t_0 is negligible in the time window considered.
For T $>$ 200 K, the experimental data better follow a sum of three exponential contributions.

$$I(t) = \sum_{i=1}^{3} A_i e^{-\frac{t}{\tau_i}} \tag{5.10}$$

Decay time constants (τ_i) and relative weights (w_i) evaluated from the fit analyses are reported in panel (b) and (c) of Figure 5.7, respectively. For all temperatures, the decay is a three-stage process, characterized by an initial fast contribution with around 45 ns decay time and a leading component of about 125 ns; the third component is described as a power law decay below 200 K and as an exponential decay in the μs time range at higher temperatures.

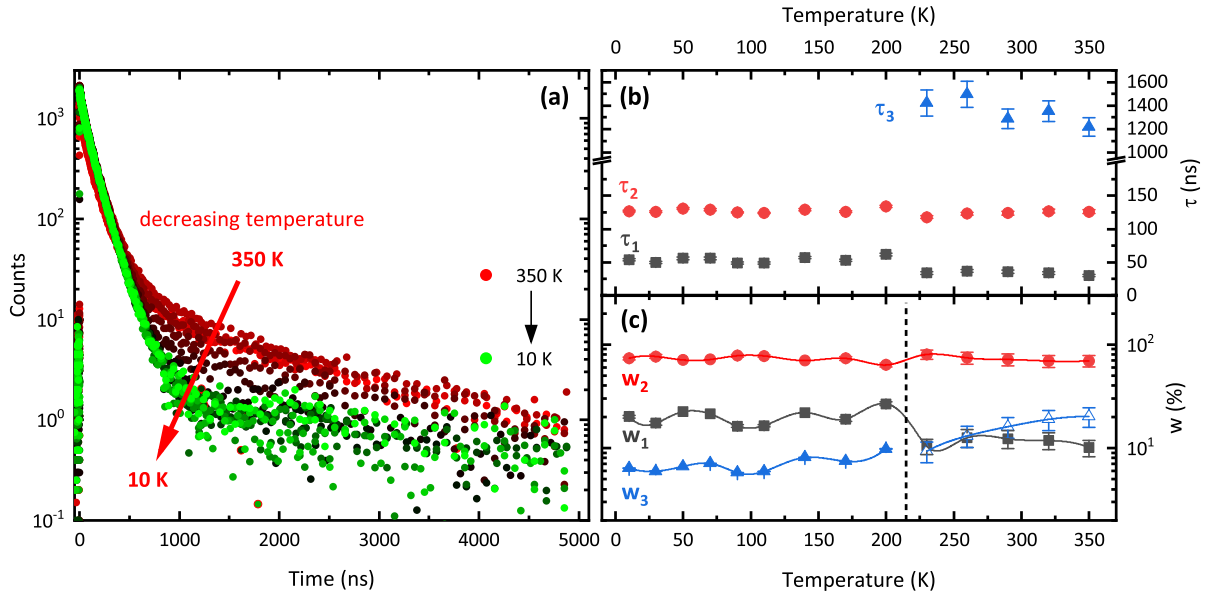

Figure 5.7: Spectrally unresolved scintillation decay profiles as a function of temperature (panel a), obtained by exciting with a pulsed X-rays source. A sum of three exponential contributions can be identified from 200 K to 350 K; below 200 K, a sum of two exponential components and a hyperbolic behavior can be observed. Temperature dependence of the time constants of the decay (panel b), and temperature dependence of the weights of the three components of the decay (panel c): error bars are within the size of data points and solid lines are guides for the eye.

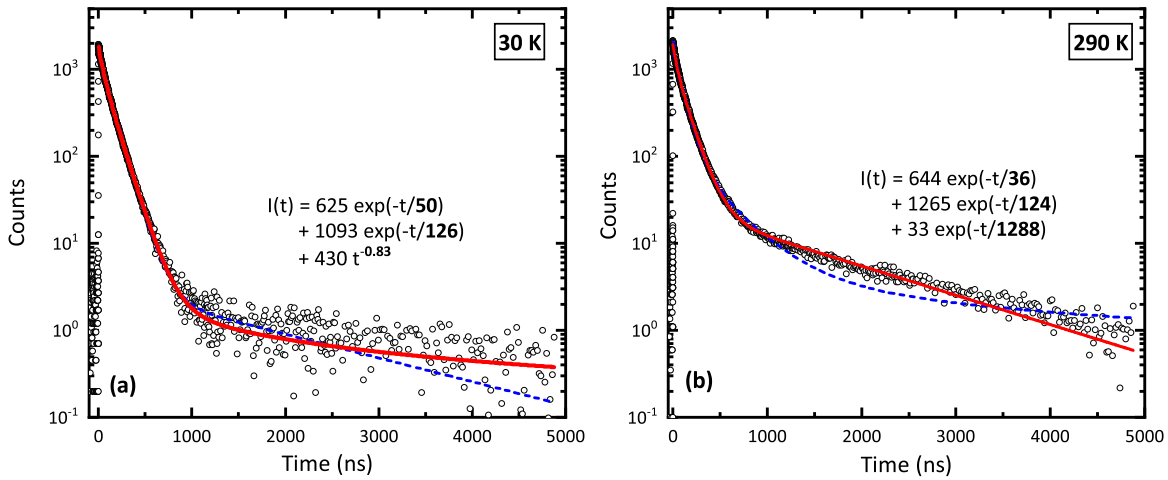

Figure 5.8: Examples of the fit to experimental data of the scintillation decay at 30 K (panel a, red solid line), by the sum of a two-exponential and a power law function (Eq. 5.9), and at 290 K (panel b, red solid line) using a sum of three exponential components (Eq. 5.10). Blue dashed lines show that a three-exponential model is not suitable to fit the scintillation decay curve at 30 K and that, on the other hand, a power law function cannot fit the 290 K decay.

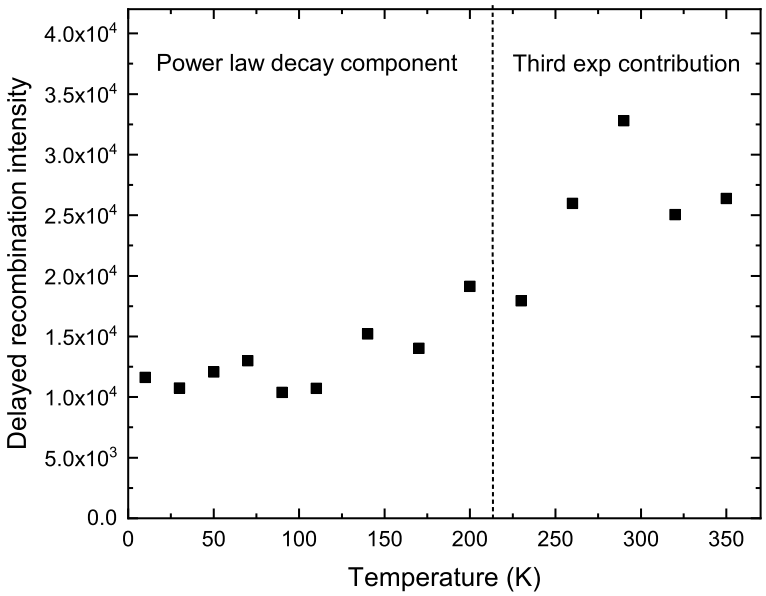

Figure 5.9: Delayed recombination intensity evaluated as the integral of the third component of the decay in the 0 – 5 μs time range.

The two faster components can be ascribed to the decay of Ce^{3+} luminescence, accompanied by non-radiative recombinations and/or energy transfer processes, that introduce distortions in the initial part of the curve, with respect to the single exponential decay expected for the transition of Ce^{3+}.
On the other hand, the slow tail in the scintillation decay can be attributed to the trapping of free carriers at shallow traps, which causes a delay in the recombination on the luminescent centers, as already introduced in Section 5.1.

In Figure 5.7(c), the vertical dashed line makes the distinction between the three-exponential analysis (on the right) and the results obtained by the fit procedure with Eq. 5.9 (on the left side). While the main contribution (w_2) does not feature any temperature dependence, an increase of the relative weight of the slow component (w_3), coupled to a decrease of the weight of the faster one (w_1) with increasing temperature, is clearly visible, thus confirming the trend previously observed in the curves of Figure 5.7(a).
Examples of the fits at 30 K and at 290 K is reported in Figure 5.8: a fit attempt by Eq. 5.9 has been performed also at T > 200 K without achieving a satisfactory reconstruction of the experimental data.

The delayed recombination intensity, evaluated as the integral of the third component in the entire time window considered in the measurement (5 μs), is reported in Figure 5.9 versus temperature: it can be considered a way to quantify the influence of traps on the recombination mechanism and it becomes more significant as the temperature increases.

The presence of a power law decay below 200 K, and of its evolution in an exponential decay in the μs time scale at higher temperatures, deserves further comments.
As pointed out in Sections 5.1.2 and 5.1.3, a power law time decay can be due to either (1) the occurrence of athermal tunneling between traps and Ce luminescent centers, or to (2) a recombination process involving detrapping to the delocalized bands of carriers from distributions of traps, typical of disordered systems. A simultaneous presence of both recombination pathways is obviously also possible. In order to better disclose the recombination mechanism, phosphorescence and thermally stimulated luminescence measurements have been performed, and are described in the following sections.

5.4 Phosphorescence

To clarify the role of defects in the processes involved in the recombination mechanism in Ce-doped silica, phosphorescence time decays * after X-ray irradiation at constant temperature were measured in the 10 - 320 K range and in time intervals up to 1 h. Within all this temperature range, the decays are of closely similar shape, as reported in panel (a) of Figure 5.10, and follow the formula

$$I(t) = A(t - t_0)^{-p} \tag{5.11}$$

where $I(t)$ is the phosphorescence amplitude, A and t_0 are constants, and $0.8 < p < 1$, except for T = 320 K, where $p = 0.5$. The parameter p converges to a value close to 1 and shows a slight temperature dependence up to 260 K, as displayed in panel (b) of Figure 5.10.

Similarly to what discussed above for the scintillation measurements, also in the case of phosphorescence the observation of a power law decay is in principle compatible with both the occurrence of athermal tunneling and of a distribution of trap levels. Indeed, both slow decay scintillation components and phosphorescence are connected to the same kind of mechanism - i.e. a delayed recombination triggered by carrier detrapping from defects; the only difference between the two phenomena lies in the different time scales of observation.
As already pointed out before, both processes can occur together. The relative probability of an electron tunneling pathway and a pathway through the conduction band depends upon concentration of defects and active recombination centers: close trap-center pairs can recombine via tunneling as well as via the conduction band, while distant pairs only via the conduction band. The distance between trapped electrons and recombination centers affects the tunneling luminescence much more than other factors, like temperature and trap depth, as demonstrated in [107].

*In several texts, the term phosphorescence is used to indicate the photo-luminescence emission from forbidden transitions between energy levels of a single center, as opposed to fluorescence that applies for allowed transitions. To avoid confusion, we will omit this meaning and use the term phosphorescence only to indicate the emission mechanism involving a trap and an emission center as distinct entities.

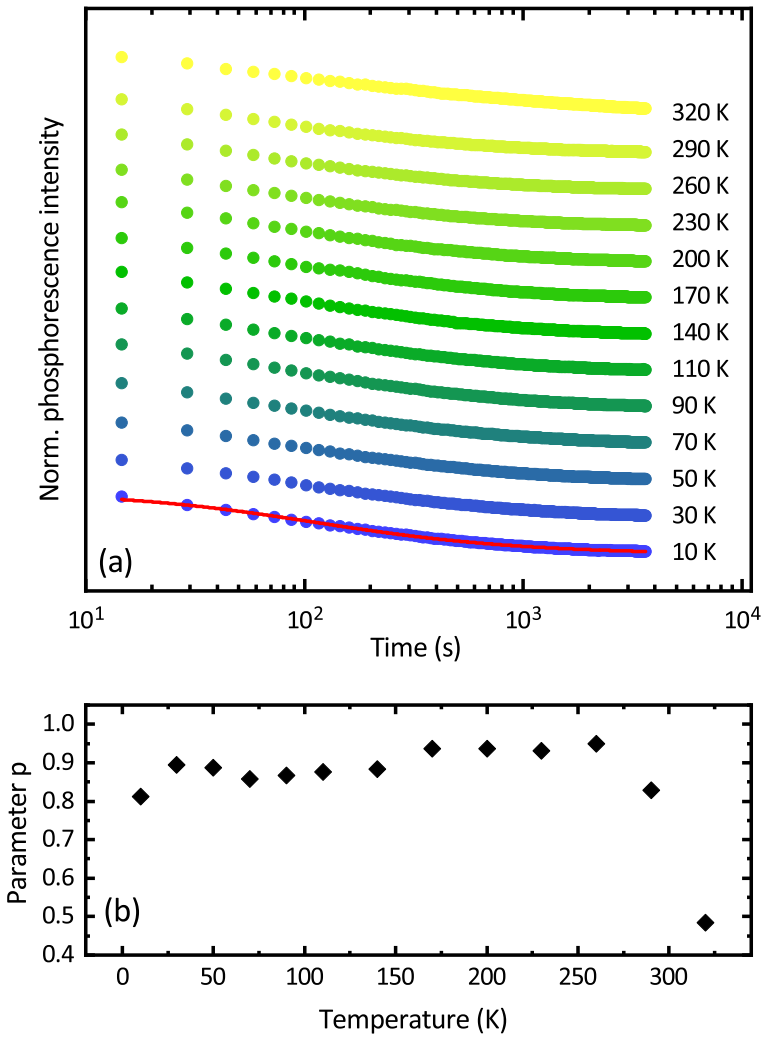

Figure 5.10: Panel a: phosphorescence decay at different temperatures, marked in the figure, after X-ray irradiation. Curves are shifted on the ordinate scale for better clarity. An example of the fit is displayed for T = 10 K by solid line. Panel b: temperature dependence of parameter p of the phosphorescence decay fit following Eq. 5.11.

5.5 Thermally stimulated luminescence

Wavelength-resolved TSL measurements were also performed to investigate trap levels which might affect the prompt radiative recombination. Measurements were carried out both in the 10 - 320 K interval after 10 K irradiation, and in the 300 - 700 K interval after RT irradiation. The heating rate was 0.1 K/s and 1 K/s, respectively.
Contour plots of the X-ray induced TSL response of Ce-doped silica fibers are displayed in Figure 5.11(a) and (b) respectively: the TSL intensity is reported as a function of emission wavelength (x-axis) and temperature (y-axis). Throughout the temperature range of the measurements, the emission is that related to the radiative $5d-4f$ transition of Ce ions, which means that carriers released from traps recombine at Ce centers.
Thermally released electrons could recombine, not necessarily radiatively, also with other hole traps; the fact that only the characteristic Ce^{3+} emission is observed is an evidence that the TSL process in silica fibers involves only electron traps.
The integration of the TSL signal over the whole emission range allowed the investigation of the temperature dependence of the TSL emission; in Figure 5.11(c) and (d) TSL glow curves below and above RT are reported, respectively.

A broad TSL structure is detected on the entire temperature range. In order to further elucidate the nature of the traps responsible for the TSL signal, a partial cleaning (PC) analysis [35] has been carried out in the 60 - 300 K range. We focused on this temperature region since it should reasonably include traps responsible for the slow scintillation decay contribution and the phosphorescence signal. The fibers were first irradiated at 10 K with approximately 120 Gy and then pre-heated at an intermediate temperature T_{stop}. After cooling down to 10 K, a TSL measurement was performed. In Figure 5.12(a), the effect of the pre-heating at different T_{stop} on TSL glow curves is shown. As T_{stop} rises, the TSL signal is reduced, due to the partial emptying of the TSL traps; moreover, the TSL glow curve maximum moves towards higher temperatures, suggesting the existence of a continuous distribution of the parameters describing the trap levels.

The initial rise method [35] was used on all partial cleaning measurements in order to evaluate the trap depths. When the logarithm of the rising portion of the TSL glow curve is displayed against T^{-1}, a linear behavior is expected, due to the *Arrhenius*-like dependence of the TSL signal versus temperature at the beginning of the trap emptying. The thermal depth of trap levels can thus be calculated by the slope of the curve:

$$I(T) \propto sn_0 \exp\left(\frac{-E_T}{k_b T}\right) \tag{5.12}$$

where E_T is the trap depth and s the frequency factor. This is an approximation of the more complex relation between TSL intensity, temperature, and trap parameters, valid in the initial portion (up to $\sim$ 10 % of the maximum intensity) of the glow peak.
In Figure 5.12(b), the Arrhenius plots of the glow curves are shown: the temperature range over which an exponential dependence over T is noticed is wide (in the case of a single-peak structure such a dependence is expected up to a few percent of the glow curve maximum), and the slope of the curves increases as T_{stop} increases.

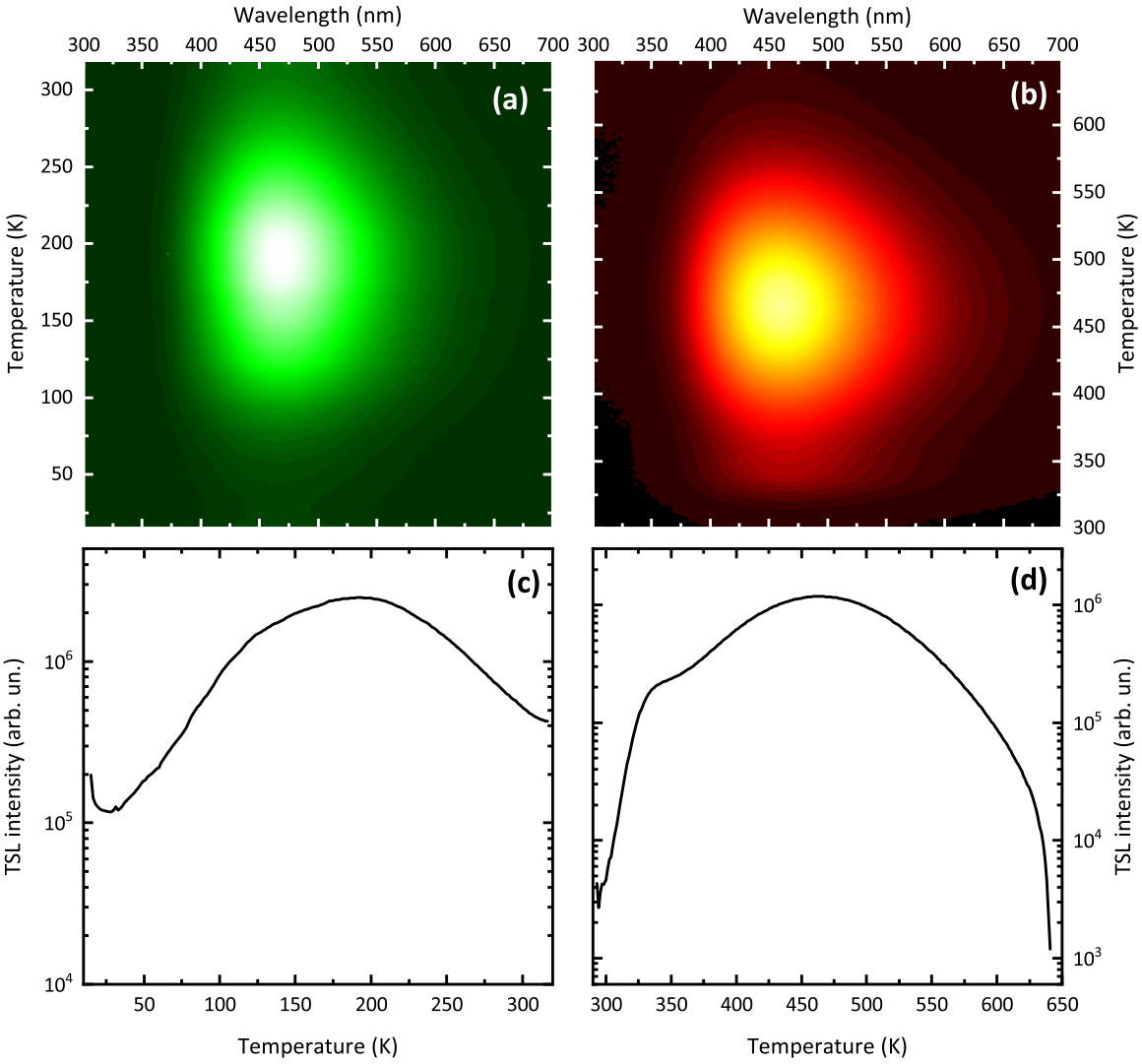

Figure 5.11: Top panels: contour plots of wavelength-resolved TSL measurements obtained after X-ray irradiation at 10 K (panel a) and at RT (panel b). Bottom panels: TSL glow curves obtained after integration of wavelength-resolved measurements, shown in top panels, from 350 nm to 700 nm.

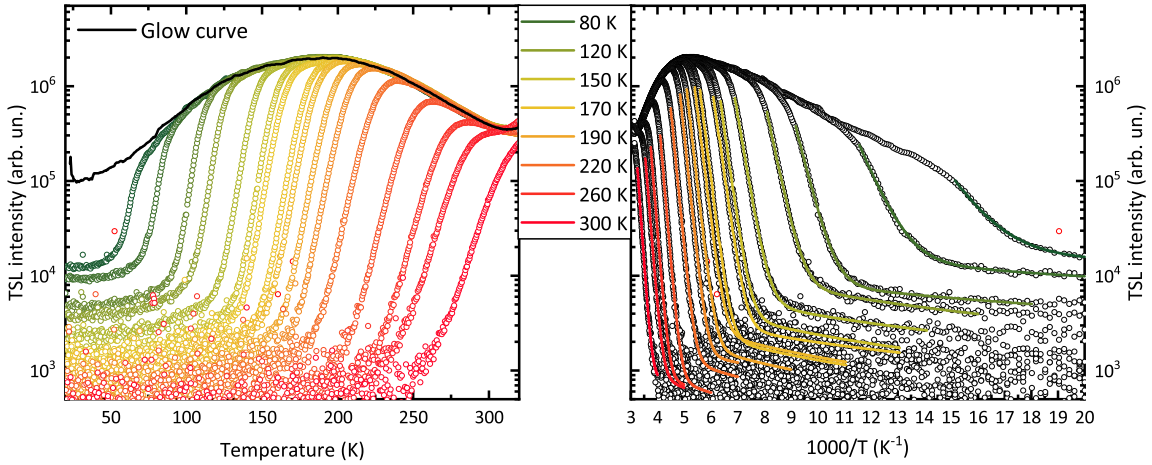

Figure 5.12: Left panel: TSL glow curves after 10 K X-ray irradiation and partial cleaning at different T_{stop} temperatures from 60 K to 300 K. Right panel: Arrhenius plot of the TSL measurements; the continuous lines are the fits with a sum of a single exponential and a power law contribution.

Both these features are consistent with a continuous distribution of trap parameters. In addition, an almost flat component is observed, particularly evident at the lowest temperatures. Therefore, the curves of the right panel of Figure 5.12 have been numerically analyzed according to the formula:

$$I(T) \propto I_0 \exp\left(\frac{-E_T}{k_b T}\right) + BT^{-p} \tag{5.13}$$

If we consider that a linear heating rate is employed for the TSL measurement, indeed the second term of the formula describes an athermal decay proportional to the inverse of time.

The trap energy values as a function of T_{stop} are reported in Figure 5.13: they range from approximately 0.1 to 0.8 eV, and an uncertainty of 5 % can be associated to them, according to results obtained in previous works [53]. Thus, the presence of a wide distribution of trap depths is demonstrated.

A strong peak superposition and comparable amplitudes prevent a clear appearance of distinct energy values in the curve of Figure 5.13, which simply displays a continuous distribution of energies without any modulation. The presence of a quite large trap energy distribution indicates that such electron traps can influence in a complex way the scintillation properties of the material.

The contour plots of TSL measurements presented in Figure 5.11 reveal that the only recombination centers active in the TSL process are Ce ions: no emissions were observed due to point defects of the silica matrix. However, a similar structure in the TSL of pure bulk silica was previously observed [97, 108], evidencing the intrinsic character of defects acting as traps. The hole nature of recombination centers indicates that electron traps are involved in the TSL process in silica: oxygen deficient centers seem the most probable candidates to act as electron traps in the material, as already discussed and demonstrated in the literature in the case of pure and RE-doped bulk silica [53, 97].

In most of Ce-doped oxide scintillators, electron traps are indeed the dominant defects, which negatively influence the scintillation mechanism [109, 110].

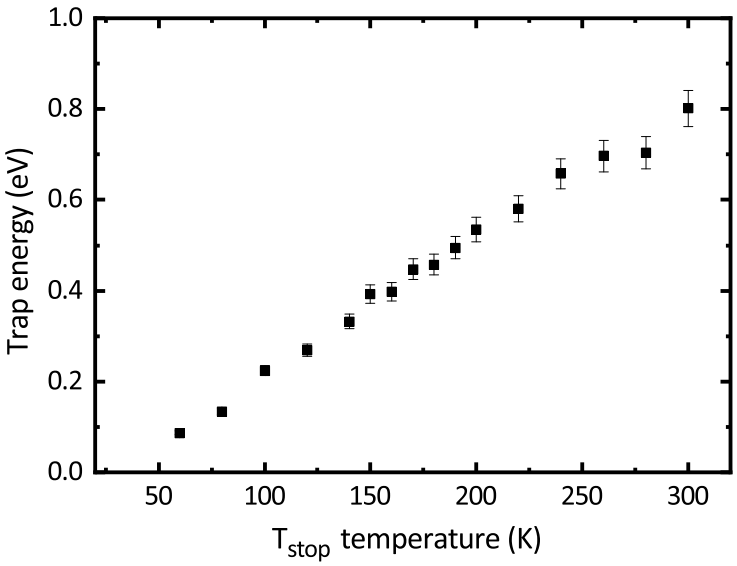

Figure 5.13: Distribution of trap energy values calculated by the initial rise method versus T_{stop} temperature.

In the frame of a first order recombination kinetics, it is possible to evaluate the frequency factor s of a trap by the following expression

$$s = \frac{\beta E_T}{k_b T_M^2} \exp\left(\frac{E_T}{k_b T_M}\right) \tag{5.14}$$

where β is the heating rate and T_M is the maximum temperature of the TSL peak.
Indeed, first order kinetics is confirmed in this case by the lack of any shift in the glow curve shape by varying the X-ray dose, as demonstrated by the data reported in Figure 5.14.

In principle, it would be then possible to evaluate the lifetime of the traps as a function of temperature:

$$\tau = s^{-1} \exp\left(\frac{E_T}{k_b T}\right) \tag{5.15}$$

However, due to the broadness of the curve and the observed superposition between the multiplicity of peaks, Eq. 5.14 can hardly be applied, because T_M can barely be evaluated for each component. Therefore, we chose to consider a mean frequency factor $s \sim 10^{10}$ Hz, as previously reported in the literature [53, 97].

We recall that our aim is to search for a possible correlation between traps observed in TSL and those responsible for scintillation slow decay components and phosphorescence signal. To this scope, trap lifetimes were calculated at the temperatures at which scintillation and phosphorescence decays were measured. An extremely wide range of lifetimes is obtained; thus in Figure 5.15 only the lifetimes of the portion of trap distribution that lie from approximately 10^{-7} s to 10^3 s are reported, which can reasonably be related to slow scintillation tails and phosphorescence.

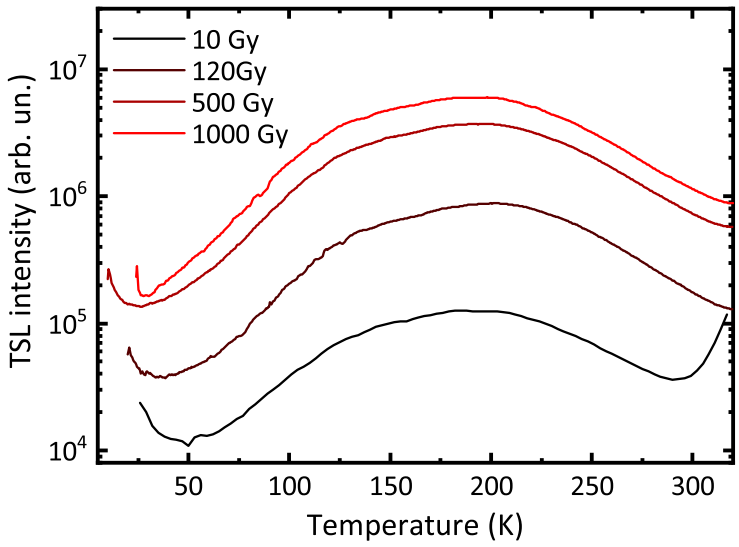

Figure 5.14: TSL glow curves as a function of 10 K X-ray irradiation dose. The shape of the glow curve remains unchanged as the trapped carrier concentration varies; this confirms the occurrence of the first-order kinetics of recombination of carriers released from traps.

From Figure 5.15, it is evident that the whole trap distribution is involved in the delayed recombination processes: however, the shallow traps affect more the low temperature decays, whereas the deeper ones act at higher temperatures.
Moreover, TSL data display also the occurrence of an athermal recombination evident at the lowest temperatures (Figure 5.12).
Therefore we can conclude that both a distribution of energy levels and athermal tunneling can account for the complex scintillation decay detected.

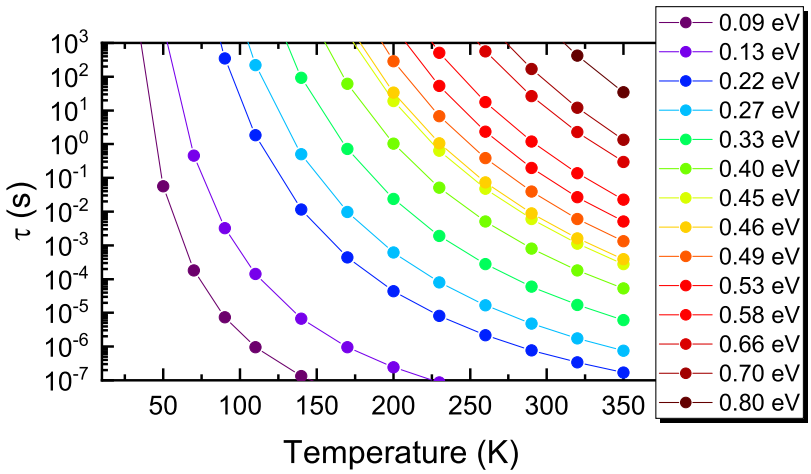

Figure 5.15: Distribution of traps lifetimes evaluated by Eq. 5.15 at various given temperatures, corresponding to those of scintillation decay measurements. Only values in the 10^{-7} s to 10^{3} s are reported because the traps with lifetime in this time scale can be related to the slow component of the scintillation decay and to the detected phosphorescence signal.

5.6 Conclusions

In scintillators, the occurrence of carrier trapping during irradiation is considered detrimental because it causes a lengthening of the scintillation kinetics or a reduction of the light yield. Although preparation technologies are continuously improved, the presence of a certain amount of lattice defects is very common even for a pure material synthesized in very controlled conditions.

This study, involving TSL, phosphorescence, RL sensitization, and time-resolved scintillation, revealed the presence of a continuous distribution of trap levels typical of amorphous materials; the observed electron traps are characterized by thermal energies similar to those already observed in other silica forms. A relationship between electron traps and intrinsic defects in the material, possibly oxygen vacancies, can be established.

A tight correlation between delayed recombination decay and defects acting as carrier traps delaying the radiative recombination has to be considered, as well as a close interplay of intrinsic defects with luminescent ions during the scintillation process; the relationship between trapping centers, TSL glow curves, and delayed recombination processes revealing the complicated dynamics of carrier trapping, detrapping, and recombination as a function of temperature has been here investigated.

Although the correlation between traps, scintillation, and phosphorescence remains qualitative, TSL results provide a justification for the power law decay governing slow scintillation tails and phosphorescence signal; they are most probably due to the recombination of carriers from a temperature-dependent portion of the detected wide trap distribution as well as to athermal tunneling between traps and luminescent centers.

The fact that above 200 K the slow component of the scintillation emission decay does not fit a power law function anymore is in accordance with the narrowing of the TSL glow curve, which is due to the distribution of traps getting narrower. A good agreement between the TSL results and the analysis of the scintillation decay profiles is thus demonstrated.

The results presented in this work can help to increase the fundamental comprehension of defect-driven phenomena, and can be extended to materials other than silica. Moreover, they could stimulate the improvement of synthesis technologies aimed at the control of the material defectiveness.

Chapter 6

Dual Cherenkov and Scintillation Response to high energy electrons

---

Current and future ionizing radiation detectors need novel materials and concepts to improve and optimize their performances. On the basis of the possibility of growing a great variety of fiber shapes and lengths, several calorimeter designs have been proposed [8], exploiting the flexibility of fibers to adapt for various needs. Fiber technology can allow a cost-effective implementation of the dual-readout approach to HEP measurements. Moreover, fibers enable the design of detectors with high spatial resolution, good timing properties, and radiation tolerance, which are essential requirements for future calorimeters [73].

Dual-readout calorimetry was proposed as a technique to determine the electromagnetic shower fraction for individual events, by comparison on an event-by-event basis of the signals generated in the form of Cherenkov and scintillation light [111]. It has recently been considered to improve the performance of hadronic calorimeters in future collider experiments (i.e., for the forthcoming high-luminosity phase of the LHC at CERN) [112].
As described in Section 1.3, scintillation light is proportional to the total energy deposited by the electromagnetic shower particles, while Cherenkov light is produced only by charged, relativistic particles, which are almost exclusively found in the electromagnetic shower component. Several approaches were suggested for the dual-readout concept: among them, either the use of two independent active media or the *a posteriori* decomposition of scintillation and Cherenkov components of the light emitted by the same material [9, 18].

Besides HEP experiments, dual readout is involved in several other fields. Dual Cherenkov and scintillation readout has for example been proposed for calibration and monitoring of high-energy-electron-beam profiles in radiotherapy and for the optical imaging of ionizing radiation in the clinical field [113, 114]; in addition, it can be used for applications in security, industrial x-ray imaging, and radiography [115, 116]. Furthermore, dual readout can be exploited to probe the transport of energetic solar particles, allowing the coverage of the energy range from tens to hundreds of MeV with a single detector [117].

This thesis is aimed at deepening the investigation of the possible application of RE-doped sol-gel silica fibers for HEP calorimetric experiments, in view of their potential use for the simultaneous Cherenkov and scintillation dual readout approach. In order to discuss their suitability with respect to this application, it is necessary to study their behavior under high energy particles beam probe.

A brief description of the complex of accelerators at CERN will be given at first, to introduce the beam line used for these experiments. In Section 6.2, the experimental setup of the test beam and the procedure followed for data analysis are reported. The main part of this chapter is then devoted to the discussion of the obtained results.
The content of this chapter has been published in [118].

6.1 Calorimetry at CERN

During the last 70 years, a complex of accelerators was built at the European Organization for Nuclear Research (CERN) and energies progressively higher could be reached for the study of new physics.

Linear accelerators (LINAC) are the first elements of the accelerator chain. The protons, obtained from hydrogen atoms from which electrons have been removed, are accelerated along a straight line to an energy of 120 MeV. Then three successive synchrotron accelerators, the Booster, the Proton Synchrotron (PS) and the Super Proton Synchrotron (SPS), bring their energy respectively to 1.4, 26 and 450 GeV. Once or twice a day, the protons of the SPS are injected into the LHC and accelerated to their final energy. With its 27.6 km, the LHC can store a lot of particles but the objective is not to collide them all at once: the particles are organized in bunches spaced by 50 ns. At the collision points, the two beams intersect and protons of the two bunches collide. An accurate operation of each component in the accelerator chain, sketched in Figure 6.1, is in principle able to provide between 10 and 20 hours of collisions. At the collision points, four huge underground caverns host complex detectors. The two largest experiments are ATLAS and CMS, designed to investigate the largest possible range of physics.

The tunnel hosting the Large Hadron Collider spans the Franco-Swiss border near Geneva. The LHC has its two beams composed of either protons or lead ions. When being accelerated transversally (as it is in a circular accelerator), light particles such as electrons lose energy through synchrotron radiation. On the contrary, hadrons like those accelerated in the LHC, are not limited by synchrotron radiation since their mass is much higher. The upper limit of their energy is fixed instead by the maximum value achievable for the magnetic field of the accelerator. To force the particles to follow circular trajectories, intense magnetic fields are indeed required. When the particle energy increases, then this magnetic field must increase as well. To reach the 14 TeV collision energy planned by the LHC original design, 8.3 T are required. This very intense magnetic field is obtained with superconducting magnets of niobium-titanium (Nb-Ti) operated at 1.9 K.

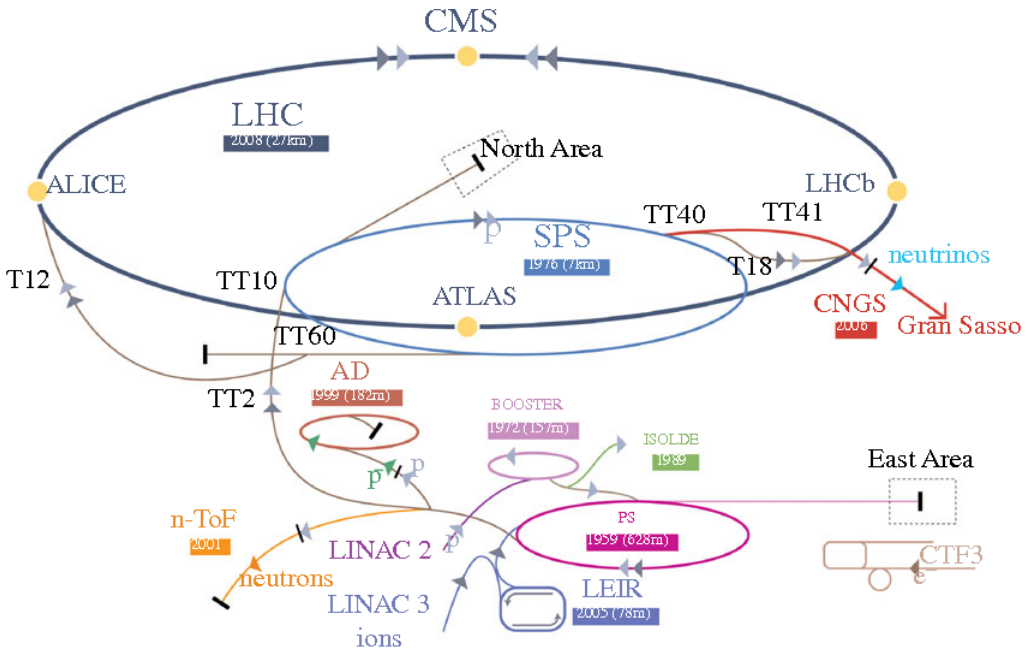

Figure 6.1: Complex of accelerators at CERN [119].

Nevertheless, starting from the first collisions at 7 TeV in March 2010, the performances of the LHC have been impressive: fine-tuning of the machine then allowed to increase the collision rate. On the 4^{th} of July 2012, the LHC received a lot of attention when it was officially announced that the huge number of these high energy collisions led to the discovery of the Higgs boson that the Standard Model predicts. The LHC thus successfully opened a track for new physics and new answers.

6.2 Experimental setup

The test with electron beams in the energy range from 20 to 200 GeV was performed at the H4 beam line of the CERN Super Proton Synchrotron North Area facility.

Ce-doped sol-gel silica fibers, produced as described in Section 3.1, are embedded in a W-Cu (75 %:25 %) absorber block of dimensions 60 × 60 × 200 mm^3 made of square 1.1 × 1.1 mm^2 holes, 1.8 mm apart, to obtain a sampling Spaghetti Calorimeter (*SpaCal*) prototype, shown in Figure 6.2(a), in which the fibers are used as the active scintillating material. These dimensions and fiber packing are optimized according to practical constraints.

Five distinct channels of fibers in the SpaCal module are sketched in Figure 6.2(c) and filled with 80 fibers each, for a total bundle diameter of approximately 15 mm: the fibers are YAG:Ce (central channel), silica doped with 0.002 % Ce (top left), Kuraray SCSF-3HF plastic used as a reference (top right), silica doped with 0.05 % Ce (bottom left), and silica doped with 0.0125 % Ce (bottom right).

We decided to focus the investigation on the response of Ce-doped silica fibers with the highest Ce concentration compared to that of plastic fibers used as a commercially available scintillator reference.

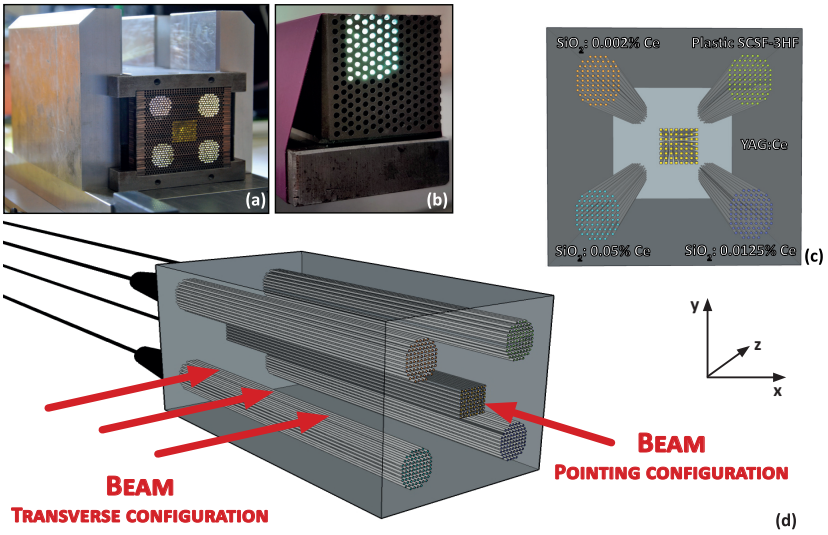

Figure 6.2: SpaCal setup. (a) Photograph of the SpaCal prototype made of five channels with 80 fibers each in a tungsten-copper absorber. (b) Picture of a min-Spacal prototype filled with 50 Pr-doped fibers. (c) Front view of the SpaCal prototype: the labels describe the type of fibers in each channel. (d) Side view of the SpaCal module, showing the pointing and transverse configurations.

A set of six Hamamatsu Photonics R5380 photomultiplier tubes with bialkali photocathodes and borosilicate glass windows of 20 mm diameter are used to readout the light from the fibers in the SpaCal module: the top channels are read out only from the rear side and the bottom channels are read out from both sides of the fibers to exploit the use and the advantages of the double side readout technique, already introduced in Section 4.2.2 [11, 77]. A silicon-rubber optical interface (EJ-560, Eljen Technology) with refractive index of 1.43 is used to couple the fibers and the PMT window to improve light extraction.

The module is mounted inside a light tight aluminum box providing optical and thermal insulation, with a water-cooled system to maintain a constant temperature of 18 $\pm$ 0.5 °C: the box is installed on a remotely controlled horizontal-vertical (x-y) table with a displacement range of $\pm$ 300 mm and positioning accuracy of approximately 1 mm. The frame of reference has the x axis horizontal on the experimental table, the y axis pointing vertically upward, and the z axis aligned with and pointing in the same direction as the beam line.

The module is exposed to the beam in two different configurations, described in Figure 6.2(d), hereafter referred to as *pointing* and *transverse*. In the former case, the beam is aligned with the fibers; the secondary particles, produced during the primary interaction of the high energy electrons impacting on the absorber developed all along the fiber length, while laterally extending inside the fiber bundle. The transverse dimension containing on average 90 % of the shower energy deposition (Moliére radius, introduced in Section 1.1.2) is estimated to be approximately 17 mm. In this configuration, the analysis of the time decay of the emitted light intensity (denoted as *pulse-shape*) and the study of the response of the fibers as a function of the varying incident-beam energy are performed. In the transverse configuration, the beam is impinging at a cross angle with respect to the fibers in order to analyze the attenuation profiles through a position scan, moving the table in discrete steps of approximately 30 mm.

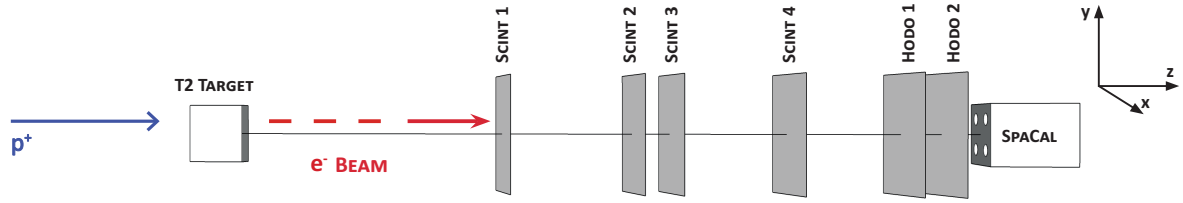

Figure 6.3: The last stage of the H4 beam line at CERN SPS. The SpaCal prototype, the scintillation counters, and the hodoscopes used in the analysis are shown. The blue arrow represents the primary proton beam impacting on the target; the red arrow represents the electron-beam direction.

6.2.1 Beam line

At CERN, the high energy protons of the SPS (see Figure 6.1), which are partly injected into the LHC rings, are also available in dedicated beam lines for test purposes.

These tests were performed at the CERN beam line H4, in the north area of the SPS, located on the site of Prevessin. This beam line provides mono-energetic particles produced by the high energy protons accelerated in the SPS. After extraction from the SPS, the primary protons are directed towards a production target (T2) made of beryllium, to generate secondary particles, including electrons and pions. The desired subset of secondary particles is then filtered with magnets and collimators and sent in vacuum pipes to the test areas.

In particular, electron beams in the 20–200 GeV range with hadron and muon contamination below 0.2 % were used for this experiment. The incoming electrons are detected by a set of four plastic scintillation counters used to trigger the data-acquisition system. The beam is composed of subsequent electron packets lasting 4 s and separated by around 30 s. Each packet contains approximately 10^4 electrons, among which approximately 10^3 are useful for the measurements exploiting the coincidence with plastic scintillation counters. The impact point of the beam particles on the module is accurately measured with two sets of beam hodoscopes, shown in Figure 6.3. Each set comprises two orthogonal planes of 64 scintillating fibers with square cross section of 0.5×0.5 mm^2, read out by a multianode PMT. Each plane provides, respectively, a measurement of the electron position in the x direction and the y direction with a nominal precision of less than 200 μm [120].

6.2.2 Experimental procedure

The coincidence of signals from the beam counters is used to generate the trigger for the event acquisition, while the hodoscopes allow reconstruction of the impact point of the electrons on the SpaCal module. The signals from the PMTs are digitized by a CAEN V1742 module operating at a sampling speed of 2.5 GHz and providing a time gate for the recorded pulses of 350 ns.

The response of a particular channel varies with the impact point, due to the variation of the shower containment and the consequent change of the energy deposited within the active volume: the center of each channel is defined as the position where the maximum response is observed, and this maximum is obtained by a fit to the measured response profiles with a

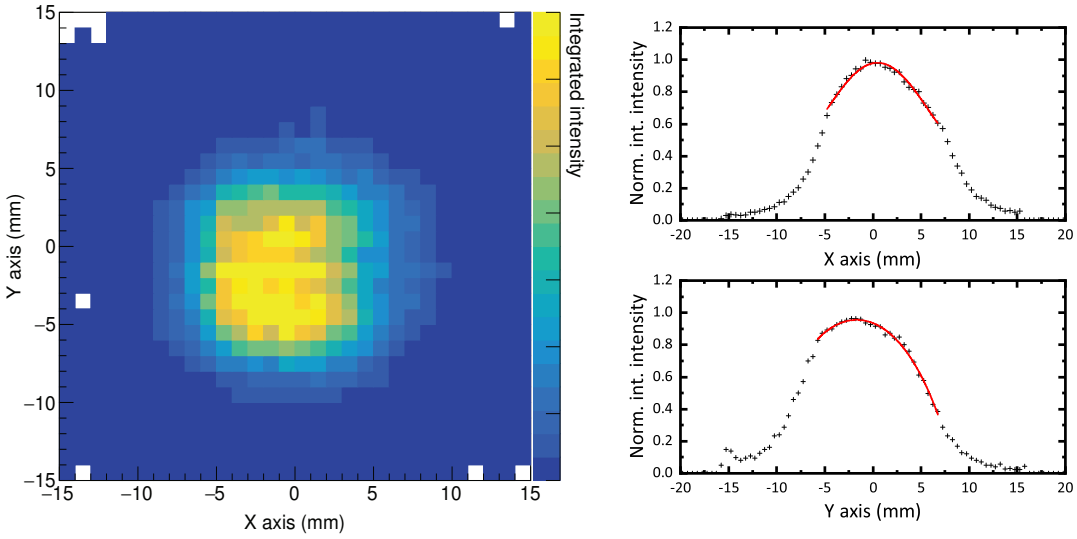

Figure 6.4: The left panel shows a contour plot of the fiber average integrated intensity as a function of the impact point along x and y axes for a 150 GeV electron beam with the module in the pointing configuration. A beam-spot selection of 20 mm^2 is considered for the analysis. The right panels show projections of the average integrated intensity of a fiber channel as a function of the impact point along the x axis (top-right panel) and the y axis (bottom-right panel). Red lines represent a polynomial symmetric fit function $A(x-x_0)^4 + B(x-x_0)^2 + C$ used to determine the channel center.

fourth-order polynomial, as illustrated in the right panels of Figure 6.4. This procedure allows the module to be correctly centered on the beam.
The left panel of Figure 6.4 shows a plot of the beam profile in the pointing configuration as detected by the rear PMT of the Ce-doped-fiber channel. Selection of a beam spot of 2.5 mm radius from the center of the bundle, corresponding to an area of 20 mm^2, is applied to limit shower transverse leakage.

After the position of each channel is determined, the high voltage supplied to each PMT is adjusted to have the highest signal without saturation: it is set to 1700 V for Ce-doped silica fibers and 800 V for plastic fibers. This setting allows the use of the same PMT gain for the whole energy scan in the 20–200 GeV range.
Energy scans are performed with the beam incident on the center of each fiber bundle for 20, 50, 100, 150, and 200 GeV electrons.

As a last step, the whole box containing the module is rotated by 90 ° clockwise to have the beam impacting on the lateral side of the fibers, allowing measurements of the attenuation length. A contour profile of the signal from Ce-doped silica fibers in this latter configuration is shown in Figure 6.5, as detected by the left PMT: it is the superposition of six different measurements obtained by shifting the detector in steps of 30 mm to allow the reconstruction of the attenuation profiles, further discussed in Section 6.3.4.

Before comparison of the signals from different channels, the photodetectors are intercalibrated in the laboratory. The intercalibration coefficients account for channel-by-channel response variations, due to the photocathode quantum efficiency and fiber-to-PMT optical coupling, and variations mostly related to the different high voltage applied to fit within the dynamic range of the analog-to-digital converter (ADC) and thus different amplification gain.

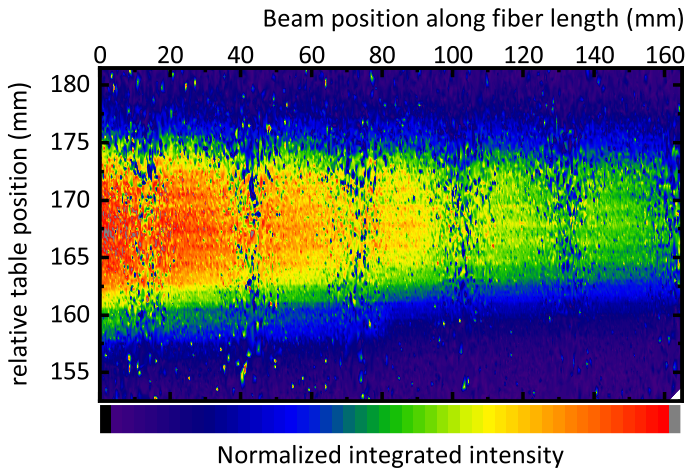

Figure 6.5: Fiber signal in the transverse configuration as a function of beam position moving from left to right as detected by the left photodetector. On the z axis, the integrated intensity normalized to the maximum reported from 0 to 1 on a linear scale is displayed. The vertical blue stripes are due to the small number of events at the edges of the beam profile when the table position is changed discretely in steps with respect to the beam.

To estimate the amount of light produced in each fiber bundle, an absolute calibration of the photodetector response is also performed. A $Lu_{2(1-x)}Y_{2x}SiO_5$:Ce crystal of 1 mm^3 is used as a reference and measured under exposure to a ^{137}Cs γ source with each PMT used in the test beam experiment: the reconstructed distribution is compared with that of a calibrated PMT to get the ADC-to-photoelectron conversion factors.

6.3 Test beam results

The test beam experiment and the following analysis provide a thorough investigation of the scintillation properties of Ce-doped sol-gel silica fibers exposed to high energy electromagnetic particles. The response of these fibers to high energy electrons is studied with the SpaCal calorimetric module in both the pointing configuration and the transverse configuration, thus allowing the evaluation of scintillation decay time, light output, and attenuation length.

The discussion focuses first on the pulse-shape analysis and then on the reconstruction of the shower profile and energy. A method for discrimination of Cherenkov and scintillation light is proposed to conduct a separate analysis of the two components of the emitted light, strengthening the possibility of Ce-doped silica fiber applications for simultaneous dual readout.

6.3.1 Pulse-shape analysis

The waveforms from the different types of fiber in the SpaCal module are recorded in a 350 ns time interval and reported in the top panel in Figure 6.6: they are calculated by averaging over the selected events for 150 GeV electrons having their impact point within 2.5 mm radius from the center of a given channel, as described in the previous section.
SiO_2:0.002 % Ce fibers do not show any scintillation light, probably too weak to be detected, and no analysis is performed on their luminescence decay.

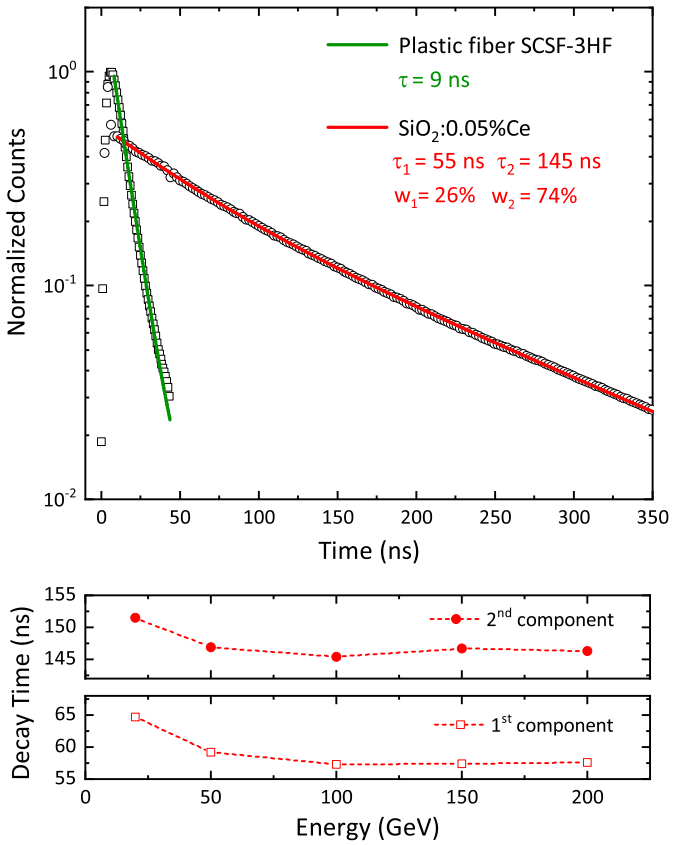

Figure 6.6: The top panel shows the normalized average pulse-shape of Ce-doped silica and plastic fibers (dotted lines) and a fit of the scintillation decay (solid lines) with a sum of exponential contributions for a 150 GeV electron beam. The decay time and weight for each component are reported. The bottom panels show the decay time for the two components of scintillation decay of Ce-doped silica fibers as a function of the incident energy. The lines are guides for the eye.

Attention focuses on the comparison between the decays of SiO_2:0.05 % Ce and plastic fibers, which are fitted by a sum of exponential contributions. Plastic fiber scintillation decay is characterized by a single component with decay time $\tau = 9 \pm 1$ ns, whereas Ce-doped silica fibers feature two contributions, with $\tau_1 = 55 \pm 5$ ns and $\tau_2 = 145 \pm 22$ ns, and fractional weights of 26 $\pm$ 3 % and 74 $\pm$ 3 %, respectively. The possible presence of a third, faster component cannot be inferred by this analysis, because the first part of the decay is strongly influenced by the fast Cherenkov emission.

In the bottom panel in Figure 6.6, the evolution of the decay time for the two components of the Ce scintillation decay is reported as a function of the incident beam energy: an overall longer scintillation decay time at the lowest energies can be observed for both components. We suggest that this effect can be ascribed, from a general point of view, to a variation of the excitation density in the material with decreasing incident energy, which consequently leads to differences in the scintillation recombination kinetics [121]. This phenomenon is the subject of further investigation, reported in Appendix A, in order to characterize and compare the scintillation kinetics of Ce-doped sol-gel silica fibers under various ionizing radiation sources with different distributions of excitation density in the material.

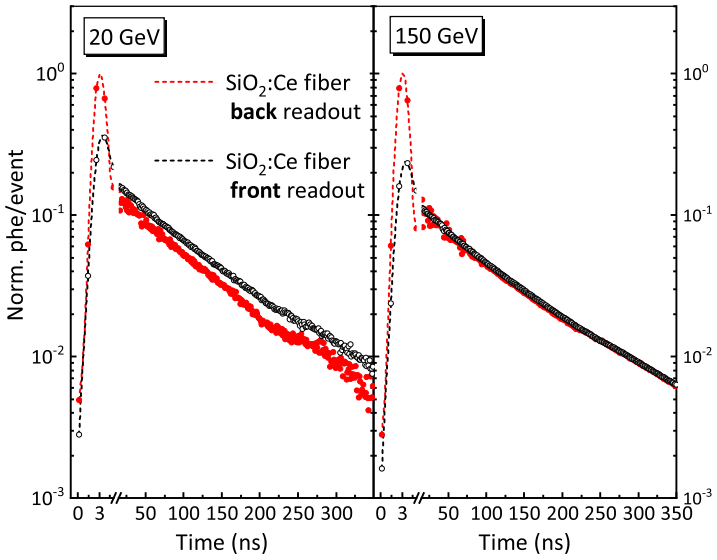

Figure 6.7: Average pulse-shape normalized to the number of events for SiO_2:0.05%Ce fibers for a 20 GeV electron beam (left panel) and a 150 GeV electron beam (right panel). Back and front readout are compared. The dashed lines are guides for the eye.

The decay times of Ce-doped fused-silica fibers produced by dissolution of the dopant in the glass matrix were reported by *Akchurin et al.* [122] and were evaluated to be 20.8 ± 5.4 ns and 93.0 ± 12.6 ns for τ_1 and τ_2, respectively, in a 200 ns time window, but with similar fractional weights. The shorter decay times, compared with those obtained in this study, can be ascribed to a different incorporation of Ce ions in the silica-based matrix studied in [122], containing a significant percentage of additional dopant ions, especially Al.

6.3.2 Discrimination of Cherenkov and scintillation light

In Figure 6.7 the average pulse-shape of 0.05 % Ce-doped silica fibers is displayed as recorded by the back PMT (red) and the front PMT (black) and normalized to the maximum of the back-PMT signal. The prompt emission, enlarged in the first part of the decay, can be ascribed to the Cherenkov effect [10, 123, 124], occurring in both the RE-doped core and the fluorinated cladding of glass fibers; the convolution with the scintillation emission has to be taken into account and, in the following, a detailed analysis is performed to distinguish the two contributions.
For confidence of the interpretations, we also report in Figure 6.8 the pulse-shape of 0.002 % Ce-doped silica fibers, for which the scintillation signal is too weak to be detected and only the Cherenkov contribution is visible.

Cherenkov light is emitted in the forward direction at a characteristic angle with respect to the track of the charged particle, as introduced in Section 1.3. Thus, the Cherenkov signal is expected to be higher in the rear detector, confirmed by the amplitude of the peak in the first part of the waveform.
On the other hand, scintillation emission is isotropic, and the same amount of scintillation light is expected in both the rear detector and the front detector, as observed in the case of

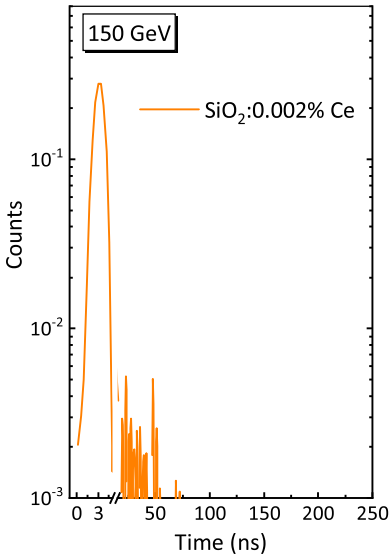

Figure 6.8: Average pulse-shape of 0.002%Ce fibers for a 150 GeV electron beam. The scintillation signal is too weak to allow its detection and therefore only the Cherenkov contribution can be visible.

150 GeV incident electrons (Figure 6.7, right panel). This occurs when the shower maximum falls approximately in the center of the fiber length, so that attenuation effects are the same for light traveling in the two directions.
For the lowest energy of 20 GeV (Figure 6.7, left panel), the scintillation light in the front PMT is more intense than in the rear PMT, thus proving the dependence of the position of the maximum of the shower L_{max} on the incident beam energy, described by Eq. 6.1 [125]:

$$L_{max} = X_0(4.2 + 1.8 \ln E) \tag{6.1}$$

where $X_0 = 0.8$ cm is the radiation length of the calorimeter prototype evaluated by *GEANT4* numerical simulation.

The average position of the shower maximum shifts toward the back of the absorber with the increase of the energy of incoming electrons: this change in the behavior of the shower profile along the longitudinal axis is expected to produce a different ratio R_{FB} of the front-PMT signal (S_{front}) and the back-PMT signal (S_{back}) measured at the two opposite ends of the fibers, defined in Eq. 6.2.

$$R_{FB} = \frac{S_{front}}{S_{back}} \tag{6.2}$$

In the top panels in Figure 6.9, R_{FB} is plotted against the position of the maximum of the shower L_{max} in centimeters on a semilogarithmic scale. The average ratio R_{FB} of the front-PMT and the back-PMT signal decreases due to the shift of the shower maximum toward the rear side of the absorber block at high energies. It is evaluated for both Cherenkov (left panel) and scintillation light (right panel), and a clear correlation with the beam energy can be observed and used for estimation of the attenuation length of the fibers with the calorimetric module in the pointing configuration, as discussed in [10].

The attenuation values so obtained are $L_{att,Ch} = 9 \pm 2$ cm and $L_{att,scint} = 25 \pm 6$ cm for Cherenkov and scintillation emission, respectively. The different nature of Cherenkov and scintillation light can account for the different correlations displayed in Figure 6.9.

In the bottom panels in Figure 6.9, the ratio of the Cherenkov signal to the scintillation signal as a function of beam energy is reported for the back readout (left) and the front readout (right) to evidence the different dependence of the two emissions on the shift of the shower maximum position toward the back of the module with increasing incident energy. The intensity of Cherenkov light increases in the back channel and decreases in the front channel faster than the intensity of scintillation, with the shower maximum moving toward the back, thus suggesting a greater attenuation of UV Cherenkov photons. This result is stressed in Section 6.3.4, where the attenuation length in the transverse configuration is evaluated for both emission contributions.

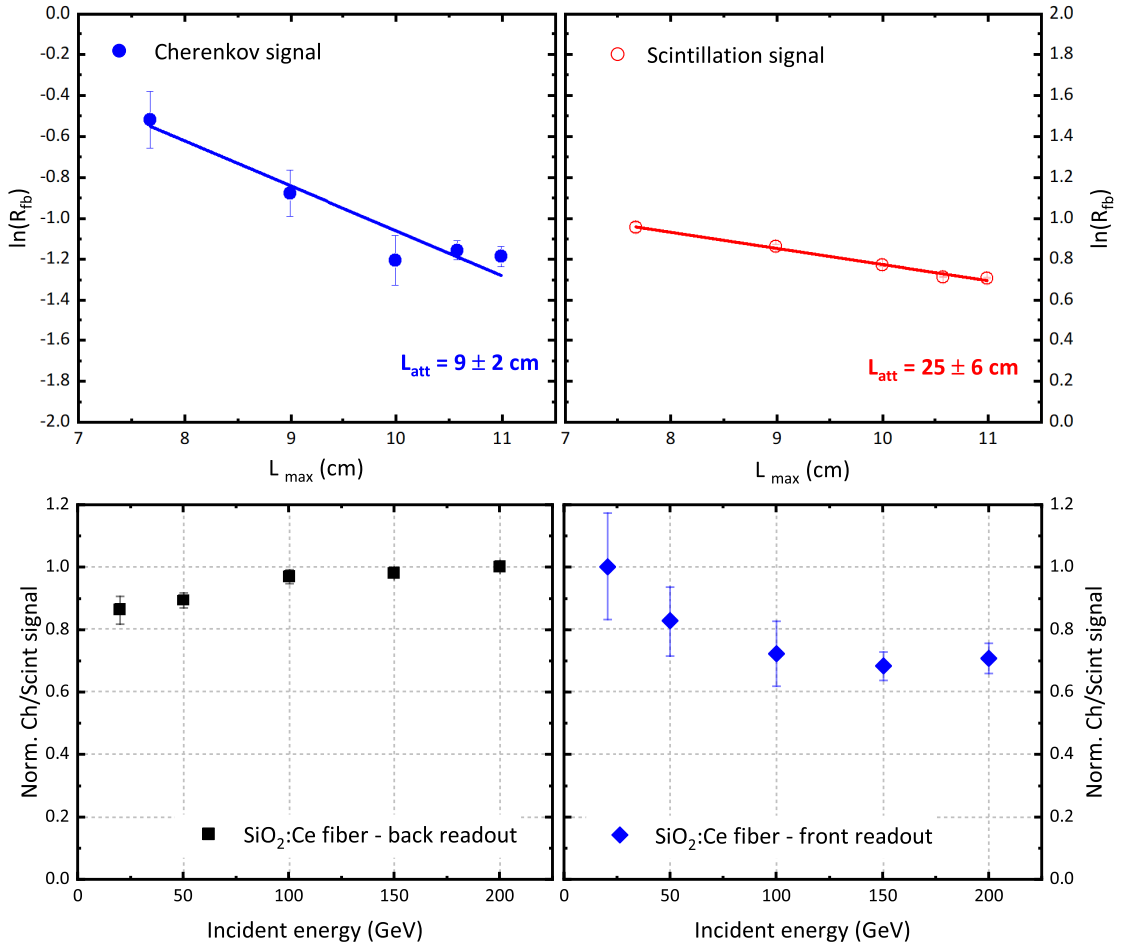

Figure 6.9: The top panels show linear correlation between the natural logarithm of the ratio of the front-PMT signal to the back-PMT signal and the position of the shower maximum in centimeters, proportional to the natural logarithm of the incident energy according to Eq. 6.1 for Cherenkov light (top-left panel) and scintillation light (top-right panel). The bottom panels show the ratio of Cherenkov (Ch) signal to scintillation (Scint) signal as a function of the incident energy for back readout (bottom-left panel) and front readout (bottom-right panel).

A separate study of Cherenkov and scintillation signals is performed through an event-by-event pulse-shape analysis, by integrating the waveform of the single selected event in different time intervals; namely, in the first 5 ns for Cherenkov emission, and in the remaining part for the scintillation contribution. This method leads to underestimation of the scintillation component because it does not take into account the scintillation signal emitted in the range $0 < t < 5$ ns, and thus a reconstruction of the true scintillation integrated emission has to be performed with use of the fit procedure conducted on the average waveform in Figure 6.6. By defining S and C as the integrated scintillation and Cherenkov emissions in the two separated time intervals calculated event by event, we can estimate the true integrated signals S_t and C_t by solving the following set of equations:

$$\begin{aligned} S_t &= \frac{S}{a} \\ C_t &= C - S \cdot \left(\frac{1}{a} - 1\right) \end{aligned} \tag{6.3}$$

where a is the ratio between scintillation integrated signal evaluated at $t > 5$ ns and the extrapolation to t = 0 ns of the area under the exponential decay fit curve of the average pulse shape displayed in Figure 6.6.

This method has been used to reconstruct the distributions of photoelectrons for both Cherenkov and scintillation emission for 150 GeV electrons beam, reported as an example in the top panels of Figure 6.10, where the ADC-to-photoelectrons coefficients have also been taken into account. A Gaussian fit has been performed on the reconstructed distributions in the 20 - 200 GeV energy range to estimate the peak positions. In the bottom panels of Figure 6.10, the position of the peak, converted in photons and divided by the incident energy, is reported as a function of the incident energy itself: the light readout by the rear PMT shows a stronger non-proportionality with respect to the front readout. Such a behavior can be related to the displacement of the maximum of the shower as a function of the incident energy, combined, only for Cherenkov component, with the directionality of the emission. In any case one can notice that Cherenkov light contribution is only a few percent with respect to scintillation for all energies. The Cherenkov light contribution is 10% and 2% of the signal for the back and front readout respectively, when the module is aligned to the beam direction.

We can conclude that under exposure to high energy particles beam probe, the two contributions of Cherenkov and scintillation light can be detected simultaneously with the same Ce-doped silica fibers bundle. A characteristic dual response of the fibers has been observed and the feasibility to carry out a well-distinguished analysis of the two components of the pulse-shape has been demonstrated.

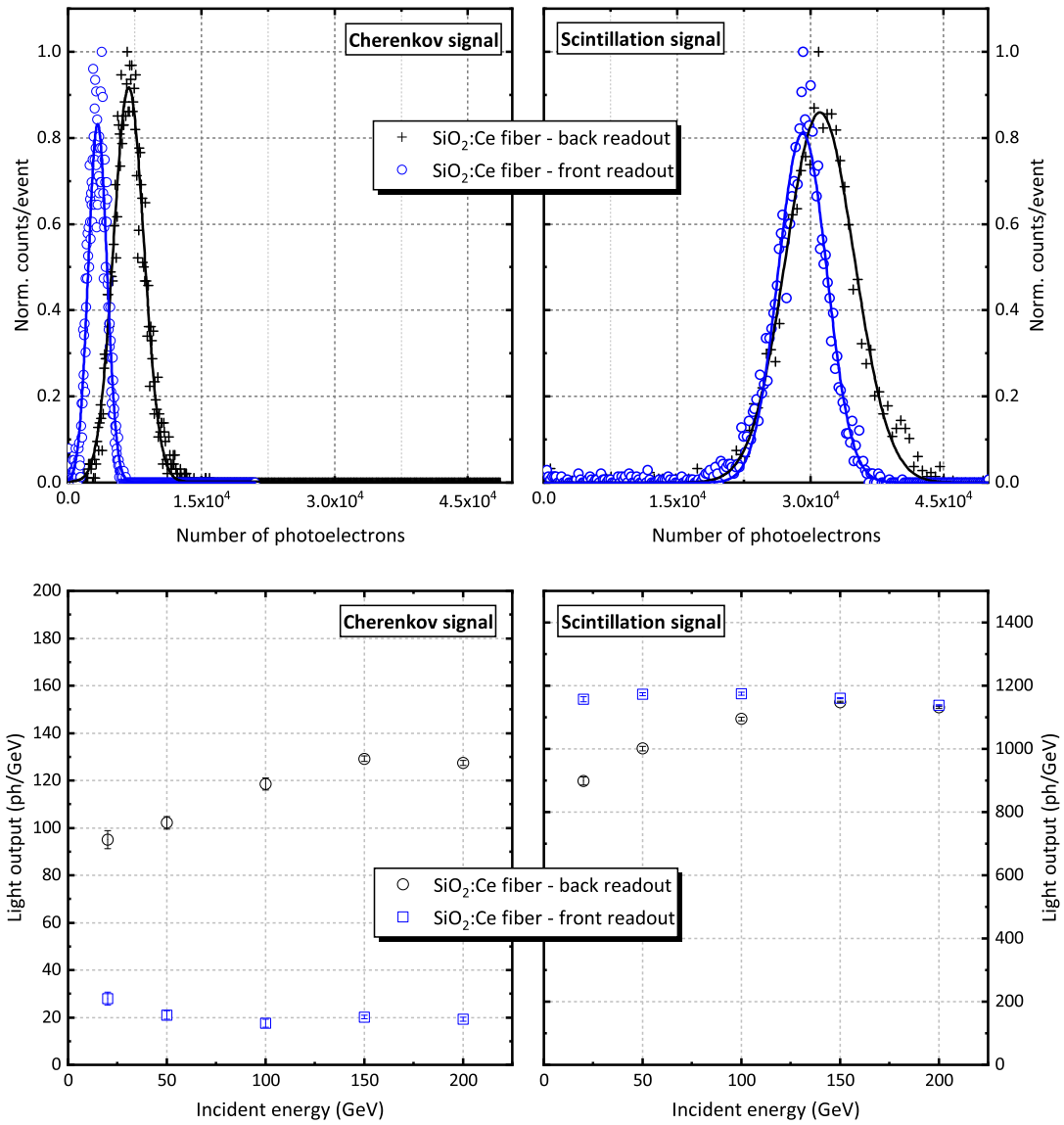

Figure 6.10: The top panels show normalized distributions of photoelectrons for Cherenkov and scintillation signals for SiO_2:Ce fiber readout from both the ends for a 150 GeV electron beam. The bottom panels show the correlation between light output of Cherenkov signal (bottom-left panel) and scintillation signal (bottom-right panel) and incident-beam energy. The y axis reports the number of photons (ph) per GeV of incident energy, which is not therefore an absolute scale of the light yield of the material. Error bars are within the size of data points.

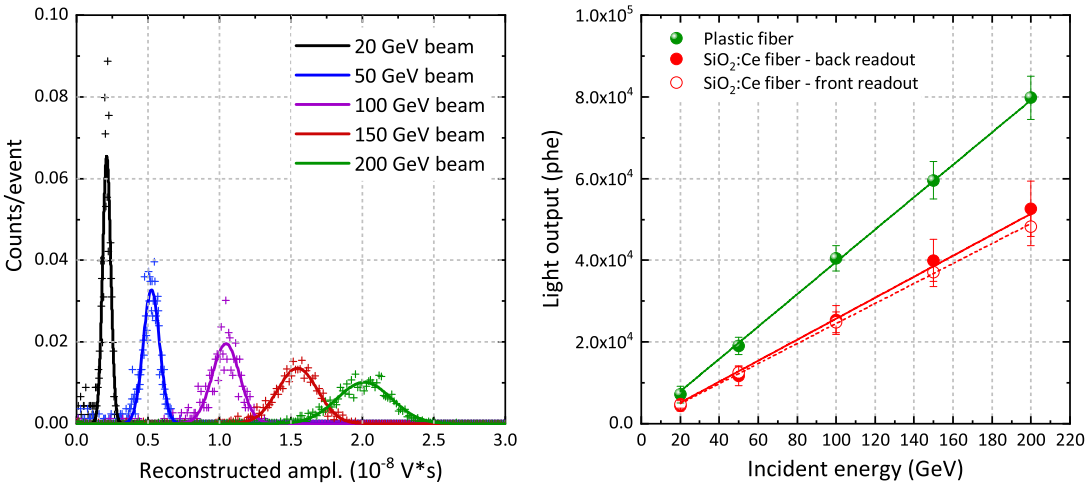

Figure 6.11: The left panel shows distributions of reconstructed amplitude at different beam energies. SiO_2:Ce fiber signal is reported. The right panel shows linear correlation between peak values of reconstructed amplitude distributions and incident beam energy. The light output in photoelectrons (phe) is evaluated.

6.3.3 Energy reconstruction and linearity

The particle energy can be reconstructed by application of intercalibration coefficients, calculated as described in Section 6.2.2, and with consideration only of events within a beam spot of 2.5 mm radius around the center of the fiber channel, to account only for electrons that develop the shower inside the fiber bundle. The total contribution is summed up event by event to reconstruct the signal, taking into account the ADC-to-photoelectron conversion factors.
The distributions of the reconstructed amplitude obtained in the 20–200 GeV range are shown in the left panel in Figure 6.11 for Ce-doped silica fibers and fitted with a Gaussian function to estimate the peak position and its width. The peak positions of the reconstructed amplitude distributions are converted to the number of photoelectrons and are reported in the right panel in Figure 6.11, where good correlation with the incident beam energy can be observed. A comparison of the light output of the different types of fibers is reported in the right panel in Figure 6.11, showing that plastic fibers are brighter than Ce-doped silica fibers by a factor 1.5. It should be taken into account that the density of the plastic fibers (1.2 g/cm^3) is lower than that of silica fibers (2.2 g/cm^3), and therefore the incident beam deposits a lower fraction of energy in the plastic fiber channel.
However, the higher density of silica fibers can be regarded as an advantage because it permits to devise calorimeters with a shorter Moliére radius compared with detectors that use plastic fibers as the active component; the shower is thus confined in a more compact area.

The energy resolution $\sigma E/E$ of the reconstructed amplitude, reported in Figure 6.12, is found to decrease with increasing incident energy, thus following the expected trend [126]: at 200 GeV it is estimated to be around 15 %, for Ce-doped silica fibers and lower for plastic fibers.

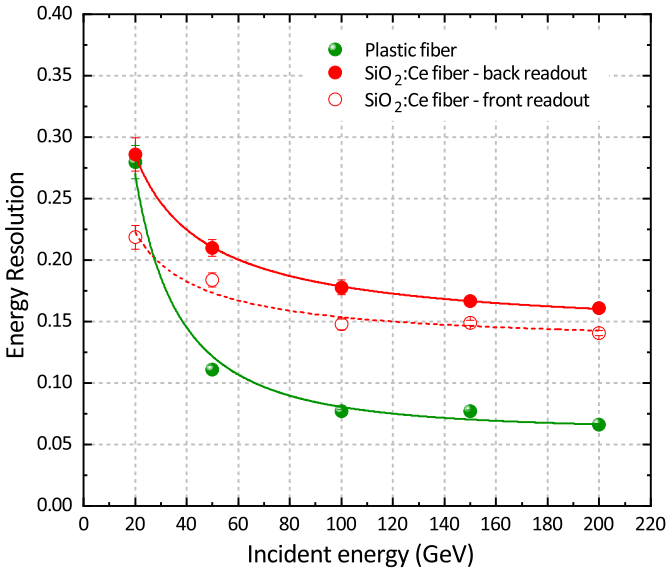

FIGURE 6.12: Energy resolution curves for SiO_2:Ce-doped fibers (red) and plastic fibers (green) as a function of beam energy. Both back (full circles) and front (open circles) readout channels for silica fibers are reported. Solid lines: fit to the experimental data, using Eq. 6.4.

This value mainly accounts for contributions from the partial transverse shower containment within a single fiber bundle and from the non-uniformity of the fibers themselves. Neglecting longitudinal shower leakage at high energies, the energy resolution of a calorimeter can be parametrized as a function of energy using the formula:

$$\frac{\sigma_E}{E} = \sqrt{\left(\frac{A}{\sqrt{E}}\right)^2 + \left(\frac{B}{E}\right)^2 + C^2} \tag{6.4}$$

where A represents the stochastic term, B the contribution from the electronic noise, and C the constant term. Stochastic fluctuations of the calorimetric response are related to the particle energy and arise from different sources along the chain of the probabilistic processes from energy deposition to signal generation and detection. Typical sources of constant term arise from shower leakage and spatial non uniformity of the response; more in general, all non statistical fluctuations contribute to the constant term of the resolution.

6.3.4 Attenuation length

A non-uniformity along the fiber length in the efficiency of the light extraction at the fiber ends, if not corrected for (e. g. by means of a double side readout [76]), can affect the response and the performance with high energy particles.

The attenuation length measurements described in the previous chapter have been repeated with 150 GeV electrons beam and the SpaCal module in transverse configuration, placing the table at 6 different x coordinates to obtain a nearly uniform scan of the entire length of the fibers. To enhance the signal, a beam spot selection of $\pm$ 2 mm along the y-axis has been applied for the computation of the energy deposit.

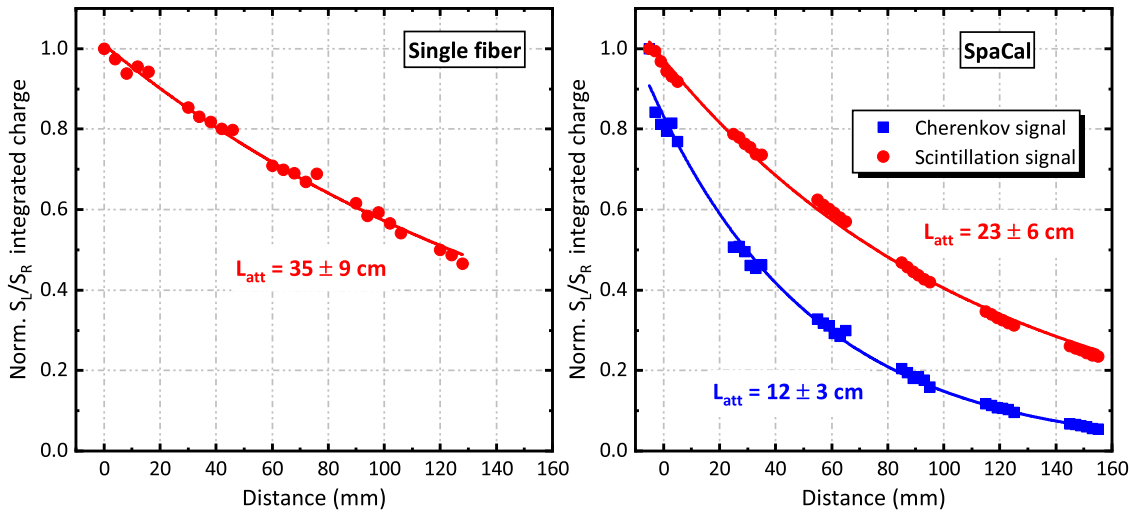

Figure 6.13: Attenuation length curves for SiO_2:Ce fibers measured in the transverse configuration under exposure to a 150 GeV electron beam and with use of the double-sided-readout technique: on the y axis, the ratio of the left-PMT signal to the right-PMT signal is reported. The left panel shows measurements of a single fiber with UV-sensitive PMTs. The right panel shows attenuation measurements in the SpaCal configuration. Discrimination between Cherenkov signal and scintillation signal is considered.

Exploiting the double side readout technique, the transverse profiles have been analyzed, parametrizing the curve with a single exponential decay according to Eq. 4.3.
Normalized transverse profiles and their fit are reported in Figure 6.13: both single fibers (left) and fibers bundle in the SpaCal module (right) have been measured, the former being readout with two UV-sensitive H6610 Hamamatsu Photonics PMTs, using two blocks of iron and lead as pre-shower. As explained in Section 4.2.2, attenuation curves have been obtained by computing the ratio of the right over left single channel signals, reported separately in Figure 6.14.

The discrimination of Cherenkov and scintillation signals has been performed for the fibers in the SpaCal module, and the attenuation length values estimated with the fit procedure are $L_{att,\ Ch} = 12 \pm 3$ cm and $L_{att,\ Scint} = 23 \pm 6$ cm for Cherenkov and scintillation emission respectively. Cherenkov light was observed to have a shorter attenuation length, thus confirming results shown in Figure 6.9 and described in the previous section: this could be ascribed to the fact that Cherenkov photons are mainly in the UV spectral region and have a higher probability therefore to be absorbed by Ce luminescent centers and by matrix defects. The difference observed in the evaluation of the attenuation length for Cherenkov emission between pointing and transverse configuration can be related to the directionality of the emitted Cherenkov photons, whose capture in the fiber depends on the orientation of the fiber axis with respect to the path of the charged particles.

For single fibers, only the analysis of the scintillation signal was possible, due to the presence of spurious signal from the PMT windows. Scintillation attenuation length was found to be worse in the SpaCal configuration with respect to single fibers ($L_{att,\ Scint} = 35 \pm 9$ cm):

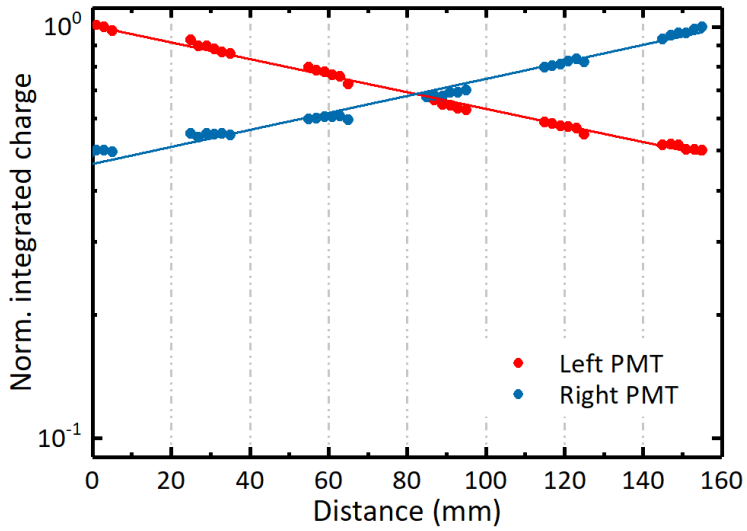

Figure 6.14: Normalized single channel signals for SiO_2:Ce fibers following a single exponential decay. A logarithmic scale on the y axis is used.

this could be related to the silica cladding in contact with the absorber, leading to a variation of the refractive index at the fiber boundary and to a loss in the total internal reflection efficiency, which causes an increase of the light leakage before reaching the photodetector.

A further optimization of the fiber cladding geometry and a proper quenching of the cladding light propagation modes are thus suggested by this analysis, in order to improve the light extraction through total internal reflection. Nevertheless, the attenuation profile measured in the beam test for the single Ce-doped silica fiber is in good agreement with laboratory measurements, reported in the previous chapter (refer to Figure 4.13).

6.4 Conclusions

The results obtained under the exposure to high energy electrons allowed a deep investigation of the scintillation properties of Ce-doped sol-gel silica fibers embedded as the active component in a Spaghetti-like electromagnetic calorimeter prototype. The decay time of Ce^{3+} scintillation, silica fiber attenuation length, and relative light output were evaluated by testing the SpaCal module both in pointing and transverse configurations with respect to the incident beam. The scintillation time decay was analyzed and the reconstruction of the shower profile and energy was addressed.

The feasibility of a simultaneous dual readout approach and the discrimination of Cherenkov and scintillation emitted light were demonstrated. The presented results support the potential applications and perspectives of silica fibers for dual readout calorimetry, as well as for beam monitoring, radiotherapy in the medical field, security, and industrial X-ray imaging.

Further material engineering will look for the optimization of the fiber geometry, to improve the light extraction from the fiber core together with the radiation hardness, in order to exploit the possibility that sol-gel silica offers to realize long scintillating fibers with good attenuation length in a cost-effective way.

Conclusions and Outlook

The aim of this PhD thesis was the study of scintillating RE-doped silica fibers, produced by sol-gel synthesis, with applications perspectives in the evolving field of high energy physics calorimetry.
The possibilities that sol-gel silica fibers offer are explored, and the new demanding requirements in terms of radiation hardness, fast timing, and scintillation performance are carefully verified for the operation in future HEP experiments.
A brief discussion of the main results and the investigations performed is here proposed, together with a view of the perspectives of this thesis.

The scintillation mechanism in silica host is activated by RE doping: Pr ion was at first selected because of its fast allowed $5d-4f$ transition with UV emission and time decay of the order of 20 ns. However, the exposure to high levels of ionizing radiation led to a degradation of the optical and scintillation response, resulting in the formation of radiation-induced point defects acting as color centers and causing re-absorption of the emitted light; this led to a worsening of the optical transmission and attenuation length.

Ce-doped sol-gel silica turned out to be a more suitable material to be optimized and engineered to satisfy the strict requirements for high energy physics applications. It was demonstrated to be a more radiation hard material compared to Pr-doped silica, and through both a spectroscopic and an operative approach it was shown that a possible solution for improving the resistance to irradiation consists in the reduction of the Ce content inside the core of the fibers. These results confirmed the idea that radiation-induced defects in silica are related to the presence of the dopant. Moreover, through a comparison of the optical properties of Ce-doped silica in bulk and fiber forms as a function of cumulated dose, it was found that the glass network structural reorganization, induced by the high temperature treatments occurring during fiber drawing, enhanced the radiation resistance of the material, probably due to a reduced concentration of optically active defects.

Sol-gel synthesis route offers the possibility to easily shape silica glass into fiber form and allows the production of a significant amount of fibers in a cost-effective way. Despite Ce-doped sol-gel silica fibers cannot fulfill strict radiation hardness requirements, they showed good scintillating properties and can thus represent a good candidate scintillator working in a low radiation environment.

The behavior of Ce-doped silica fibers as the active scintillating component of a small SpaCal calorimeter prototype was tested with beams of highly energetic electrons. The scintillation properties of the material were studied along with a preliminary evaluation of the calorimetric performances of the module. The feasibility of a simultaneous detection of the dual Cherenkov and scintillation emission was demonstrated, together with the possibility to carry out a satisfactory discrimination of the two components of the emitted light by an event-by-event based analysis. This feature opens application perspectives for the future generation of HEP calorimeters based on the dual readout approach, aiming at improving the energy resolution, affected by fluctuations in the electromagnetic fraction of the shower of secondary particles. The unique characteristic of a simultaneous detection of Cherenkov and scintillation light would allow the realization of calorimeters made of a single type of fibers to read the dual emission instead of two types of fibers with either different doping or different density. Ce-doped silica fibers were thus demonstrated to be a good scintillator material to be used in a Spacal geometry detector.

Besides HEP experiments, dual readout turns out to be useful in several other fields. Dual Cherenkov and scintillation readout has also been proposed for calibration and monitoring of high energy electron beam profiles in radiotherapy and for the optical imaging of ionizing radiation in the clinical field; in addition, it can be used for applications in security, industrial X-ray imaging, and radiography.

Moreover, good quality optical fibers allow the propagation of light over long distances and were proposed also as wavelength shifters for the collection and transport of light in HEP experiments, and for the realization of scintillating optical fiber sensors for remote real time dosimetry in medical systems.

The fundamental comprehension of the role of point defects involved in the scintillation process is of essential importance for a complete understanding of the underlying physical mechanism and for the optimization and the improvement of the performances: point defects were found to be detrimental for the scintillation response since they cause a delay in the recombination process which degrades the timing response and the light yield. Therefore, an engineering of the fabrication method looking towards a removal of intrinsic defects is foreseen; by this point of view, sol-gel method is a valuable tool because it permits to perform the synthesis by using high purity precursors, reducing the level of unwanted impurities.

The presence of a broad continuous distribution of trap levels, in the 0.1 - 0.9 eV energy interval, was demonstrated by thermally stimulated luminescence investigations, and correlated with the delayed component of the scintillation emission decay as a function of temperature. The slow component of the scintillation time decay follows a t^{-p} trend, with p close to 1, which can indicate both the presence of athermal tunneling recombination processes and the inhomogeneous broadening of defects levels in amorphous materials, as pointed out by thermo-luminescence results. The role of defects as competitors with luminescent centers in the trapping of charge carriers created upon irradiation was also disclosed by monitoring the behavior of the RL intensity as a function of the exposure time at different temperatures.

This thesis thus confirmed the potential of RE-doped silica fibers produced by sol-gel technique and allowed for optimistic perspectives. It helped to increase the fundamental understanding of the incorporation of RE ions in the silica matrix and could stimulate the improvement of synthesis techniques aimed at a better control of the material defectiveness.

Future work should aim at deeply disclosing the factors that contribute to enhance the resistance to irradiation and at further improvement of the fiber geometry, including the possible use of coatings and wrappings to significantly progress in the light propagation. An optimization looking towards a complete quenching of the cladding light propagation modes could be suggested to facilitate the light extraction from the fiber core.

From a fundamental point of view, the comprehension of the scintillation mechanism and of the origin of the slow tails in the emission decay deserves further studies: a key point is represented by the correlation of the scintillation response with the density of ionization, which could be investigated by exploiting experimental techniques and powerful simulations toolkit.

Appendix A

Scintillation decay as a function of excitation energy

Scintillation decay profiles as a function of varying incident excitation energy, from few eV to the MeV range, have been studied and compared, with the aim of investigating the relationship between the scintillation kinetics and the distribution of excitation density in the material under exposure to ionizing radiation sources.

In particular, five sources of different energy have been chosen: UV light at 4 eV, giving origin to a photo-luminescence emission, 15 and 40 keV X-rays, 511 keV γs from a ^{22}Na source, and 5.5 MeV α particles from a ^{241}Am source.

The PL decay measurement has been carried out at the Institute of Physics of the Czech Academy of Sciences (Prague, Czech Republic) by exciting Ce-doped silica fibers with a pulsed 310 nm LED and acquiring the spectrally unresolved signal with a PMT Horiba Jobin Yvon TBX-04.

The X-ray excitation was performed at the Lawrence Berkeley National Laboratory using a custom-made pulsed X-ray system consisting of an ultrafast laser (200 fs pulses at 165 kHz), a light-excited X-ray tube, a Hamamatsu R3809U-50 microchannel PMT and an Ortec 9308 ps time analyzer. The impulse response of the system is 100 ps FWHM. A description of the working principle and the first characterization of the apparatus can be found in [106].

Radioisotopes ^{22}Na and ^{241}Am were made available by the Institute of Physics of the Czech Academy of Sciences, where also the scintillation measurements have been carried out. The detection system by digital scope is equipped with a hybrid PMT PP0475B operated at 9 kV, and an oscilloscope self-triggered by the rise of scintillation pulse; the band width is 500 MHz and the FWHM of the instrumental response is about 10-15 ns. With the help of convolution, it is possible to evaluate decay time down to 3-5 ns with a precision of 10 - 20 %.

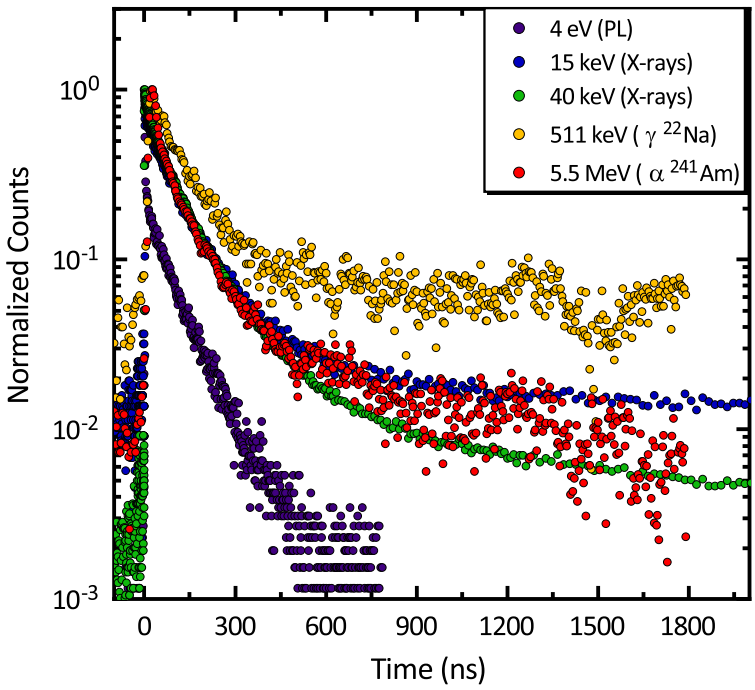

Figure A.1: PL decay (λ_{exc}= 310 nm, λ_{em} = 445 nm) and spectrally unresolved scintillation decay profiles of Ce^{3+} luminescence in a 2 μs time window. Data were normalized to their initial value and background counts subtracted. Various sources have been compared, varying in the energy and the type of incoming radiation.

A qualitative comparison of the decay curves obtained with the excitation sources previously listed is reported in Figure A.1. The presence of a slow component in the decay can be clearly observed in the scintillation profiles (X-rays, γ, and α sources) with respect to time-resolved PL: in the latter case, only the $4f - 5d$ transition of Ce recombination centers is selectively excited, and the relative decay time is that typical of Ce^{3+}, at around 100 ns. In fact, the PL emission process should not involve traps delaying the radiative recombination.

From these preliminary results, a dependence of the decay profile on the energy of the excitation source is difficult to identify, thus leading to the conclusion that a clear correlation between the distribution of excitation density and the slow component of the scintillation decay can barely be established.

A trend in the slow component of the decay at varying the energy of the incoming exciting radiation would suggest a different role of the material defects caused by a different density of the energy deposited along the track of the particle penetrating inside the medium. Moreover, the interaction of α particles with matter, involving ionization and excitation of the atoms, is completely different with respect to photons interaction, and was thus expected to give rise to a different scintillation response.

In order to further investigate how the density and type of excitation related to the energy deposition by an incoming particle in a medium can influence its scintillation response, simulations can be exploited in future work, to corroborate the experimental observations.

This topic deserves further in-depth analysis because it could represent a key point in the fundamental comprehension of the connection between the density of energy deposited by energetic ionizing radiation and the participation of defects in the recombination process.

Appendix B

RL sensitization and TSL in Pr-doped silica

In this appendix, the study of the role of the drawing process in modifying the distribution of trap levels in the silica host is proposed, and additional measurements on Pr-doped silica are reported.
The set of Pr-doped silica samples, introduced in Section 3.2.1, was chosen as an illustrative example.

The RL efficiency during exposure to ionizing radiation can reveal the role of point defects as competitors with the luminescent recombination centers in free carrier capture during irradiation, as already discussed in Section 5.2.1. The RL efficiency of all the Pr-doped silica samples investigated was found to increase after prolonged irradiation. The curves, normalized to their initial values, are reported in Figure B.1, where the relative intensity of the Pr^{3+} RL signal is displayed versus the cumulated absorbed dose during irradiation with 20 kV X-rays. The end of the irradiation sequence corresponds to a total cumulated dose of about 240 Gy. Each data point has been obtained by integrating the emission spectrum in the 240 - 945 nm range: this choice is justified by the fact that the spectral shape does not change during the measurements sequence.
In all the cases, the intensity of the RL signal increases towards a saturation value. Comparing all the samples and taking into account their respective positions along the fiber neck-down (Figure 3.2), it appears that such increase depends on the stage of the drawing process the sample derives from, and becomes more pronounced as the fiber condition is approached.

The inset of Figure B.1 shows an enlargement of the afterglow measurements carried out after the end of the irradiation. All the samples exhibit a luminescence signal, originated by the detrapping process, which becomes indistinguishable from the background level after some minutes. The afterglow curves do not follow a simple exponential decay; such behavior is in agreement with the presence of several trap levels exhibiting also inhomogeneous broadening. Once more, comparing all the samples, a progressive acceleration of the decay is observed by getting closer to the fiber condition.

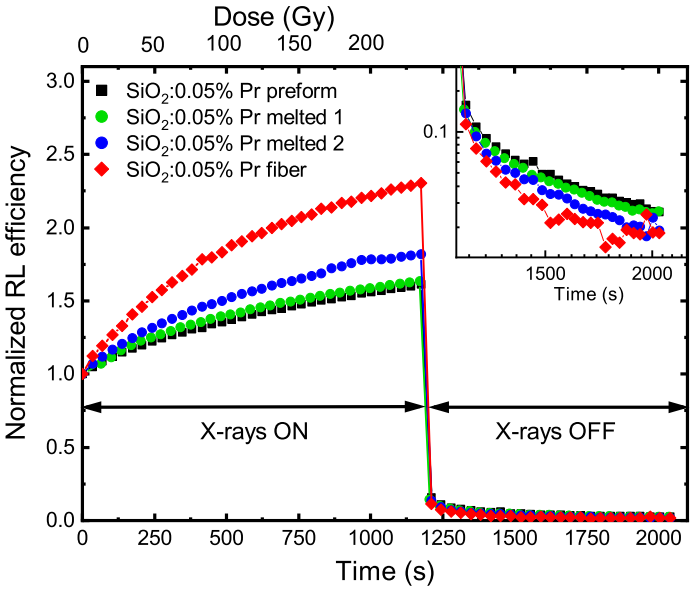

Figure B.1: (a) Room temperature RL efficiency of SiO_2: 0.05% Pr versus irradiation dose and time, for a total cumulated dose of 240 Gy. Each data point has been obtained by integrating the RL spectrum in the 240–945 nm range. Data are normalized to the initial value. (b) After the irradiation stops, the afterglow signal is detected as a function of time. In the inset, an enlargement of the afterglow decays is reported.

This result is opposite to what observed for Yb-doped fibers, studied in [50]. In this respect, we remark that Pr ions capture holes during irradiation: therefore, their afterglow luminescence is caused by the emptying of electron traps. The opposite occurs for Yb ions which capture electrons during irradiation, so their afterglow luminescence is caused by the emptying of hole traps. Different kinds of traps were found to display a different dependence upon the stage of the drawing process.

The results of wavelength-resolved TSL measurements obtained on all the samples after RT X-rays irradiation are reported in Figure B.2. The glow curves above RT related to the $5d-4f$ emission (a) are characterized by a dominant peak at about 90 °C and by a lower peak at approximately 230 °C; similar peaks are detected in the glow curves related to the $4f-4f$ emission (b), but with opposite relative intensity. The slight shift at higher temperature of the Pr-doped preform glow peaks is probably due to the difference in the sample thickness (2 mm) with respect to the other samples ($\sim$ 1 mm) causing a thermal lag during the sample heating. The different mutual intensity ratios of the TSL peaks obtained after integration on the $5d-4f$ (a) and $4f-4f$ (b) emissions might be related to a stronger thermal quenching of the $5d-4f$ emission with respect to that of the $4f-4f$ ones.

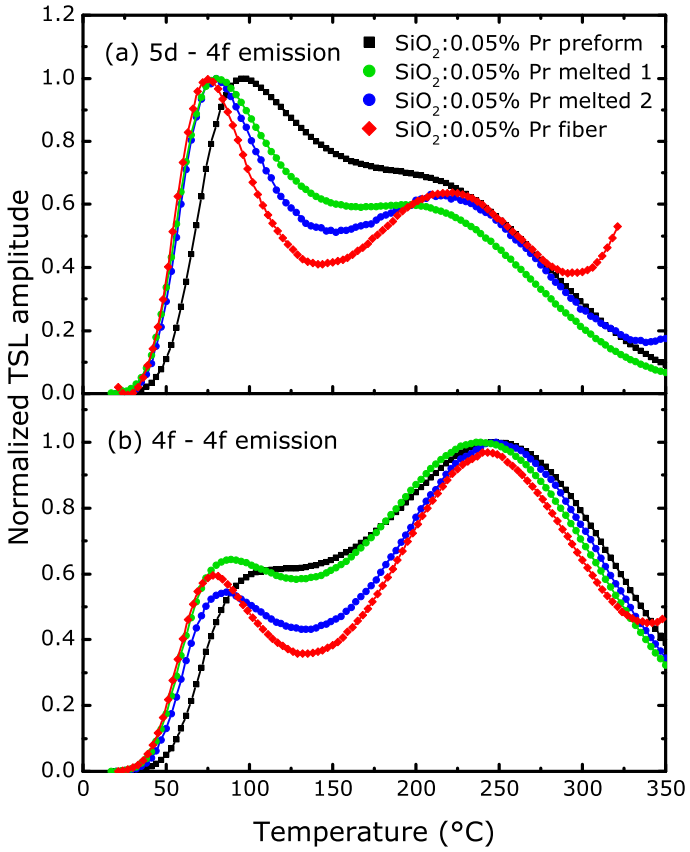

Figure B.2: TSL glow curves of bulk SiO_2:0.05% Pr and fiber obtained after 500 Gy X-rays irradiation at RT. A heating rate of 1 °C/s was adopted. The curves were obtained by integration of wavelength resolved TSL measurements from 270 to 370 nm (a) and from 570 to 670 nm (b) to independently investigate the temperature dependence of the two main Pr^{3+} emissions. The curves are normalized to their maximum values.

Similarly to what pointed out for RL hysteresis and afterglow, a dependence of the glow peak width on the stage of the drawing process can be clearly observed: the structures of the glow curves become better resolved, i. e. their width is significantly smaller, going from preform to fiber through the melted samples. This feature can be ascribed to a readjustment of the silica matrix due to the heating process required by the fiber drawing, which influences the localized trap levels and consequently the trap-related phenomena, like RL hysteresis, afterglow, and TSL emission.

References

[1] P. A. Rodnyi, *Physical Processes in Inorganic Scintillators*, CRC Press (1997).

[2] C. Dujardin, E. Auffray, E. Bourret-Courchesne, P. Dorenbos, P. Lecoq, M. Nikl, A. N. Vasil'ev, A. Yoshikawa and R. Y. Zhu, *Needs, Trends and Advances in Inorganic Scintillators*, IEEE Trans. Nuc. Sci. **65** (2018) 8 1977.

[3] R. Wigmans, *Sampling calorimetry*, Nucl. Instrum. Methods Phys. Res. **494** (2002) 1-3 277.

[4] CMS Collaboration *The Phase-2 Upgrade of the CMS Barrel Calorimeters* tech. rep. CERN-LHCC-2017-011 CMS-TDR-015 CERN, Sept. 2017.

[5] A. V. Zarubin, ed. *Perspectives on physics and CMS at very High Luminosity HL-LHC* 2012.

[6] P. Lecoq, *Metamaterials for novel X- or γ-ray detector designs*, IEEE Trans. Nuc. Sci. Symp. Conf. Record (2008) 1405.

[7] R. Y. Zhu, *A very compact crystal shashlik electromagnetic calorimeter for future HEP experiments*, J. Phys. Conf. Ser. **928** (2017) 012015.

[8] K. Pauwels, M. Lucchini, A. Benaglia and E. Auffray "Engineering of Scintillation Materials and Radiation Technologies" ed. by M. Korzhik and A. Getkin Springer International Publishing, 2017, p. 231.

[9] E. Auffray, D. Abler, P. Lecoq and G. Mavromanolakis, *Dual readout with PWO crystals and LuAG crystal scintillating fibers*, IEEE Trans. Nuc. Sci. **57** (2010) 1454.

[10] M. Lucchini, T. Medvedeva, K. Pauwels, C. Tully, A. Heering, C. Dujardin, K. Lebbou, P. Lecoq and E. Auffray, *Test beam results with LuAG fibers for next-generation calorimeters*, J. Instrum. **8** (2013) P10017.

[11] K. Pauwels, C. Dujardin, S. Gundacker, K. Lebbou, P. Lecoq, M. Lucchini, F. Moretti, A. G. Petrosyan, X. Xu and E. Auffray, *Single crystalline LuAG fibers for homogeneous dual-readout calorimeters*, J. Instrum. **8** (2013) P09019.

[12] V. Kononets, E. Auffray, C. Dujardin, S. Gridin, F. Moretti, G. Patton, K. Pauwels, O. Sideltskiy, X. Xu and K. Lebbou, *Growth of long undoped and Ce-doped LuAG single crystal fibers for dual readout calorimetry*, J. Cryst. Growth **435** (2016) 31.

[13] M. Nikl, K. Kamada, V. Babin, J. Pejchal, K. Pilarova, E. Mihokova, A. Beitlerova, K. Bartosiewicz, S. Kurosawa and A. Yoshikawa, *Defect engineering in Ce-doped aluminum garnet single crystal scintillators*, Cryst. Growth Des. **14** (2014) 9 4827.

[14] X. Xu, K. Lebbou, F. Moretti, K. Pauwels, P. Lecoq, E. Auffray and C. Dujardin, *Ce-doped LuAG single-crystal fibers grown from the melt for high-energy physics*, Acta Mater. **67** (2014) 232.

[15] K. Hara, K. Hata, S. Kim, M. Mishina, M. Sano, Y. Seiya, K. Takikawa, M. Tanaka and K. Yasuoka, *Radiation hardness and mechanical durability of Kuraray optical fibers*, Nucl. Instrum. Methods Phys. Res., Sect. A **411** (1998) 1 31–40.

[16] S. V. Afanasiev, P. de Barbaro, I. A. Golutvin, I. F. Emeliantchik, A. I. Malakhov, P. V. Moisenz, V. A. Smirnov and N. M. Shumeiko, *Improvement of radiation hardness of the sampling calorimeters based on plastic scintillators*, Nucl. Instrum. Methods Phys. Res., Sect. A **717** (2013) 11–13.

[17] H. Jivan, J. E. Mdhluli, E. Sideras-Haddad, B. Mellado, R. Erasmus and M. Madhuku, *Radiation damage effects on the optical properties of plastic scintillators*, Nucl. Instrum. Methods Phys. Res., Sect. B **409** (2017) 224–228.

[18] N. Akchurin, F. Bedeschi, A. Cardini, M. Cascella, G. Ciapetti, A. d'Orazio, L. Collica, D. De Pedis, R. Ferrari, S. Franchino, M. Fraternali, G. Gaudio, P. Genova, J. Hauptman, F. Lacava, L. La Rotonda, S. Lee, M. Livan, E. Meoni, A. Negri, D. Pinci, A. Policicchio, F. Scuri, A. Sill, T. Venturelli, C. Voena and R. Wigmans, *Detection of electron showers in dual-readout crystal calorimeters*, Nucl. Instrum. Methods Phys. Res., Sect. A **686** (2012) 125–135.

[19] A. Vedda, N. Chiodini, D. Di Martino, M. Fasoli, F. Morazzoni, F. Moretti, R. Scotti, G. Spinolo, A. Baraldi, R. Cappelletti, M. Mazzera and M. Nikl, *Insights into microstructural features governing Ce^{3+} luminescence efficiency in sol-gel silica glasses*, Chem. Mater. **18** (2006) 6178.

[20] A. Vedda, A. Baraldi, C. Canevali, R. Capelletti, N. Chiodini, R. Francini, M. Martini, F. Morazzoni, M. Nikl, R. Scotti and G. Spinolo, *Optical properties of Ce^{3+}-doped sol-gel silicate glasses*, Nucl. Instr. Meth. A **486** (2002) 259.

[21] A. Vedda, N. Chiodini, D. Di Martino, M. Fasoli, M. Martini, F. Moretti, E. Rosetta, G. Spinolo, M. Nikl, N. Solovieva, A. Baraldi and R. Capelletti, *Luminescence properties of rare-earth ions in SiO_2 glasses prepared by the sol-gel method*, J. Non-Cryst. Solids **345-346** (2004) 338.

[22] I. Veronese, C. De Mattina, M. Fasoli, N. Chiodini, E. Mones, M. C. Cantone and A. Vedda, *Infrared luminescence for real time ionizing radiation detection*, Appl. Phys. Lett. **115** (2014).

[23] A. Vedda, N. Chiodini, D. Di Martino, M. Fasoli, S. Keffer, A. Lauria, M. Martini, F. Moretti and G. Spinolo, *Ce^{3+}-doped fibers for remote radiation dosimetry*, Appl. Phys. Lett. **85** (2004) 26 6356.

[24] M. J. Berger, J. H. Hubbell, S. M. Seltzer, J. Chang, J. S. Coursey, R. Sukumar, D. S. Zucker and K. Olsen *NIST Photon Cross Section Database* https://www.nist.gov/pml/xcom-photon-cross-sections-database.

[25] G. F. Knoll, *Radiation Detection and Measurement*, Wiley (1979).

[26] M. J. Berger, J. Chang and J. S. Coursey *NIST Stopping Power and Range Table for electrons, protons and Helium Ions* https://www.nist.gov/pml/stopping-power-range-tables-electrons-protons-and-helium-ions.

[27] J. Beringer et al., *Review of Particle Physics*, Phys. Rev. D **86** (2012) 1.

[28] D. Groom and S. Klein, *Passage of particles through matter*, Eur. Phys. J. C **15** (2000) 163.

[29] R. Wigmans, *Advances in hadron calorimetry*, Annu. Rev. Nuc. Part. S **41** (1991) 133.

[30] R. Wigmans, *Calorimetry - energy measurement in particle physics*, Oxford University Press (2000).

[31] O. Ganel and R. Wigmans, *Quartz fiber calorimetry for LHC experiments*, Nucl. Instr. Met. A **365** (1995) 360.

[32] P. Lecoq, A. Annenkov, A. Gektin, M. Korzhik and C. Pedrini, *Inorganic Scintillators for Detector Systems*, Springer (2006).

[33] A. N. Vasil'ev "Relaxation of hot electronic excitations in scintillators: account for scatter- ing, track effects, complicated electronic structure" *Proceedings of the 5^{th} International Conference on Inorganic Scintillators and Their Applications (SCINT99)* 1999, pp. 43–52.

[34] S. Seifert, J. H. L. Steenbergen, H. T. van Dam and D. R. Schaart, *Accurate measurement of the rise and decay times of fast scintillators with solid state photon counters*, J. Instrum. **7** (2012) P09004.

[35] S. W. S. McKeever, *Thermoluminescence of solids*, Cambridge University Press (1985).

[36] F. P. Bowden and L. T. Chadderton, *Fission fragment damage to crystal lattices: dislocation formation*, Proc. R. Soc. Lond. **A269** (1962).

[37] B. P. Sobolev, *Multicomponent Crystals Based on Heavy Metal Fluorides for Radiation Detectors*, Inst. D'estudis Catalan (1994).

[38] G. Blasse and B. Grabmaier, *Luminescent Materials*, Springer-Verlag (1994).

[39] L. Skuja, *Optically active oxygen-deficiency-related centers in amorphous silicon dioxide*, J. Non-Cryst. Solids **239** (1998) 16–48.

[40] C. Grupen and B. Schwartz, *Particle detectors*, Cambridge University Press (2008).

[41] G. Mavromanolakis, *Quartz fiber calorimetry and calorimeters*, arXiv:physics/0412123 (2004).

[42] M. Lundin, *On the electromagnetic energy resolution of Cherenkov-fiber calorimeter*, Nucl. Instr. Meth. A **372** (1996) 359.

[43] F. Moretti, A. Vedda, N. Chiodni, M. Fasoli, A. Lauria, V. Jary, R. Kucerkova, E. Mihokova, A. Nale and N. Nikl, *Incorporation of Ce^{3+} in crystalline Gd-silicate nanoclusters formed in silica*, J. Lumin. **132** (2012) 461.

[44] A. Vedda, N. Chiodini, M. Fasoli, A. Lauria, F. Moretti, D. Di Martino, A. Baraldi, E. Buffagni, R. Cappelletti, M. Mazzera, P. Bohacek and E. Mihokova, *Evidences of rare-earth nanophases embedded in silica using vibrational spectroscopy*, IEEE Trans. Nucl. Sci. **57** (2010) 1361.

[45] N. Chiodini, G. Brambilla, A. Vedda, D. Di Martino, M. Fasoli, A. Lauria and M. Redaelli, *SiO_2-based scintillating fibres for X-ray detection*, SPIE **5198** (2004) 298.

[46] R. Becker, G. Dissertori, A. Gendotti, Q. Huang, D. Luckey, W. Lustermann, S. Lutterer, F. Nessi-Tedaldi, F. Pandolfi, F. Pauss, M. Peruzzi, M. Quittnat and R. Walny, *Proof-of-principle of a new geometry for sampling calorimetry using inorganic scintillators plates*, J. Phys.: Conf. Ser. **587** (2015) 012039.

[47] C. J. Brinker and G. W. Scherer, *Sol-Gel Science: the Physics and Chemistry of Sol-Gel Processing*, Academic Press (1990).

[48] N. Chiodini, M. Fasoli, M. Martini, E. Rosetta, G. Spinolo and A. Vedda, *High-efficiency SiO_2:Ce^{3+} glass scintillators*, Appl. Phys. Lett. **81** (2002) 23 4374.

[49] M. Fasoli, N. Chiodini, A. Lauria, F. Moretti and A. Vedda, *Effect of deep traps on the optical properties of Tb^{3+} doped sol-gel silica*, Phys. Stat. Sol. C **4** (2007) 3 1056.

[50] I. Veronese, C. De Mattia, M. Fasoli, N. Chiodini, M. C. Cantone, C. Moretti F. anc Dujardin and A. Vedda, *Role of optical fiber drawing in radioluminescence hysteresis of Yb-doped silica*, J. Phys. Chem. C **119** (2015) 15572.

[51] *Polymicro Technologies* 2011 `https://www.molex.com/molex/products/`.

[52] A. Mawardi and R. Pitchumani, *Optical fiber drawing process model using an analytical neck-down profile*, IEEE Photonics J. **2** (2010) 4 620.

[53] A. Vedda, N. Chiodini, D. Di Martino, M. Fasoli, L. Griguta, F. Moretti and E. Rosetta, *Thermally stimulated luminescence of Ce- and Tb-doped SiO_2 sol-gel glasses*, J. Non-Cryst. Solids **351** (2005) 3699.

[54] R. Reisfeld, A. Patra, G. Panczer and M. Gaft, *Spectroscopic properties of cerium in sol-gel glasses*, Opt. Mater. **13** (1999) 81.

[55] D. Di Martino, A. Vedda, G. Angella, M. Catti, E. Cazzini, N. Chiodini, F. Morazzoni, R. Scotti and G. Spinolo, *Evidences of Rare Earth Ion Aggregates in a Sol-Gel Silica Matrix: The Case of Cerium and Gadolinium*, Chem. Mater. **16** (2004) 3352.

[56] F. Moretti, N. Chiodni, M. Fasoli, L. Griguta and A. Vedda, *Optical absorption and emission properties of Gd^{3+} in silica host*, J. Lumin. **126** (2007) 759.

[57] M. Fasoli, F. Moretti, A. Lauria, N. Chiodini, A. Vedda and M. Nikl, *Radio-luminescence efficiency and rare-earth dispersion in Tb-doped silica glasses*, Radiat. Meas. **42** (2007) 784.

[58] F. Cova, M. Fasoli, F. Moretti, N. Chiodini, K. Pauwels, E. Auffray, M. T. Lucchini, E. Bourret, I. Veronese, E. d'Ippolito and A. Vedda, *Optical properties and radiation hardness of Pr-doped sol-gel silica: Influence of the fiber drawing process*, J. Lumin. **192** (2017) 661.

[59] M. Fasoli, A. Vedda, A. Lauria, F. Moretti, E. Rizzelli, N. Chiodini, F. Meinardi and M. Nikl, *Effect of reducing sintering atmosphere on Ce-doped sol-gel silica glasses*, J. Non-Cryst. Solids **355** (2009) 1140.

[60] Y. Shen, X. Feng, Y. Shi, A. Vedda, F. Moretti, C. Hu, S. Liu, Y. Pan, H. Kou and L. Wu, *The radiation hardness of Pr:LuAG scintillating ceramics*, Ceram. Int. **40** (2014) 3715.

[61] A. E. Geissberger and F. L. Galeener, *Raman studies of vitreous SiO_2 versus fictive temperature*, Phys. Rev. B **28** (1983) 3266.

[62] F. L. Galeener, *Planar rings in glasses*, Solid State Commun. **44** (1982) 1037.

[63] F. L. Galeener, *Band limits and the vibrational spectra of tetrahedral glasses*, Phys. Rev. B **19** (1979) 4292.

[64] A. Pasquarello and R. Car, *Identification of Raman defect lines as signatures of ring structures in vitreous silica*, Phys. Rev. Lett. **80** (1998) 5145.

[65] C. A. Taylor, M. F. Wayne and W. K. S. Chiu, *Residual stress measurement in thin carbon films by Raman spectroscopy and nanoindentation*, Thin Solid Films **429** (2003) 190.

[66] K. M. Davis, A. Agarwal, M. Tomozawa and K. Hirao, *Quantitative infrared spectroscopic measurement of hydroxyl concentrations in silica glass*, J. Non-Cryst. Solids **203** (1996) 27.

[67] A. Baraldi, E. Buffagni, R. Capelletti, M. Mazzera, S. Brovelli, N. Chiodini, A. Lauria, F. Moretti, A. Paleari and Vedda. A., *FTIR spectroscopy to investigate the role of fluorine on the optical properties of pure and rare earth-doped sol-gel silica*, J. Non-Cryst. Solids **353** (2007) 564.

[68] A. Agarwal, K. M. Davis and M. Tomozawa, *A simple IR spectroscopic method for determining fictive temperature of silica glasses*, J. Non-Cryst. Solids **185** (1995) 191.

[69] W. C. Oliver and G. M. Pharr, *Measurement of hardness and elastic modulus by instrumented indentation: Advances in understanding and refinements to methodology*, J. Mater. Res. **19** (2004) 1 3.

[70] A. C. Fischer-Cripps, *Critical review of analysis and interpretation of nanoindentation test data*, Surf. Coat. Tech. **200** (2006) 4153.

[71] R. Tandon, *A technique for measuring stresses in small spatial regions using cube-corner indentation: application to tempered glass plates*, J. Eur. Ceram. Soc. **27** (2007) 2407.

[72] G. R. Anstis, P. Chantikul, B. R. Lawn and D. B. Marshall, *A critical evaluation of indentation techniques for measuring fracture toughness: direct measurements*, J. Am. Ceram. Soc. **64** (1981) 4 533.

[73] D. Contardo, M. Klute, J. Mans, L. Silvestris and J. Butler *Technical proposal for the phase-II upgrade of the CMS detector* tech. rep. CERN-LHCC-2015-010. LHCC-P-008. CMS-TDR-15-02 CERN, 2015.

[74] A. Benaglia, M. Lucchini, K. Pauwels, C. Tully, T. Medvedeva, A. Heering, C. Dujardin, V. Kononets, K. Lebbou, N. Aubry, S. Faraj, G. Ferro, P. Lecoq and E. Auffray, *Test beam results for a high granularity LuAG fibre calorimeter prototype*, J. Instrum. **11** (2016) P05004.

[75] M. Cascella, S. Franchino and S. Lee, *The Future of High Energy Physics - Some Aspects*, World Scientific Publishing Co. Pte. Ltd. (2017).

[76] M. T. Lucchini, K. Pauwels, K. Blazek, S. Ochesanu and E. Auffray, *Radiation tolerance of LuAG:Ce and YAG:Ce crystals under high levels of gamma- and proton-irradiation*, IEEE Trans. Nuc. Sci. **63** (2016) 586.

[77] F. Cova, F. Moretti, M. Fasoli, N. Chiodini, K. Pauwels, E. Auffray, M. T. Lucchini, S. Baccaro, A. Cemmi, H. Bartova and A. Vedda, *Radiation hardness of Ce-doped sol-gel silica fibers for high energy physics applications*, Opt. Lett. **43** (2018) 4 903.

[78] Y. Sun, M. Koshimizu and S. Kishimoto, *Synthesis and characterization of Pr^{3+}-doped glass scintillators prepared by the sol-gel method*, J. Sol-Gel Sci. Technol. **62** (2012) 313.

[79] H. Ogino, A. Yoshikawa, M. Nikl, A. Krasnikov, K. Kamada and T. Fukuda, *Growth and scintillation properties of Pr-doped $Lu_3Al_5O_{12}$ crystals*, J. Cryst. Growth **287** (2006) 335.

[80] W. Drozdowski, P. Dorenbos, J. de Haas, R. Drozdowska, A. Owens, K. Kamada, K. Tsutsumi, Y. Usuki, T. Yanagida and A. Yoshikawa, *Scintillation properties of praseodymium activated $Lu_3Al_5O_{12}$ single crystals*, IEEE Trans. Nucl. Sci. **55** (2008) 2420.

[81] T. Yanagida, Y. Fujimoto, K. Kamada, D. Totsuka, H. Yagi, T. Yanagitani, Y. Futami, S. Yanagida, S. Kurosawa, Y. Yokota, A. Yoshikawa and M. Nikl, *Scintillation properties of transparent ceramic Pr:LuAg for different Pr concentrations*, IEEE Trans. Nucl. Sci. **59** (2012) 2146.

[82] M. Zhuravleva, A. Novoselov, E. Mihokova, J. A. Mares, A. Vedda, M. Nikl and A. Yoshikawa, *Crystal growth and scintillating properties of (Pr,Si)-doped $YAlO_3$*, Cryst. Res. Technol. **42** (2007) 1324.

[83] M. Nikl, J. A. Mares, A. Vedda, M. Fasoli, V. Laguta, E. Mihokova, J. Pejchal, M. Zhuravleva, A. Yoshikawa and K. Nejezchleb, *Can Pr-doped YAP scintillator perform better?*, IEEE Trans. Nucl. Sci. **57** (2010) 1168.

[84] A. Novoselov, H. Ogino, A. Yoshikawa, M. Nikl, J. Pejchal, J. A. Mares, A. Beitlerova, C. D'Ambrosio and T. Fukuda, *Study on crystal growth and luminescence properties of Pr-doped RE_2SiO_5 (RE = Y, Lu)*, J. Cryst. Growth **287** (2006) 309.

[85] W. Strçk, J. Legendziewicz, E. Lukowiak, K. Maruszewski, J. Sokolnicki, A. A. Boiko and M. Borzechowska, *Optical properties of Pr^{3+} doped silica gel glasses obtained by sol-gel method*, Spectrochim. Acta Part A **54** (1998) 2215.

[86] R. Percival, M. Phillips and D. Hanna, *Characterization of spontaneous ans stimulated emission from praseodymium (Pr^{3+}) ions doped into a silica-based monomode optical fiber*, IEEE J. Quantum Electron **25** (1989) 2119.

[87] S. Derenzo, G. Bizarri, R. Borade, E. Bourret-Courchesne, R. Boutchko, A. Canning, A. Chaudhry, Y. Eagleman, G. Gundiah, S. Hanrahan, M. Janecek and M. Weber, *New scintillators discovered by high-thorughput screening*, Nucl. Instrum. Methods Phys. Res. Sect. A **652** (2011) 247.

[88] C. M. Sunta, *Unraveling Thermoluminescence*, Springer (2015).

[89] M. Nikl, K. Nitsch, S. Baccaro, A. Cecilia, M. Montecchi, B. Borgia, I. Dafinei, M. Diemoz, M. Martini, E. Rosetta, G. Spinolo, A. Vedda, M. Kobayashi, M. Ishii, Y. Usuki, O. Jarolimek and P. Reiche, *Radiation induced formation of color centers in $PbWo_4$ single crystals*, J. Appl. Phys. **82** (1997) 5758.

[90] A. N. Annenkov, E. Auffray, A. E. Borisevich, G. Drobychev, A. Fedorov, A. Inyakin, M. Korzhik, A. Lopatik, P. Lecoq, J. Mendiburu, P. Nedelec, J. Peigneux, P. Rebecchi and D. Sillou, *On the mechanism of radiation damage of optical transmission in lead tungstate crystal*, Phys. Status Solidi A **191** (2002) 277.

[91] L. Zhang, D. Bailleux, A. Bornheim, K. Zhu and R. Zhu, *Performance of the monitoring light source for the CMS lead tungstate crystal calorimeter*, IEEE Trans. Nuc. Sci. **52** (2005) 1123.

[92] J. S. Stroud, *Photoionization of Ce^{3+} in glass*, J. Chem. Phys. **35** (1961) 3 844–850.

[93] A. Vedda and M. Fasoli, *Tunneling recombinations in scintillators, phosphors and dosimeters*, Radiat. Meas. **118** (2018) 86.

[94] A. J. Wojtowicz, J. Glodo, W. Drozdowski and K. R. Przegietka, *Electron traps and scintillation mechanism in $YAlO_3$:Ce and $LuAlO_3$:Ce scintillators*, J. Lumin. **79** (1998) 275.

[95] P. Avouris and T. N. Morgan, *A tunneling model for the decay of luminescence in inorganic phosphors: the case of Zn_2SiO_4:Mn*, J. Chem. Phys. **74** (1981) 8 4347.

[96] D. J. Huntley, *An explanation of the power-law decay of luminescence*, J. Phys. Condens. Matter **18** (2006) 1359.

[97] M. Martini, F. Meinardi, E. Rosetta, G. Spinolo, A. Vedda, J. L. Leray, P. Paillet, J. L. Autran and R. A. B. Devine, *Radiation induced trap levels in SIMOX oxides: low temperature thermally stimulated luminescence*, IEEE Trans. Nuc. Sci. **45** (1998) 1396.

[98] J. T. Randall and M. H. F. Wilkins, *Phosphorescence and electron traps. II. The interpretation of long period phosphorescence*, Proc. Roy. Soc. Lond. **184** (1945) 390.

[99] W. L. Medlin, *Decay of phosphorescence from a distribution of trapping levels*, Phys. Rev. B **123** (1961) 2 592.

[100] H. Wieczorek and O. Overdick "Afterglow and Hysteresis in CsI:Tl" *Proceedings of the 5^{th} International Conference on Inorganic Scintillators and their Applications (SCINT99)* ed. by V. Mikhailin M. V. Lomonosov Moscow State University, Aug. 2000, p. 385.

[101] M. G. Rodriguez, G. Denis, M. S. Akselrod, T. H. Underwood and E. G. Yukihara, *Thermoluminescence, Optically Stimulated Luminescence and Radioluminescence Properties of Al_2O_3:C,Mg*, Radiat. Meas. **46** (2011) 1469.

[102] S. Blahuta, A. Bessiere, D. Gourier, V. Ouspenski and B. Viana, *Effect of X-ray dose on the luminescence properties of Ce:LYSO and co-doped Ca,Ce:LYSO single crystals for scintillation applications*, Opt. Mater. **35** (2013) 1865.

[103] E. Dell'Orto, M. Fasoli, G. Ren and A. Vedda, *Defect-driven radioluminescence sensitization in scintillators: the case of $Lu_2Si_2O_7$:Pr*, J. Phys. Chem. C **117** (2013) 20201.

[104] F. Moretti, G. Patton, A. Belsky, M. Fasoli, A. Vedda, M. Trevisani, M. Bettinelli and C. Dujardin, *Radioluminescence sensitization in scintillators and phosphors: trap engineering and modeling*, J. Phys. Chem. C **118** (2014) 9670.

[105] S. Blahuta, B. Viana, A. Bessiere, E. Mattmann and B. LaCourse, *Luminescence quenching processes in $Gd_2O_2S:Pr^{3+},Ce^{3+}$ scintillating ceramics*, Opt. Mater. **33** (2011) 1514.

[106] S. C. Blankespoor, S. E. Derenzo, W. W. Moses, C. S. Rossington, M. Ito and K. Oba, *Characterization of a pulsed X-ray source for fluorescent lifetime measurements*, IEEE Trans. Nuc. Sci. **41** (1994) 4 698.

[107] A. Dobrowolska, A. J. Bos and P. Dorenbos, *Electron tunneling phenomena in YPO_4:Ce,Ln (Ln = Er, Ho, Nd, Dy)*, J. Phys. D: Appl. Phys. **47** (2014) 335301.

[108] A. Losavio, B. Crivelli, A. Cazzaniga, M. Martini, G. Spinolo and A. Vedda, *Oxide damage by ion implantation in silica*, Appl. Phys. Lett. **74** (1999) 2453.

[109] S. Blahuta, A. Bessiere, B. Viana, P. Dorenbos and V. Ouspenski, *Evidence and consequences of Ce^{4+} in LYSO:Ce, Ca and LYSO:Ce, Mg single crystals for medical imaging applications*, IEEE Trans. Nucl. Sci. **60** (2013) 3134.

[110] M. Nikl, A. Vedda, M. Fasoli, I. Fontana, V. Laguta, E. Mihokova, J. Pejchal, J. Rosa and K. Nejezchleb, *Shallow traps and radiative recombination processes in $Lu_3Al_5O_{12}$;Ce single crystal scintillator*, Phys. Rev. B **76** (2007) 195121.

[111] S. Lee, M. Liva and R. Wigmans, *Dual-readout calorimetry*, Rev. Mod. Phys. **90** (2017) 025002.

[112] N. Akchurin, O. Atramentov, K. Carrell, K. Z. Gümüs, J. Hauptman, H. Kim, H. P. Paar, A. Penzo and R. Wigmans, *Separation of scintillation and Cherenkov light in an optical calorimeter*, Nucl. Instrum. Methods Phys. Res. A **550** (2005) 185.

[113] W. J. Yoo, S. H. Shin, D. Jeon, S. Hong, S. G. Kim, H. I. Sim, K. W. Jang, S. Cho and B. Lee, *Simultaneous measurements of pure scintillation and Cerenkov signals in an integrated fiber-optic dosimeter for electron beam therapy dosimetry*, Opt. Express **21** (2013) 27770.

[114] T. M. Shaffer, C. M. Drain and J. Grimm, *Optical imaging of ionizing radiation from clinical sources*, J. Nuc. Med. **57** (2016) 1661.

[115] A. Arodzero, S. Boucher, J. Hartzell, S. V. Kutsaev, R. C. Lanza, V. Palermo, S. Vinogradov and V. Ziskin ed. by IEEE Nucl. Sci. Symp. and Med. Imaging Conf. (NSS/MIC) 2015, p. 1.

[116] A. Arodzero 2011/0163236 2011.

[117] M. Christl, J. H. Adams, E. N. Kuznetsov and S. Nazzel *PROC. OF THE 31st ICRC (Local Organizing Committee of ICRC, Lodz, Poland, 2009)* 2009.

[118] F. Cova, M. T. Lucchini, K. Pauwels, E. Auffray, N. Chiodini, M. Fasoli and A. Vedda, *Dual Cherenkov and Scintillation Response to High-Energy Electrons of Rare-Earth-Doped Silica Fibers*, Phys. Rev. Appl. **11** (2019) 024036.

[119] S. Myers, *The engineering needed for particle physics*, Phil. Trans. R. Soc. A **370** (2012) 3887.

[120] J. Spanggaard *Delay Wire Chambers - A Users Guide* tech. rep. SL-Note-98-023-BI CERN, Geneva, 1998.

[121] A. N. Vasil'ev *International Conference on Engineering of Scintillation Materials and Radiation Technologies* ed. by Springer 2016, p. 3.

[122] N. Akchurin, C. Cowden, J. Damgov, C. Dragoiu, P. Dudero, J. Faulkner and S. Kunori, *Cerium-doped scintillating fused-silica fibers*, J. Instrum. **13** (2018) P04010.

[123] P. Krizan, *Recent progress in particle identification methods*, Nucl. Instrum. Methods Phys. Res. A **598** (2009) 130.

[124] J. P. Hayward, C. L. Hobbs, Z. W. Bell, L. A. Boatner, R. E. Johnson, J. O. Ramey, G. E. Jellison and C. R. Lillard, *Characterizing the radiation response of Cherenkov glass detectors with isotropic sources*, J. Radioanal. Nucl. Chem. **295** (2013) 1143.

[125] C. W. Fabjan and F. Gianotti, *Calorimetry for particle physics*, Rev. Mod. Phys. **75** (2003) 1.

[126] M. T. Lucchini, E. Auffray, A. Benaglia, F. Cavallari, D. Cockerill, A. Dolgopolov, J. L. Faure, N. Golubev, P. R. Hobson, S. Jain, M. Korjik, V. Mechinski, A. Singovski, T. Tabarelli de Fatis, I. Tarasov and S. Zahid, *Double side readout technique for mitigation of radiation damage effects in $PbWO_4$ crystals*, J. Instrum. **11** (2016) P04021.

[127] C. Hu, S. Liu, M. Fasoli, A. Vedda, M. Nikl, X. Feng and Y. Pan, *ESR and TSL study of hole and electron traps in LuAG:Ce,Mg ceramic scintillator*, Opt. Mater. **45** (2015) 252.

[128] A. Arora, D. B. Marshall and B. R. Lawn, *Indentation deformation/fracture of normal and anomalous glasses*, J. Non-Cryst. Solids **31** (1979) 415.